

**ELECTRONIC STRUCTURES OF Ni FILMS ON Cu(001)  
STUDIED BY ANGLE-RESOLVED PHOTOEMISSION  
SPECTROSCOPY**

**Ratchadaporn Supruangnet**



**A Thesis Submitted in Partial Fulfillment of the Requirements for the  
Degree of Doctor of Philosophy in Physics  
Suranaree University of Technology  
Academic Year 2010**

โครงสร้างอิเล็กทรอนิกส์ของฟิล์มนิกเกิลบนทองแดงระนาบ (001) ศึกษาโดย  
เทคนิคโฟโตมิชชันสเปกโทรสโกปีแบบแยกแยะเชิงมุม

นางสาวรัชฎาภรณ์ ทรัพย์เรืองเนตร



วิทยานิพนธ์นี้เป็นส่วนหนึ่งของการศึกษาตามหลักสูตรปริญญาวิทยาศาสตรดุษฎีบัณฑิต  
สาขาวิชาฟิสิกส์  
มหาวิทยาลัยเทคโนโลยีสุรนารี  
ปีการศึกษา 2553

**ELECTRONIC STRUCTURES OF Ni FILMS ON Cu(001)  
STUDIED BY ANGLE-RESOLVED PHOTOEMISSION  
SPECTROSCOPY**

Suranaree University of Technology has approved this thesis submitted in partial fulfillment of the requirements for the Degree of Doctor of Philosophy.

Thesis Examining Committee

---

(Asst. Prof. Dr. Chinorat Kobdaj)

Chairperson

---

(Assoc. Prof. Dr. Prayoon Songsiriritthigul)

Member (Thesis Advisor)

---

(Dr. Hideki Nakajima)

Member

---

(Assoc. Prof. Dr. Vittaya Amornkitbamrung)

Member

---

(Asst. Prof. Dr. Supagorn Rugmai)

Member

---

(Dr. Saroj Rujirawat)

Member

---

(Dr. Wut Dankittikul)

---

(Assoc. Prof. Dr. Prapun Manyum)

Acting Vice Rector for Academic Affairs    Dean of Institute of Science

รัชฎาภรณ์ ทรัพย์เรืองเนตร : โครงสร้างอิเล็กทรอนิกส์ของฟิล์มนิกเกิลบนทองแดงระนาบ (001) ศึกษาโดยเทคนิคโฟโตอิมิชชันสเปกโทรสโกปีแบบแยกแยะเชิงมุม (ELECTRONIC STRUCTURES OF Ni FILMS ON Cu(001) STUDIED BY ANGLE-RESOLVED PHOTOEMISSION SPECTROSCOPY) อาจารย์ที่ปรึกษา: รองศาสตราจารย์ ดร.ประยูร ส่งศิริฤทธิกุล, 176 หน้า.

ในงานวิทยานิพนธ์นี้ได้ศึกษาถึงที่มาทางอิเล็กทรอนิกส์ในการเกิดการเปลี่ยนแปลงทิศทางของแม่เหล็กในฟิล์มบางนิกเกิลที่ปลูกแบบอพิแทกซ์บนทองแดงระนาบ (001) โดยแมกเนติกแอนไอโซทรอปีนี้จะขึ้นกับความหนาของแผ่นฟิล์ม ซึ่งทิศทางของแม่เหล็กปกติขึ้นอยู่กับความหนาของแผ่นฟิล์มจะเปลี่ยนไปอยู่ในทิศที่ตั้งฉากกับพื้นผิวของแผ่นฟิล์มที่ความหนาประมาณ 7 ชั้นอะตอม และเปลี่ยนจากทิศทางที่ตั้งฉากกับพื้นผิวกลับไปอยู่ในทิศทางที่ขนานกับพื้นผิวของแผ่นฟิล์มที่ความหนาประมาณ 40 ชั้นอะตอม เนื่องจากการศึกษาพฤติกรรมในการเปลี่ยนแปลงทิศทางของแม่เหล็กนี้มีความสำคัญในการพัฒนาอุปกรณ์ที่ใช้ในการจัดเก็บข้อมูลที่มีความจุสูง และสร้างความรู้พื้นฐานเกี่ยวกับวัสดุทางแม่เหล็กที่มีความบางมาก ๆ ที่ผ่านมาได้มีการศึกษาเชิงทฤษฎีถึงความสัมพันธ์ระหว่างโครงสร้างทางอะตอมและโครงสร้างอิเล็กทรอนิกส์ต่อการเกิดแมกเนติกแอนไอโซทรอปีนี้ว่าเกี่ยวข้องกับอันตรกิริยาระหว่างสปินและวงโคจรของอิเล็กตรอน โดยมีการสังเกตว่าที่บริเวณพื้นผิวและรอยต่อระหว่างแผ่นฟิล์มที่ปลูกบนแผ่นฐานที่เป็นวัสดุต่างชนิดกันจะเกิดการบิดเบี้ยวของแลตทิซ และโครงสร้างทางอิเล็กทรอนิกส์จะเปลี่ยนรูปไปจากเดิมที่มีลักษณะคล้ายทรงกลม ในเชิงทฤษฎีออร์บิทัลโมเลกุล วงโคจรที่อิเล็กตรอนสามารถอยู่ได้จะขึ้นกับทิศทางการเปลี่ยนของโครงสร้างทางอะตอม ซึ่งจะมีผลต่อแมกเนติกแอนไอโซทรอปีเนื่องจากสปินของอิเล็กตรอนส่วนมากจะมีทิศที่ตั้งฉากกับพื้นผิวของแผ่นฟิล์ม ถึงแม้จะมีการศึกษาเกี่ยวกับโครงสร้างทางแม่เหล็กที่ขึ้นกับความหนาของแผ่นฟิล์มมาเป็นจำนวนมากแล้ว แต่การอธิบายถึงที่มาในการเกิดแมกเนติกแอนไอโซทรอปีในทางโครงสร้างอิเล็กทรอนิกส์ยังไม่มีกรอบแน่ชัด ดังนั้นในวิทยานิพนธ์นี้จึงได้ศึกษาว่าเมื่อเพิ่มความหนาของแผ่นฟิล์มแล้วโครงสร้างทางอิเล็กทรอนิกส์และสมมาตรของวงโคจรอิเล็กตรอนจะมีผลต่อการเปลี่ยนแปลงแมกเนติกแอนไอโซทรอปีอย่างไร โดยเทคนิคที่ใช้ในการศึกษาคือเทคนิคโฟโตอิมิชชันสเปกโทรสโกปีแบบแยกแยะเชิงมุมร่วมกับการคำนวณโครงสร้างอิเล็กทรอนิกส์แบบเฟสฟังก์ชันเฟลิต โดยการศึกษาจะใช้ข้อดีจากเทคนิคโฟโตอิมิชชันที่สามารถแยกแยะโครงสร้างทางอิเล็กทรอนิกส์ของอิเล็กตรอนจากวงโคจรต่าง ๆ ในโลหะนิกเกิลได้ การแยกแยะนี้สามารถทำได้โดยการเปลี่ยนมุม

ตกกระทบของแสงที่มีโพลาไรซ์แบบเส้นตรง และวิธีนี้ยังสามารถหาความสัมพันธ์ระหว่างค่าความเข้มของสเปกตรัมที่สถานะต่าง ๆ กันได้อีกด้วย เมื่อเริ่มปลูกฟิล์มนิกเกิลบนผิวทองแดงระนาบ (001) พบว่าระดับพลังงาน  $3d$  ของนิกเกิลจะอยู่ใกล้กับระดับพลังงาน  $4s$  ของทองแดง ซึ่งในการศึกษาโครงสร้างอิเล็กทรอนิกส์ของพื้นผิวในทิศทางโมเมนตัม  $\Gamma-\Delta-X$  พบว่าฟิล์มนิกเกิลในช่วงความหนา 0.5 จนถึง 20 ชั้นอะตอมนั้น ระดับพลังงานที่มีวงโคจรอิเล็กทรอนิกส์ตรอนในแบบ  $d_{z^2}$  จะค่อย ๆ เลื่อนตำแหน่งไปในทิศทางที่มีค่าพลังงานยึดเหนี่ยวลดลง แต่ถ้าความหนาของแผ่นฟิล์มมีค่ามากกว่า 6.6 ชั้นอะตอม ระดับพลังงานที่มีวงโคจรอิเล็กทรอนิกส์ตรอนในแบบ  $d_{x^2-y^2}$  จะค่อย ๆ เลื่อนไปในทิศทางที่มีค่าพลังงานยึดเหนี่ยวสูงขึ้น ในช่วงความหนาของแผ่นฟิล์มระหว่าง 6.6 ถึง 20 ชั้นอะตอมนี้ ทั้งการเพิ่มจำนวนของอิเล็กตรอนในวงโคจรอิเล็กทรอนิกส์ตรอนในแบบ  $d_{x^2-y^2}$  และการลดจำนวนของอิเล็กตรอนในวงโคจรแบบ  $d_{z^2}$  มีส่วนทำให้เกิดสถานะของแม่เหล็กในแนวตั้งฉากกับผิวเพิ่มมากขึ้น ซึ่งสอดคล้องกับผลการคำนวณโครงสร้างอิเล็กทรอนิกส์แบบเฟิร์ดพรีนซิเพิลในฟิล์มที่มีความหนาระหว่าง 1 ถึง 7 ชั้นอะตอม



สาขาวิชาฟิสิกส์  
ปีการศึกษา 2553

ลายมือชื่อนักศึกษา \_\_\_\_\_  
ลายมือชื่ออาจารย์ที่ปรึกษา \_\_\_\_\_  
ลายมือชื่ออาจารย์ที่ปรึกษาร่วม \_\_\_\_\_

RATCHADAPORN SUPRUANGNET : ELECTRONIC STRUCTURES OF  
Ni FILMS ON Cu(001) STUDIED BY ANGLE-RESOLVED  
PHOTOEMISSION SPECTROSCOPY. THESIS ADVISOR :  
ASSOC. PROF. PRAYOON SONGSIRIRITTHIGUL, Ph.D. 176 PP.

Ni/THIN FILM/ANGLE-RESOLVED PHOTOEMISSION  
SPECTROSCOPY/SURFACE ENERGY BAND DISPERSION/PERPENDICULAR  
MAGNETIC ANISOTROPY

This thesis reports the electronic origin of magnetic anisotropy transition in thin nickel films epitaxially grown on Cu(001). The magnetic anisotropy strongly depends on the film thickness and rotates from the “usual” in-plane magnetization to out-of-plane at about 7 ML and from out-of-plane to in-plane at about 40 ML. Since this behavior is of technological as well as of scientific relevance this study impacts on the advanced development of magnetic recording devices and fundamental understanding on low-dimensional magnetic materials. The origin of the magnetic anisotropy has been analyzed in the framework of the spin-orbit interaction leading to the correlation between the lattice and electronic structures. As observed in films grown on heterogeneous substrates, the lattice distortion takes place in the surface and interface, and the electronic structures deforms from the usual spherical shape. In terms of molecular orbit theory, the electron orbit occupancy depends on the direction of lattice distortions, and influences on the magnetic anisotropy favoring the spins into the perpendicular to the dominated orbital plane. Even though the macroscopic lattice and magnetic structures upon the film thickness have been investigated well,

the microscopic origin based on electronic structures was not clarified. In this study, angle-resolved photoemission spectroscopy (ARPES) and first-principles energy-band calculation were performed to analyze how the energy band structure and its symmetry contribute to the magnetic anisotropy transition as the film grows. The main idea behind spectroscopic experiment is to take advantage of the photoemission matrix elements in order to disentangle the various  $d$ -orbitals contributing to the photoemission spectra from nickel. The matrix elements are exploited by changing the incident angle of the linearly polarized light and thereby lead to the relative intensities and spectral profiles for the different states. As the Ni film grows, Ni  $3d$  bands are formed near the Fermi level in the range of the Cu  $4s$  bands. In the surface band dispersions measured along the  $\bar{\Gamma}$ - $\bar{\Delta}$ - $\bar{X}$  plane, one band with  $d_{z^2}$  orbital character evolves with a small shift to low binding energy up to 20 ML, while the other band with  $d_{x^2-y^2}$  orbital character gradually forms with a shift to high binding energy above 6.6 ML. Both an increase of the  $d_{x^2-y^2}$  and a decrease of the  $d_{z^2}$  band fillings in the Ni thickness range between 6.6 and 20 ML contribute to reinforce the perpendicular magnetic anisotropy, which are partly backed up by a first-principles energy band calculation.

School of Physics

Academic Year 2010

Student's Signature \_\_\_\_\_

Advisor's Signature \_\_\_\_\_

Co-advisor's Signature \_\_\_\_\_

## ACKNOWLEDGEMENTS

This thesis would not have been completed without assistance and guidance from many people in various ways. Therefore, I would like to deeply thank to the following persons for their contribution:

First and foremost I would like to express my special gratitude to my advisor, Assoc. Prof. Dr. Prayoon Songsiriritthigul, who has supported me throughout my thesis with his patience and knowledge during the course of my graduate studies at the School of Physics. I would like to express my sincere gratitude to my co-advisor, Dr. Hideki Nakajima for his support, guidance and suggestions during the whole period of this work. I would like to thank Dr. Ritthikrai Chai-ngam for his advices and his help with all of the SMOKE measurements. I would like to thank Prof. Dr. Sukit Limpijumnong and his group for support and providing me to use the facilities for calculation in this work. I would like to thank Assoc. Prof. Dr. Vittaya Amornkitbamrung, Asst. Prof. Dr. Chinorat Kobdaj, Asst. Prof. Dr. Supagorn Rugmai, and Dr. Saroj Rujirawat for contributing as the thesis-examining committees. I would like to thank the Synchrotron Light Research Institute (SLRI) for the scholarship under Contract No. GS-50-D05 and provide the facilities for me to carry out this thesis work. I would like to thank Mr. Natthaphol Sumano for his help with some parts of my thesis. I would like to thank all of the technical staff members of SLRI for their support. Finally, I would like to express thanks to my family for their support and encouragement.

Ratchadaporn Supruangnet

# CONTENTS

|   | <b>Page</b> |
|---|-------------|
| ABSTRACT IN THAI.....                               | I           |
| ABSTRACT IN ENGLISH.....                            | III         |
| ACKNOWLEDGEMENTS.....                               | V           |
| CONTENTS.....                                       | VI          |
| LIST OF TABLES.....                                 | X           |
| LIST OF FIGURES.....                                | XI          |
| LIST OF ABBREVIATIONS.....                          | XVII        |
| <b>CHAPTER</b>                                      |             |
| <b>I INTRODUCTION.....</b>                          | <b>1</b>    |
| 1.1 Overview of the study.....                      | 1           |
| 1.2 Purpose of the study.....                       | 12          |
| <b>II THEORETICAL BACKGROUND.....</b>               | <b>13</b>   |
| 2.1 Photoemission spectroscopy.....                 | 13          |
| 2.1.1 Basic principle.....                          | 13          |
| 2.1.2 The three step model.....                     | 15          |
| 2.1.3 Angle-resolved photoemission.....             | 17          |
| 2.1.4 Dipole selection rules.....                   | 20          |
| 2.1.5 Spectral representation.....                  | 23          |
| 2.1.6 Photocurrent measured by ARPES.....           | 25          |
| 2.2 Electronic structure of correlated systems..... | 26          |

## CONTENTS (Continued)

|  | <b>Page</b> |
|--|-------------|
| 2.2.1 Band structure of bulk Cu and Cu(100) surface.....       | 26          |
| 2.2.2 Band structure of bulk Ni and Ni(100) surface.....       | 32          |
| 2.3 Magnetism in thin films.....                               | 37          |
| 2.3.1 Basic concepts in the magnetism.....                     | 37          |
| 2.3.2 Surfaces magnetism.....                                  | 40          |
| 2.3.2.1 Dimensionality effects.....                            | 41          |
| 2.3.2.2 Magnetic moments at surfaces.....                      | 42          |
| <b>III THE CALCULATION METHOD.....</b>                         | <b>45</b>   |
| 3.1 Density functional theory.....                             | 45          |
| 3.1.1 The Hohenberg-Kohn theorems.....                         | 46          |
| 3.1.2 Kohn and Sham equation.....                              | 46          |
| 3.1.3 The local density approximation.....                     | 47          |
| 3.1.4 Generalized gradient approximation.....                  | 48          |
| 3.2 Plane waves.....   | 49          |
| 3.3 Pseudopotentials.....                                      | 50          |
| 3.3.1 The concept of pseudopotentials.....                     | 50          |
| 3.3.2 Norm-conserving pseudopotentials.....                    | 51          |
| 3.3.3 Ultrasoft pseudopotentials.....                          | 53          |
| 3.3.4 Projected augmented waves.....                           | 53          |
| 3.4 The Vienna <i>Ab initio</i> Simulation Package (VASP)..... | 54          |
| 3.5 Surface calculations.....                                  | 55          |

## CONTENTS (Continued)

|   | <b>Page</b> |
|---|-------------|
| 3.5.1 Slab models for surfaces.....   | 55          |
| 3.5.2 Computational details.....  | 56          |
| 3.5.3 Ni/Cu(001) surfaces.....  | 57          |
| <b>IV EXPERIMENTAL TECHNIQUES AND INSTRUMENTS.....</b>  | <b>58</b>   |
| 4.1 Experimental techniques.....  | 58          |
| 4.1.1 Auger electron spectroscopy (AES).....  | 58          |
| 4.1.2 Low energy electron diffraction (LEED).....   | 61          |
| 4.1.3 Reflection high energy electron diffraction (RHEED).....                                      | 62          |
| 4.1.4 Molecular beam epitaxy (MBE).....   | 64          |
| 4.1.5 Surface magneto-optical Kerr effect (SMOKE).....  | 65          |
| 4.2 Experimental instruments.....   | 69          |
| 4.2.1 Vacuum chamber.....   | 69          |
| 4.2.2 Electron energy analyzer.....   | 72          |
| 4.3 Sample preparations.....  | 73          |
| 4.4 Thickness calibration.....  | 76          |
| 4.5 Angle-resolved photoemission measurements.....  | 78          |
| 4.6 Surface magneto-optical Kerr effect measurements.....   | 79          |
| <b>V RESULTS AND DISCUSSION.....</b>  | <b>81</b>   |
| 5.1 Normal emission data.....   | 81          |
| 5.2 Surface energy band dispersion along $\bar{\Gamma}$ - $\bar{\Delta}$ - $\bar{X}$ direction..... | 84          |
| 5.3 Magnetic properties of Ni on Cu(001).....   | 109         |



## LIST OF TABLES

| Table   | Page |
|---|------|
| 2.1 Dipole selection rule using linear polarized light coming to single crystal surface.....  | 22   |
| 2.2 Comparison of experiment and calculated binding energies and effective masses of surfaces states on Cu(100).....  | 31   |
| 2.3 The energy levels in the units of electron volts at symmetry points of Ni.....  | 34   |
| 2.4 Magnetic moments (in $\mu_B$ ) of 3d transition metal atoms at the surface and in the center layer, and the corresponding enhancement for the surface atoms.... | 44   |
| A.1 Spherical harmonics and their expressions in Cartesian coordinates.....   | 131  |
| A.2 Linear combinations of the spherical harmonics for <i>s</i> , <i>p</i> , and <i>d</i> orbitals in cubic potential.....  | 132  |
| B.1 Spin-orbit coupling constants for various orbitals of Ni and Cu atoms.....  | 137  |
| C.1 Character table for C <sub>4v</sub> point group.....  | 139  |

## LIST OF FIGURES

| Figure  | Page |
|---|------|
| 1.1 A schematic illustration of longitudinal and perpendicular recordings.....  | 2    |
| 1.2 Magnetization curves of bulk Ni along the easy [111] and hard [100] axes.....   | 3    |
| 1.3 The experimental (a) and theoretical (b) results of magnetic anisotropy energies as a function of the inverse of the film thickness for Ni/Cu(001)..... | 7    |
| 1.4 A schematic drawing of contributions of anisotropy energy on a pseudomorphic grown thin film.....   | 8    |
| 1.5 The experimental data for Ni/Cu(001) shown $K$ as a function of $1/d$ for two reduced temperatures $t$ .....  | 8    |
| 1.6 Magnetic anisotropy energy calculated for 12 ML Ni/Cu(001).....   | 9    |
| 1.7 Calculated $K_v$ and orbital moments for fct Ni as a function of uniaxial deformation of $c/a$ -ratio.....  | 11   |
| 2.1 A schematic relation between the electron energy distribution of photoemitted electrons and the density of state of a metallic solid.....               | 14   |
| 2.2 A schematic diagram of the three-step and the one-step models used to describe ARPES processes.....   | 16   |
| 2.3 A schematic drawing of the geometry of an angular resolved photoemission experiment.....  | 19   |
| 2.4 The attenuation length plotted as a function of the electron kinetic energy.....  | 20   |
| 2.5 Bulk Brillouin zone for the fcc lattice indicated with several high-symmetry lines.....   | 22   |

## LIST OF FIGURES (Continued)

| <b>Figure</b>   | <b>Page</b> |
|---|-------------|
| 2.6 Definition of directions used in a photoemission experiment with $s$ and $p$ polarized light.....   | 23          |
| 2.7 Band structure of Cu along some symmetry points as calculated by Segall (1962) and Burdick (1963).....  | 28          |
| 2.8 Projected bulk band structure for Cu(100) onto the surface BZ along the $\bar{\Gamma}-\bar{X}$ and $\bar{\Gamma}-\bar{M}$ directions.....                     | 29          |
| 2.9 Experimental (left) and theoretical (right) inverse photoemission spectra ( $\hbar\omega = 9.7$ eV) for Cu(100) along the $\Gamma XUL$ bulk mirror plane..... | 30          |
| 2.10 The empirical bulk band structure of Ni along certain symmetry lines in the Brillouin zone.....  | 33          |
| 2.11 Calculated spin-resolved surface electronic states in a five-plane Ni(100) film....  | 36          |
| 2.12 Stoner parameters for the element metals calculated from DOS and spin-dependent mean-field interactions based on density functional theory.....              | 40          |
| 2.13 Calibrated in-phase susceptibility versus temperature for several thickness of Ni/Cu(001).....   | 43          |
| 3.1 A schematic illustration concept of the pseudopotential (dash lines) and all-electron potential (solid lines) and their corresponding wave functions.....     | 52          |
| 3.2 A schematic of basic idea of slab model.....  | 56          |
| 3.3 A schematic diagram of a supercell that used to model: (a) 5 ML Cu(001) and (b) 2 ML Ni on each side of 5 ML Cu(001) slab.....                                | 57          |
| 4.1 A schematic diagram of the Auger process.....   | 60          |

## LIST OF FIGURES (Continued)

| <b>Figure</b>   | <b>Page</b> |
|---|-------------|
| 4.2 The mean free path of the electron in solid.....  | 61          |
| 4.3 A schematic diagram of LEED optics.....   | 62          |
| 4.4 Schematic pictures showing the relationship between the intensity oscillations<br>of the RHEED pattern and the film morphology for layer-by-layer growth..... | 63          |
| 4.5 A schematic picture of diffraction geometry of RHEED.....   | 63          |
| 4.6 RHEED patterns after 5 ML Ni was grown on Cu(001) at room temperature.....  | 64          |
| 4.7 A schematic of the MBE system at the BL4 beamline.....  | 65          |
| 4.8 A schematic diagram of magneto-optic Kerr effect.....   | 68          |
| 4.9 Orientation of the magnetization and the incidence plane for the two main<br>Kerr geometries.....   | 68          |
| 4.10 A schematic diagram of the experimental station for the BL4 at SLRI.....   | 70          |
| 4.11 A schematic diagram of the photoemission system at BL4.....  | 71          |
| 4.12 A schematic diagram of Alpha 110.....  | 72          |
| 4.13 LEED patterns of (a) 1.7 ML, (b) 3.6 ML, (c) 5.5 ML, (d) 7 ML,<br>and (e) 10 ML Ni/Cu(001) at an electron energy of 76 eV.....                               | 74          |
| 4.14 Thickness dependence of the oscillations in RHEED patterns in MBE growth<br>of Ni on Cu(001) at room temperature.....  | 75          |
| 4.15 AES spectra on various Ni films thicknesses including comparing to clean<br>Cu(001) surface.....   | 76          |
| 4.16 Calibration of Ni films thickness obtained from the RHEED oscillation and<br>AES measurements.....   | 77          |

## LIST OF FIGURES (Continued)

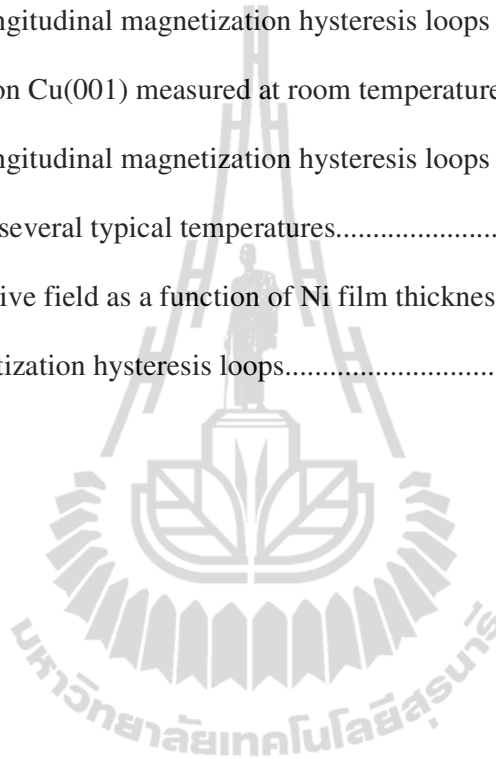
| Figure   | Page |
|--|------|
| 4.17 A schematic illustration of LEED pattern on Ni/Cu(001) surfaces.....  | 79   |
| 4.18 A schematic diagram of the SMOKE experimental setup at the BL4 at SPL in<br>SLRI.....   | 80   |
| 5.1 Photon energy and symmetry dependence obtained from normal-emission<br>ARPES spectra on film thicknesses of 0.6, 3.6, and 6.3 ML.....    | 83   |
| 5.2 A simple drawing of the $d_{x^2-y^2}$ orbital along the $\bar{\Delta}$ mirror plane in the surface<br>BZ coordinate.....                 | 86   |
| 5.3 Thickness dependence of ARPES spectra on the Ni/Cu(001) were measured<br>at normal emission for various thicknesses.....                 | 88   |
| 5.4 Thickness dependence of ARPES spectra on the Ni/Cu(001) were measured<br>at an emission angle of $2^\circ$ for various thicknesses.....  | 89   |
| 5.5 Thickness dependence of ARPES spectra on the Ni/Cu(001) were measured<br>at an emission angle of $4^\circ$ for various thicknesses.....  | 93   |
| 5.6 Thickness dependence of ARPES spectra on the Ni/Cu(001) were measured<br>at an emission angle of $6^\circ$ for various thicknesses.....  | 94   |
| 5.7 Thickness dependence of ARPES spectra on the Ni/Cu(001) were measured<br>at an emission angle of $8^\circ$ for various thicknesses.....  | 95   |
| 5.8 Thickness dependence of ARPES spectra on the Ni/Cu(001) were measured<br>at an emission angle of $10^\circ$ for various thicknesses..... | 96   |

## LIST OF FIGURES (Continued)

| <b>Figure</b>   | <b>Page</b> |
|---|-------------|
| 5.9 Thickness dependence of ARPES spectra on the Ni/Cu(001) were measured at an emission angle of 12° for various thicknesses.....  | 97          |
| 5.10 Thickness dependence of ARPES spectra on the Ni/Cu(001) were measured at an emission angle of 14° for various thicknesses.....   | 98          |
| 5.11 Thickness dependence of ARPES spectra on the Ni/Cu(001) were measured at an emission angle of 17° for various thicknesses.....   | 99          |
| 5.12 Thickness dependence of energy band structures obtained from ARPES spectra on the Ni/Cu(001).....  | 100         |
| 5.13 First-principles energy band calculations in paramagnetic Ni films in the Ni/5 ML-Cu(001)/Ni structure.....  | 102         |
| 5.14 A schematic model of a repetition supercell for 5-ML Ni/5 ML-Cu(001)/5-MLNi structure.....   | 103         |
| 5.15 STM images of (a) 0.2 ML, (b) 0.7 ML, (c) 3.4 ML, (d) 4.5 ML, (e) 5.6 ML, (f) 7.1 ML, (g) 16.9 ML, and (h) 20.3 ML Ni/Cu(100) films.....   | 105         |
| 5.16 LEED patterns of (a) 0.5 ML, (b) 1.0 ML, (c) 3.6 ML, (d) 4.7 ML, (e) 5.2 ML (f) 6.7 ML, (g) 17.5 ML, and (h) 20 ML Ni/Cu(001) films taken at an electron energy of 130eV.....                      | 106         |
| 5.17 Surface roughness (the average height of the islands) plotted versus total coverage for the Ni/Cu(100) system, which was simulated at room temperature with the deposition flux of 0.8 ML/min..... | 108         |

**LIST OF FIGURES (Continued)**

| <b>Figure</b>   | <b>Page</b> |
|---|-------------|
| 5.18 Polar and longitudinal magnetization hysteresis loops for different Ni film thicknesses on Cu(001) measured at room temperature..... | 110         |
| 5.19 Polar and longitudinal magnetization hysteresis loops of Ni films on Cu(001) measured at several typical temperatures.....           | 111         |
| 5.20 Plot of coercive field as a function of Ni film thickness determined from the polar magnetization hysteresis loops.....              | 112         |



## LIST OF ABBREVIATIONS

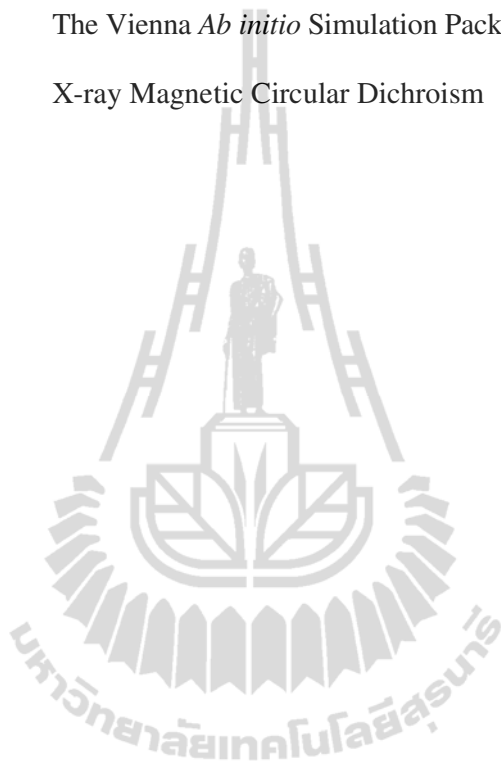
|           |   |   |
|-----------|---|---|
| AES       | = | Auger Electron Spectroscopy                       |
| AL        | = | Attenuation Length                                |
| APW       | = | Augmented Plane Wave                              |
| ARPES     | = | Angle Resolved Photoemission Spectroscopy         |
| BZ        | = | Brillouin Zone                                    |
| CAE       | = | Constant Analyzer Energy                          |
| CG        | = | Conjugate Gradient                                |
| CRR       | = | Constant Retard Ratio                             |
| $d_c$     | = | Critical Thickness                                |
| DFT       | = | Density Functional Theory                         |
| DOS       | = | Density of States                                 |
| $E_{kin}$ | = | Kinetic Energy                                    |
| FCC       | = | Face-Centered-Cubic                               |
| FCT       | = | Face-Centered-Tetragonal                          |
| FWHM      | = | Full Width at Half-Maximum                        |
| GGA       | = | Generalized Gradient Approximation                |
| IMFP      | = | Inelastic Mean Free Path                          |
| IPE       | = | Inverse Photoemission                             |
| $K_{eff}$ | = | Effective Magnetic Anisotropy Energy              |
| $K_I$     | = | Interface Contribution Magnetic Anisotropy Energy |
| $K_S$     | = | Surface Contribution Magnetic Anisotropy Energy   |

**LIST OF ABBREVIATIONS (Continued)**

|        |   |  |
|--------|---|--|
| $K_v$  | = | Volume Contribution Magnetic Anisotropy Energy |
| LCAO   | = | Linear Combination of Atomic Orbitals          |
| LDA    | = | Local Density Approximation                    |
| LEED   | = | Low-Energy Electron Diffraction                |
| MAE    | = | Magnetic Anisotropy Energy                     |
| MBE    | = | Molecular Beam Epitaxy                         |
| MCA    | = | Magnetic Crystalline Anisotropy                |
| ML     | = | Monolayers                                     |
| MRAM   | = | Magnetic Random Access Memory                  |
| PAW    | = | Projector Augmented Wave                       |
| PES    | = | Photoemission Spectroscopy                     |
| PMA    | = | Perpendicular Magnetic Anisotropy              |
| RHEED  | = | Reflection High-Energy Electron Diffraction    |
| SLRI   | = | Synchrotron Light Research Institute           |
| SMOKE  | = | Surface Magneto-Optical Kerr Effect            |
| SPL    | = | Siam Photon Laboratory                         |
| SPLEED | = | Spin Polarized Low-Energy Electron Diffraction |
| SQUID  | = | Superconducting Quantum Interference Device    |
| SRT    | = | Spin Reorientation Transition                  |
| $T_c$  | = | Curie Temperature                              |
| UHV    | = | Ultra-High Vacuum                              |
| USPP   | = | Ultrasoft Pseudopotential                      |

**LIST OF ABBREVIATIONS (Continued)**

|       |   |  |
|-------|---|--|
| $V_0$ | = | Inner Potential of the Crystal                 |
| VASP  | = | The Vienna <i>Ab initio</i> Simulation Package |
| XMCD  | = | X-ray Magnetic Circular Dichroism              |



# CHAPTER I

## INTRODUCTION

### 1.1 Overview of the study

Nowadays, because the low-dimensional magnetic materials are of technological as well as scientific relevance their enormous potential applications in nanotechnology are promising. A wide spectrum of applications covers magnetic random access memory (MRAM), high-density storage media, hard disc read heads, logic devices or miniaturized field sensors (Zhu, Zheng, and Prinz, 2000). Moreover, ultrathin magnetic films also provide our fundamental understanding of magnetic phenomena and their properties suitable for practical applications. The magnetic anisotropy is one of the most important properties of magnetic materials related to all of applications mentioned above.

Magnetic anisotropy energy (MAE) is defined as an energy required to rotating the magnetization from one direction to another with a certain external field. In general, the magnetic anisotropy in films considerably differs from that in bulk due to the reduced symmetry at surfaces, interfaces, and the distorted structures of the pseudomorphic ultrathin films. In particular, it is possible to tailor the magnetic anisotropy by varying the thicknesses of the films such as Co/Pt (Carcia, 1988), Co/Pd (Engel et al., 1991), and Ni/Cu (Huang et al., 1994; Hjortstam and Trygg, 1996; Henk, Niklasson, and Johansson, 1999). The most phenomena in these aspects are usually referred to as perpendicular magnetic anisotropy (PMA) which a key factor in a high density recording (Figure 1.1).

Basically, the MAE is evaluated by measuring the magnetizations along a hard and an easy axis, as shown in Figure 1.2. Typically, the magnitude of the MAE is of the order of only  $10^{-6}$  to  $10^{-3}$  eV/atom. There are two main reasons that describe an increase of MAE in ultrathin films and multilayers by orders of magnitude higher than that of bulk atoms. One is the broken symmetry at the surfaces or interfaces, and the other is the lattice distortion due to strains between the magnetic layers and the substrate layers. The MAE arises from the dipole-dipole and spin-orbit interactions.

The dipole-dipole interaction leads to a contribution to the anisotropy which depending on the sample shape, so-called the shape anisotropy. The spin-orbit coupling effects to the magnetization is so-called the magnetocrystalline anisotropy (MCA). The spin-orbit coupling influences on the magneto-elastic anisotropy, if the sample is stressed. In the following, three anisotropies will be discussed in more detail.

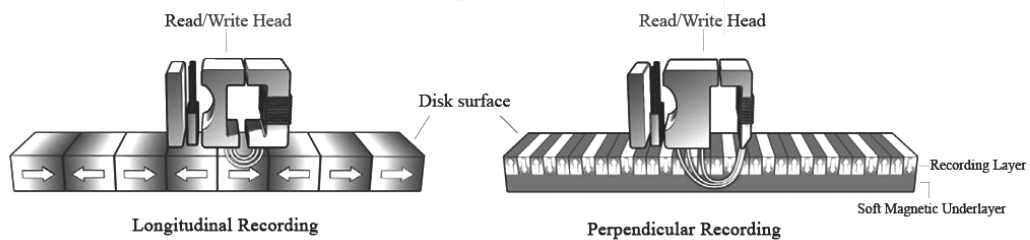


**Figure 1.1** A schematic illustration of longitudinal and perpendicular recordings. Western Digital Technologies (www, 2006).

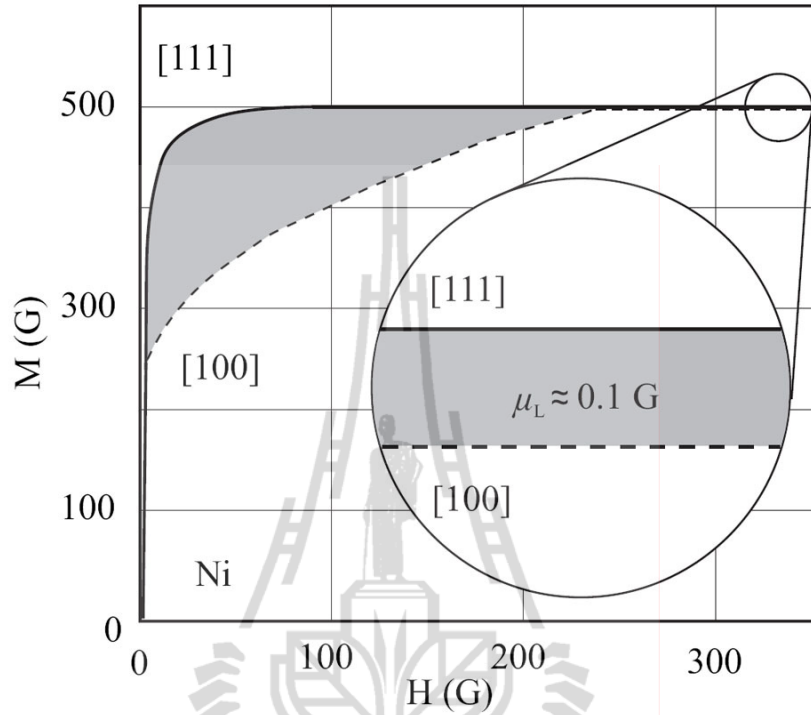


**Figure 1.2** Magnetization curves of bulk Ni along the easy [111] and hard [100] axes (Kittel, 1976). The MAE is directly related to the area enclosed between the two curves.

**Shape anisotropy** The shape anisotropy originates from long-range dipolar interactions and it strongly depends on the specimen shape. For a thin film, the shape effect to the dipole interactions can be described by the demagnetizing field ( $H_d$ ), which is created by the magnetic field, is given by

$$H_d = H_{\text{dip}} - \frac{M}{3} = -DM, \quad (1.1)$$

where  $D$  is the shape-dependent demagnetizing tensor and only the tensor element in the perpendicular direction is available in the thin film. Therefore, the shape anisotropy energy per unit volume is given by (Johnson et al., 1996)

$$E_d = \frac{1}{2} \mu_0 M_s^2 \cos^2 \theta, \quad (1.2)$$

where  $M_s$  is the saturation magnetization and  $\theta$  is the angle of magnetization with respect to the film normal. According to this expression, the in-plane orientation for magnetization favors in the shape anisotropy, because the shape anisotropy does not depend on the film thickness into the expression of Eq. (1.2). Therefore, the shape anisotropy contributes only to bulk MAE ( $K_V$ ) and is proportional to the number of atoms.

**Magnetocrystalline anisotropy: MCA** The phenomenological description of the magnetic anisotropy has been proposed by Néel (1954). In his model, the spin-orbit interaction introduces an angular-dependent magnetic interaction. The Néel's model is based on the localized moment approximation and therefore is not suitable for itinerant magnets. The spin-orbit Hamiltonian can be expressed as (Bruno, 1989)

$$H_{so} = \xi \mathbf{L} \cdot \mathbf{S}, \quad (1.3)$$

where  $\xi$  is the spin-orbit constant (Appendix B). The modification of the band structure induced by the spin-orbit coupling is used to explain the MCA. The spin-orbit interactions lift the degeneracy of the band structures. The crystalline anisotropy energy can be expanded in a power series of the direction cosines of the orientation of the magnetization with respect to the crystal axes  $\alpha_x$ ,  $\alpha_y$  and  $\alpha_z$ . In the case of bulk cubic crystal, the MCA does not give from the second order term ( $\alpha_x^2 + \alpha_y^2 + \alpha_z^2$ ) because it is constant.

For surface, the translational symmetry in the direction of the film normal is broken, resulting in an uniaxial anisotropy (Qiu and Bader, 1999). In general, surface anisotropy can be written as

$$E_{\text{MCA}} = K_s \cos^2 \theta + K_{s,p} \sin^2 \theta \cos^2 \phi, \quad (1.4)$$

where  $\theta$  is the angle of the magnetization away from the surface normal and  $\phi$  is the azimuthal angle (Gradmann, Korecki, and Waller, 1986; Rado, 1982). According to the expression, the surface normal is an easy axis when  $K_s < 0$ , thus the film plane is an easy plane of the surface anisotropy.

Recently, the effect of the symmetry reduction at a surface on MCA can be obtained from *ab-initio* band structure calculations (Pick and Dreysse, 1992; Daalderop, Kelly, and Schuurmans, 1994). The calculations demonstrated the split of state when the direction of the magnetization is perpendicular or parallel to the film plane. Therefore, MCA energy can be obtained by the total energy difference along the direction of magnetization perpendicular and parallel to the surface film. For example, the theoretical and experimental results revealed thickness dependent magnetic anisotropy energies in Ni/Cu(001) as shown in Figure 1.3 (Hong et al., 2004).

**Magneto-elastic anisotropy** The magneto-elastic anisotropy is produced from a strain-induced modification of MCA. In ultrathin films, strain is mainly induced by the lattice mismatch between the film and substrate, which is  $\eta = (a_f - a_s) / a_s$  when  $a_f$  and  $a_s$  are the lattice constants of the film and the substrate, respectively. Therefore, the strain state is film-thickness dependent.

The modification of MCA induced with the strain can be analyzed by the first order term in the Taylor's expansion as

$$E_{\text{ME}} = B_1 (\alpha_1^2 e_{xx} + \alpha_2^2 e_{yy} + \alpha_3^2 e_{zz}) + B_2 (\alpha_1 \alpha_2 e_{xy} + \alpha_2 \alpha_3 e_{xz} + \alpha_1 \alpha_3 e_{zx}). \quad (1.5)$$

Here  $e_{ij}$  denotes the strains,  $B_1$  and  $B_2$  are the magneto-elastic coupling constants. Thus, the magneto-elastic anisotropy energy is easy to calculate when the strains are known.

Since atoms at the surface and interface have a different atomic environment from the bulk atoms, additional magneto-elastic coupling coefficients should be written as  $B_{\text{eff}} = B_{\text{bulk}} + B_s / d$  (Song, Ballentine, and O'Handley, 1994; Sander, 1999). From this discussion, the (effective) magnetic anisotropy energy in 2D systems can be decomposed into a volume contribution ( $K_V$ ) and a contribution from the surface ( $K_S$ ) and interface ( $K_I$ ). The relation between these contributions can be written as

$$K = K_{\text{eff}} = K_V + (K_S + K_I) / d. \quad (1.6)$$

This relation describes the average value of the magnetic anisotropy energy of the surface and interface atoms and inner atoms of a magnetic layer of film thickness  $d$ . A schematic diagram of all contributions of effective magnetic anisotropy energy is shown in Figure 1.4. Commonly, the expression in Eq. (1.1) is usually used in experimental studies,  $K_V$  and  $K_S$  or  $K_I$  are determined by a plot of the product  $K_{\text{eff}}$  versus  $d$ . This is shown in Figure 1.5 for Ni/Cu(001). For thicker Ni/Cu(001) films,  $K_V \approx 30 \mu\text{eV}/\text{atom}$  at a reduced temperature of  $t = T/T_c = 0.56$  is larger than that for bulk Ni (Figure 1.2). Moreover, this argumentation has been proven in the theoretical calculation for a thin film of 12 ML of Ni (Uiberacker et al., 1999). They found that a large negative contribution from surface layer (Figure 1.6) was related to the negative slope in Figure 1.5. It is clear that a positive  $K_{\text{eff}}$  describes the easy axis to be perpendicular to the layer plane.

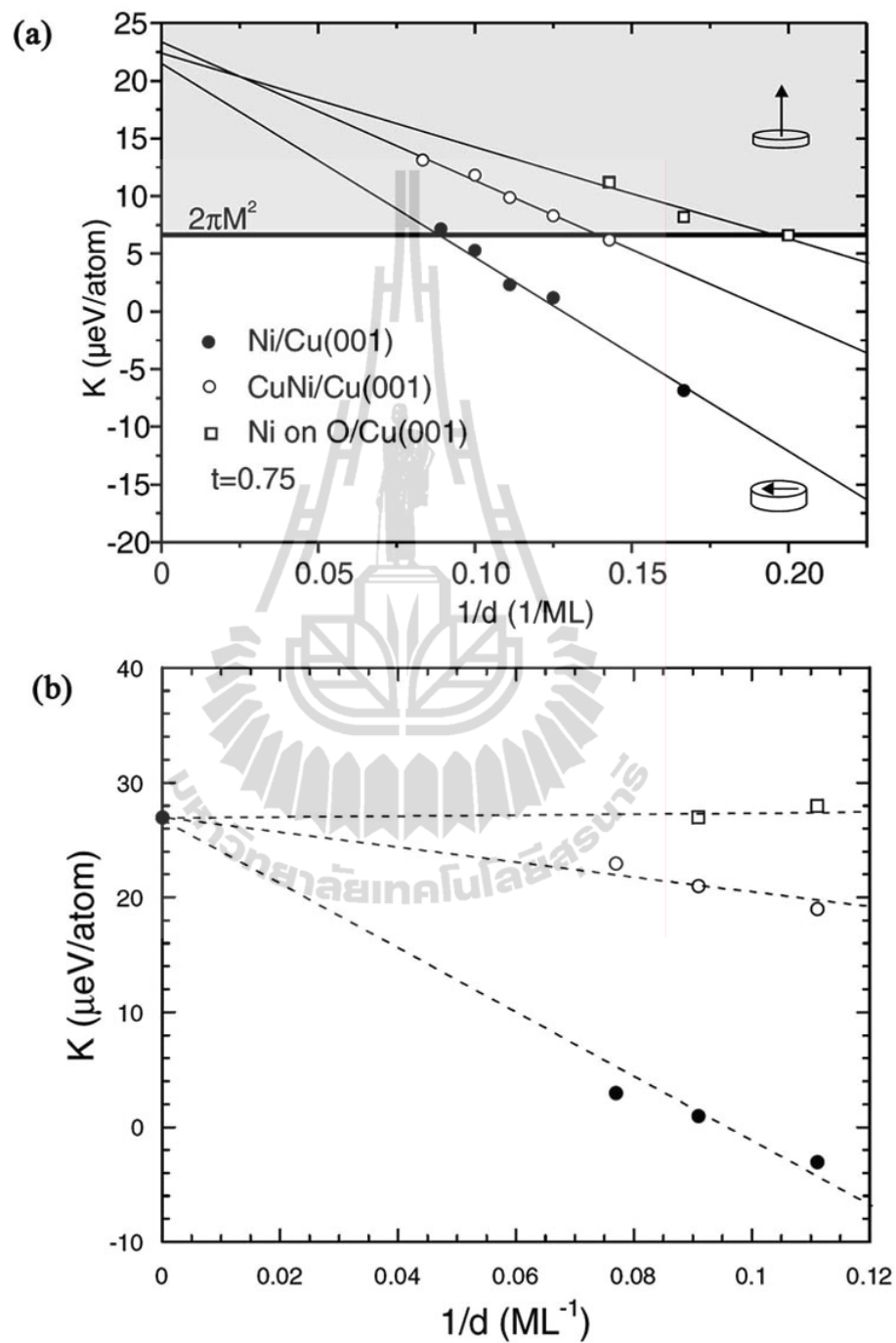


**Figure 1.3** The experimental (a) and theoretical (b) results of magnetic anisotropy energies as a function of the inverse of the film thickness for Ni/Cu(001), Cu/Ni/Cu(001), and Ni/O/Cu(001) (Hong et al., 2004).

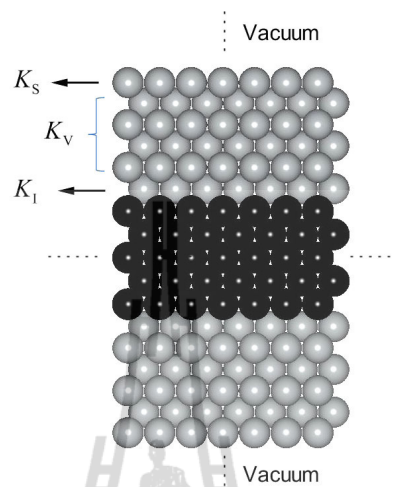


**Figure 1.4** A schematic drawing of contributions of anisotropy energy on a pseudomorphic grown thin film.  $K_S$ ,  $K_I$ , and  $K_V$  are the surface, the interface, and the central of volume contribution, respectively.

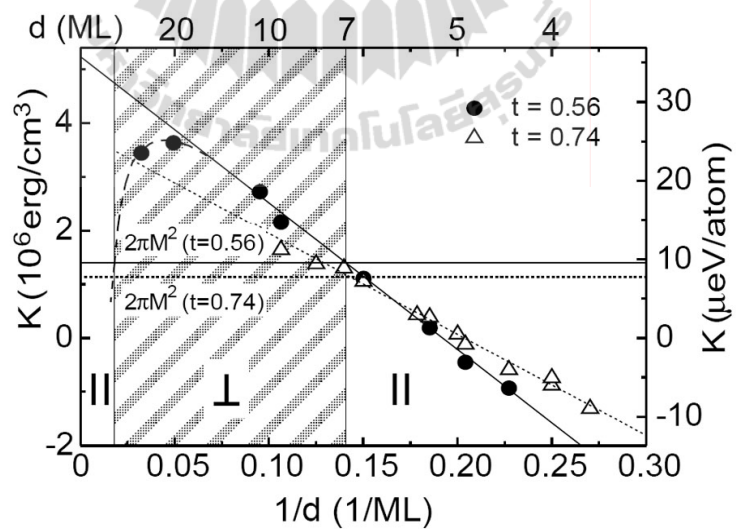


**Figure 1.5** The experimental data for Ni/Cu(001) shown  $K$  as a function of  $1/d$  for two reduced temperatures  $t$ . The marked area is represented the perpendicular magnetization where the  $K_S$  exceeds the shape anisotropy (Baberschke, 1996).

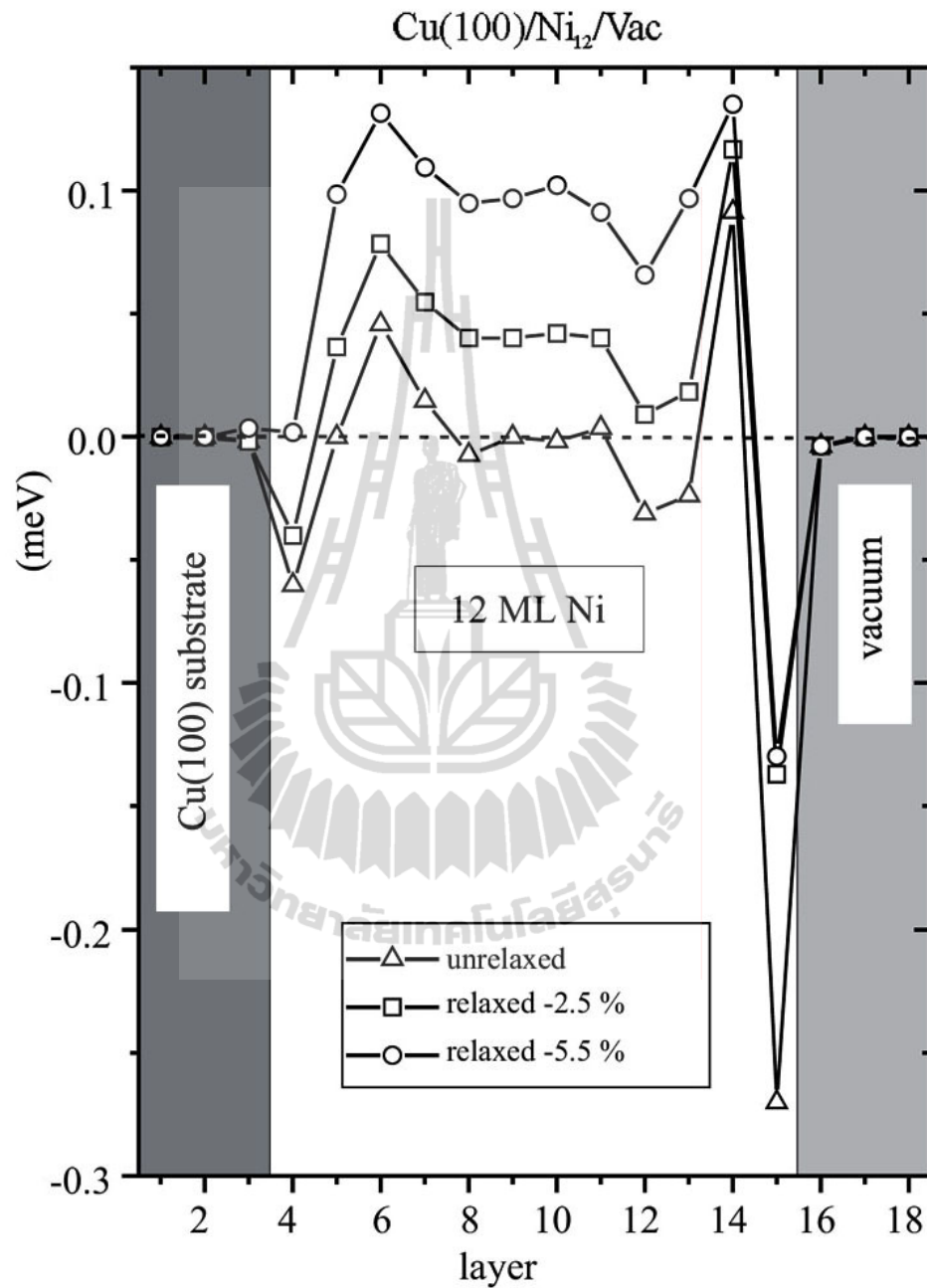


**Figure 1.6** Magnetic anisotropy energy calculated for 12 ML Ni/Cu(001), where the open triangles represent an unrelaxed cubic fcc-lattice structure, squares and circles denote to a relaxed tetragonal structure (Uiberacker et al., 1999).

The prominent case of Ni/Cu(001) has attracted special interest due to its character indicating both normal spin reorientation transition (SRT) and reverse SRT. Thus, they are considered as a basic starting point for magnetism studies in nanoscale. The first reorientation turns in-plane to the perpendicular direction of magnetization axis between 7 ML (Schulz and Baberschke, 1994; Farle et al., 1997a, 1997b) and 10-11 ML (Vollmer et al., 1999; van Dijken et al., 2000). It was found that PMA appears stable in a wide thickness range. The magnetization switches back to in-plane for films thickness up to 35-70 ML (Schulz, Schwarzwald, and Baberschke, 1994; O'Brien, Droubay, and Tonner, 1996). This unusual behavior has been extensively studied both experimentally and theoretically, and these critical thicknesses for Ni/Cu(001) films were found to be analyzed as the distortion of the Ni films owing to the lattice mismatch between Ni and Cu of 2.5%, where the strain relaxation at interface between Ni and Cu is caused by misfit dislocations (Baberschke, 1999). According to the previously reported experiments (Shen, Giergiel, and Kirschner, 1995; Müller et al., 1996; Farle et al., 1997a, 1997b; Platow et al., 1999), the ultrathin Ni films are formed pseudomorphically on Cu(001) up to the thickness around 15 ML and the strains are expanded in-plane and compressed along the surface normal as it's called a face-centered-tetragonal (fct) crystal structure. MAE of fct Ni as a function of the axial  $c/a$  ratio has been calculated by Hjortstam et al. (1997). The theoretical results show the large and positive volume contributions in  $K_V$  term of thin fct Ni films (Figure 1.7).

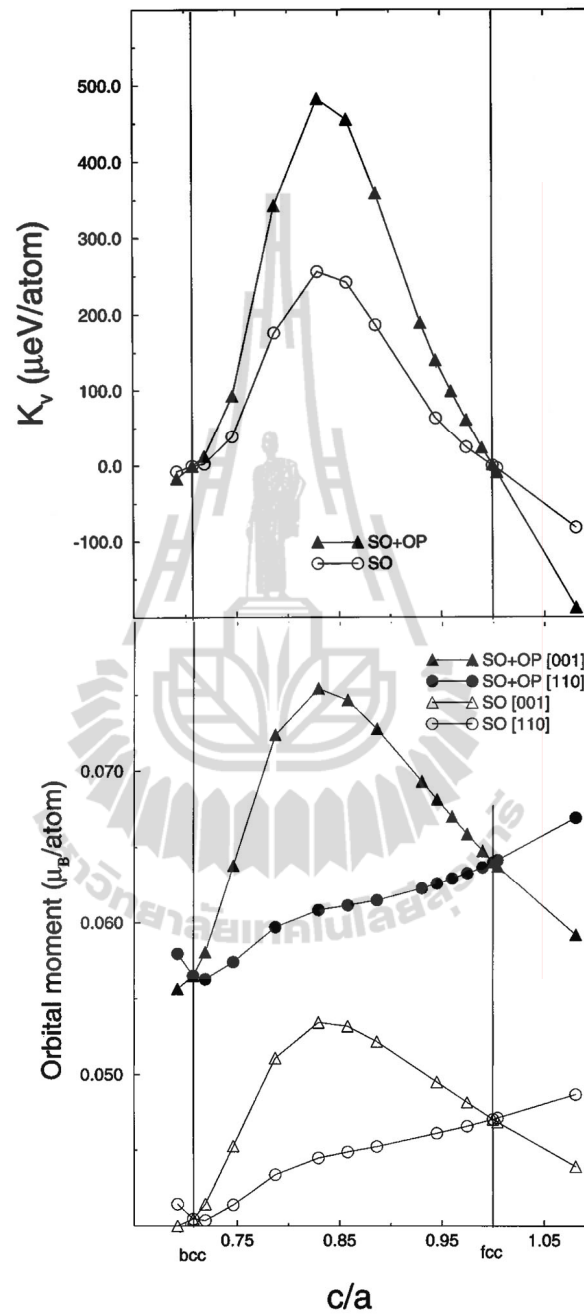


**Figure 1.7** Calculated  $K_V$  and orbital moments for fct Ni as a function of uniaxial deformation of  $c/a$ -ratio. Open symbols denote to spin-orbit-coupling-only, and full symbols to spin orbit in combination with orbital polarization (Hjortstam et al., 1997).

## 1.2 Purpose of the study

The objectives of this thesis are to investigate the electronic structure and the magnetic anisotropy in Ni films on Cu(001) substrate as a function of Ni films thickness. The main technique used in this thesis is the angle-resolved photoemission spectroscopy (ARPES) using the synchrotron radiation. ARPES measurements are able to reveal the thickness- and polarization-dependent energy band dispersions in surface and bulk Brillouin zones (BZs). The surface and interface electronic structures are identified by means of a surface sensitivity measurement as well as constant bulk energy band dispersions in ARPES. In order to understand the basic properties of magnetic anisotropy of this system, the experiment data have to be compared with theoretically calculated models. From a lattice structure viewpoint, low-energy-electron diffraction (LEED) and reflection-high-energy-electron diffraction (RHEED) patterns provide an indication to model dependent upon lattice structure by solving the phase-factor problem in a numerical calculation. However, the local atomic structures including a dislocation and a strain cannot be identified in this study. In terms of magnetism, the SMOKE measurement tells us the easy magnetization axis of Ni films in comparison between the longitudinal and polar hysteresis loops. However, the absolute MAE cannot be evaluated in SMOKE system. So that some reports of magnetic properties including the spin and orbital magnetic moments in Ni films on Cu(001) by means of superconducting quantum interference device (SQUID) (Ney et al., 2002) and x-ray magnetic circular dichroism (XMCD) (Wilhelm et al., 2000; Amemiya et al., 2005) are used to give us an insight on the magnetic properties corresponding to this experimental studies.

## CHAPTER II

### THEORETICAL BACKGROUND

This chapter describes background knowledge such as the basic principle of photoemission spectroscopy including ARPES. Moreover, the interrelation between magnetism and electronic structure are also reviewed.

#### 2.1 Photoemission spectroscopy

##### 2.1.1 Basic principle

Photoemission spectroscopy (PES) is a technique based on the photoelectric effect, first discovered in 1887 by Hertz (1887). Later, in 1905, Albert Einstein was given as the explanation of light-induced electron emission. He introduced the two important concepts in this theory. First, light is made of quantization (photon) where each photon gives the energy by the product of Planck's constant and the frequency of the light ( $h\nu$ ). Second, an electron can absorb a photon and emit with the full final energy where such electron emission is carried with useful information about the electronic structure of solids. Since a short mean free path of the emitted electrons (typically about  $10 \text{ \AA}$ ) from surface in PES measurement, PES provides a surface sensitivity technique. Therefore, photoemission is a direct method to determine the information of the electronic structure of materials. On the basis of the band theory, the solid sample has the Fermi energy ( $E_F$ ) at the top of the occupied states in metals as shown in Figure 2.1, which separates from the vacuum level ( $E_{\text{vac}}$ ) by  $\Phi$ .

The electrons are emitted from matter as a consequence of the absorption of a photon of energy ( $h\nu$ ), and may be referred to as photoelectrons. According to the conservation of energy, the detected kinetic energy ( $E_{kin}$ ) of the photoelectron implies that

$$E_{kin} = h\nu - \Phi - |E_B|, \quad (2.1)$$

where  $\Phi$  is the work function and  $E_B$  is the binding energy of the electrons.

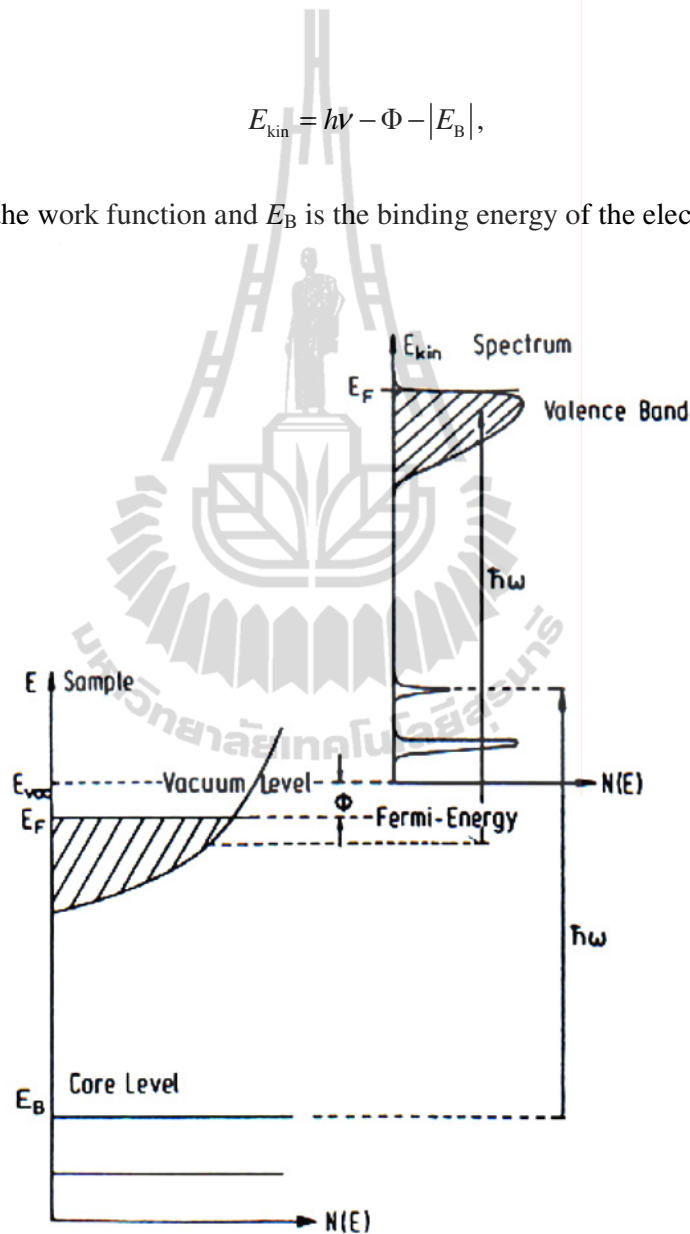


**Figure 2.1** A schematic relation between the electron energy distribution of photoemitted electrons and the density of state of a metallic solid (Hüfner, 1995).

### 2.1.2 The three step model

There are two models to formulate the photoemission process; the one- and three-step models as shown in Figure 2.2. The three step model has been developed by Berglund and Spicer (1964), which presents a first approach to phenomenological description to PES. This approach is based on three processes; the electron is excited from ground state, the excited electron transports to the surface, and finally the electron escapes through the surface into the vacuum. All of these steps are treated independent of each other. For a system that the electrons interact with an oscillating electromagnetic field, the original Hamiltonian is given by

$$H_{\text{int}} = \frac{e}{2mc} (\mathbf{A} \cdot \mathbf{p} + \mathbf{p} \cdot \mathbf{A}) = \frac{e}{mc} (\mathbf{A} \cdot \mathbf{p}), \quad (2.2)$$

where  $\mathbf{A}$  is the electromagnetic vector potential and  $\mathbf{p}$  is the momentum operator.

According to the Fermi's golden rule, the transition rate between initial states  $|\psi_i\rangle$  with energy  $E_i$  and final states  $|\psi_f\rangle$  with energy  $E_f$  can be written as

$$w_{i \rightarrow f} = \frac{2\pi}{\hbar} \left| \langle \psi_f | \mathbf{A} \cdot \mathbf{p} | \psi_i \rangle \right|^2 \delta(E_f - E_i - h\nu). \quad (2.3)$$

For a solid with a periodic potential lattice, the significant quantum numbers of the initial (occupied) and final (empty) states are the Bloch vector  $\mathbf{k}_i$  and  $\mathbf{k}_f$ , respectively. Therefore, Eq. (2.3) can be write out the explicitly  $\mathbf{k}$ -dependence as

$$w_{i \rightarrow f} = \frac{2\pi}{\hbar} \left| \langle \psi_f, \mathbf{k}_f | \mathbf{A} \cdot \mathbf{p} | \psi_i, \mathbf{k}_i \rangle \right|^2 \delta(E_f - E_i - h\nu). \quad (2.4)$$

From Eq. (2.4), the total photoabsorption can be written as

$$I_{\text{abs}} \propto \sum_{\mathbf{k}_f, \mathbf{k}_i} \left| \langle \psi_f, \mathbf{k}_f | \mathbf{A} \cdot \mathbf{p} | \psi_i, \mathbf{k}_i \rangle \right|^2 \delta(E_f - E_i - h\nu). \quad (2.5)$$

In the one step model, the electron from the initial state is excited into a free electron like in vacuum and decays inside the crystal. In particular, the final photoelectron state has to be calculated as a solution of the semi-infinite crystal as called time reversed LEED state (Mahan, 1970; Feibelman and Eastman, 1974; Pendry, 1976). Due to the Bloch form of the one-electron wave functions, the momentum conservation of the matrix element in Eq. (2.4) is given by

$$|\langle \mathbf{k}_f | \mathbf{A} \cdot \mathbf{p} | \mathbf{k}_i \rangle|^2 = |M_{if}|^2 \delta(\mathbf{k}_f - \mathbf{k}_i - \mathbf{G}), \quad (2.6)$$

where  $\mathbf{G}$  is a surface reciprocal lattice vector. However, the three-step model is most commonly used in the description of photoemission data it is easily accessible if they do not interfere in each step.

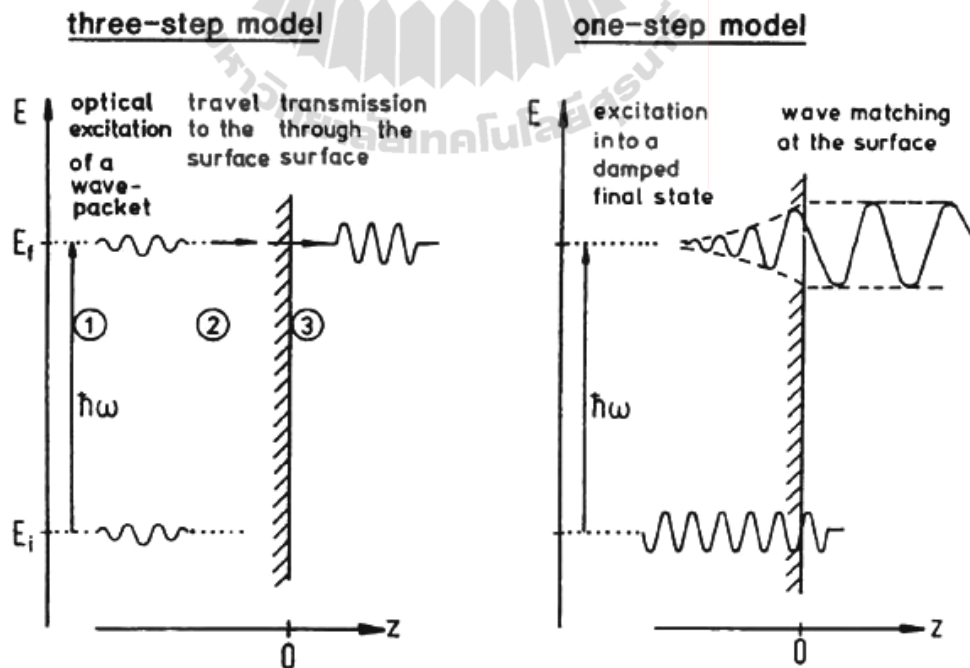


**Figure 2.2** A schematic diagram of the three-step and the one-step models used to describe ARPES processes (Hüfner, 1995).

### 2.1.3 Angle-resolved photoemission

In the past, there were no experimental methods for band mapping, or direct determination of the band structure until the development of ARPES. ARPES gives a very powerful technique used to probe the occupied electron of both bulk and surface states. It is the most direct method for the study of the electronic band structure of surfaces and extensively used to study simple one-dimensional (1D) and two-dimensional (2D) systems. Furthermore, the more complex three-dimensional (3D) systems have been quite successful in establishing the electronic structure of materials. Based on the basic principle of PES, one can determine the momentum of the emitted electron from the measured  $E_{\text{kin}}$  by equation as follows;

$$E_{\text{kin}} = \frac{p^2}{2m}, \quad (2.7)$$

$$p = |\vec{p}| = \sqrt{2mE_{\text{kin}}}.$$

Since the direction of  $\vec{p}$  is determined from the polar and azimuthal angles  $\theta$  and  $\varphi$  with respect to the surface as shown in Figure 2.3, which can be decomposed into the components of  $\vec{p}$  parallel to the surface ( $p_{\parallel}$ ) and perpendicular to the surface ( $p_{\perp}$ ). For crystals with ordered surfaces, there is a periodicity along the surface plane. Thus, the momentum of emitted electrons parallel to the surface is conserved, and the parallel component of the electron crystal momentum is given by

$$\begin{aligned} |p_{\parallel}| &= \hbar k_{\parallel} = \sqrt{2mE_{\text{kin}}} \cdot \sin \theta, \\ k_{\parallel} &= 0.512 \sqrt{E_{\text{kin}}} \cdot \sin \theta \quad (\text{\AA}^{-1}), \end{aligned} \quad (2.8)$$

where  $k_{\parallel}$  is the wave vector of the outgoing photoelectron.

Therefore, the energy band structures parallel to the crystal surface is given by measuring the photoemission spectrum with different angles of outgoing electron. On the other hand, the translation symmetry is broken in the surface normal. Hence the out-of-plane momentum ( $p_{\perp}$ ) component is not conserved. So, the component of wave vector normal to the crystal surface ( $k_{\perp}$ ) is not known experimentally. In order to determine  $k_{\perp}$ , one often assumes that the final states can be approximated by a free-electron-like dispersion and describes the energy of excited photoelectron as

$$E_{\text{kin}} + V_0 = \frac{\hbar^2 \mathbf{k}^2}{2m}, \quad (2.9)$$

where  $V_0$  is the so-called inner potential of the crystal referenced to the vacuum level. To obtain the  $k_{\perp}$ , energy band dispersions can be fitted by  $V_0$  as a fitting parameter. In this model, the  $k_{\perp}$  can be written as

$$\begin{aligned} k_{\perp} &= \frac{1}{\hbar} \sqrt{2m(E_{\text{kin}} \cos^2 \theta + V_0)} \\ &= (0.51) \sqrt{(E_{\text{kin}} \cos^2 \theta + V_0)} \quad (\text{\AA}^{-1}). \end{aligned} \quad (2.10)$$

For the determination of  $V_0$ , three methods are available: (1)  $V_0$  is adjusted to optimize the occupied states between experimental and theoretical band structures, (2) by using the value of the theoretical muffin-tin zero or (3) by observing the symmetries in the experimental  $E(k_{\perp})$  curves. If the sample is irradiated by the synchrotron radiation, a tunable photon source is available. Then, the wave vector perpendicular to surface can be obtained from:

$$k_{\perp} = (0.51) \sqrt{E_{\text{kin}} + V_0} \quad (\text{\AA}^{-1}). \quad (2.11)$$

If the excitation energy is increased, the electron mean free path (Figure 2.4) also changes depending on the kinetic energy of electrons. Since this approach failed to explain in solids with strongly anisotropic crystal structure (Strocov et al., 1997, 1998), it remains unsatisfactory for accuracy band mapping. Here, band mapping is used to determine the band dispersion  $E(\mathbf{k})$  in a crystalline solid, the three-dimensional wave vector  $\mathbf{k} = (k_{\perp}, k_{\parallel})$  is known. In the ARPES experiment, the wave vector parallel ( $k_{\parallel}$ ) and perpendicular ( $k_{\perp}$ ) to the surface can be obtained by measuring intensity of photoelectrons emitted as a function of angle and photon energy, respectively. Then, the dispersions of the band can be obtained by a plot in the binding energy as a function of the wave vector that calculated from Eq. (2.8) and Eq. (2.10).

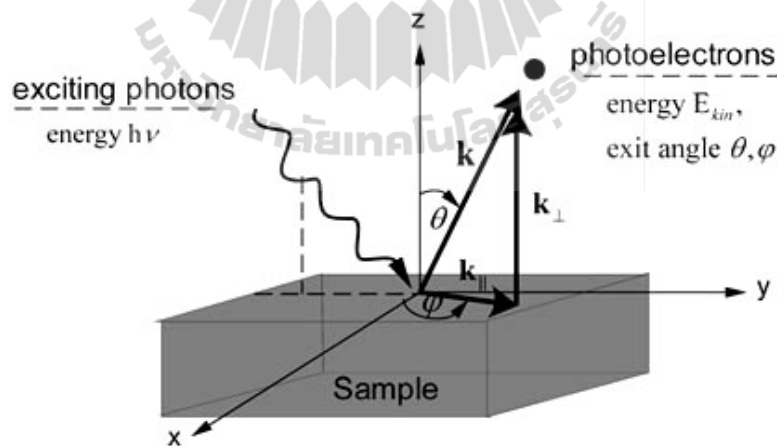


**Figure 2.3** A schematic drawing of the geometry of an angular resolved photoemission experiment.  $h\nu$  is the photon energy,  $\vartheta$  and  $\varphi$  are the polar and azimuthal angles of the emitted electrons, and  $E_{kin}$  is the kinetic energy of the detected photoelectron (Schattke and Van Hove, 2003).

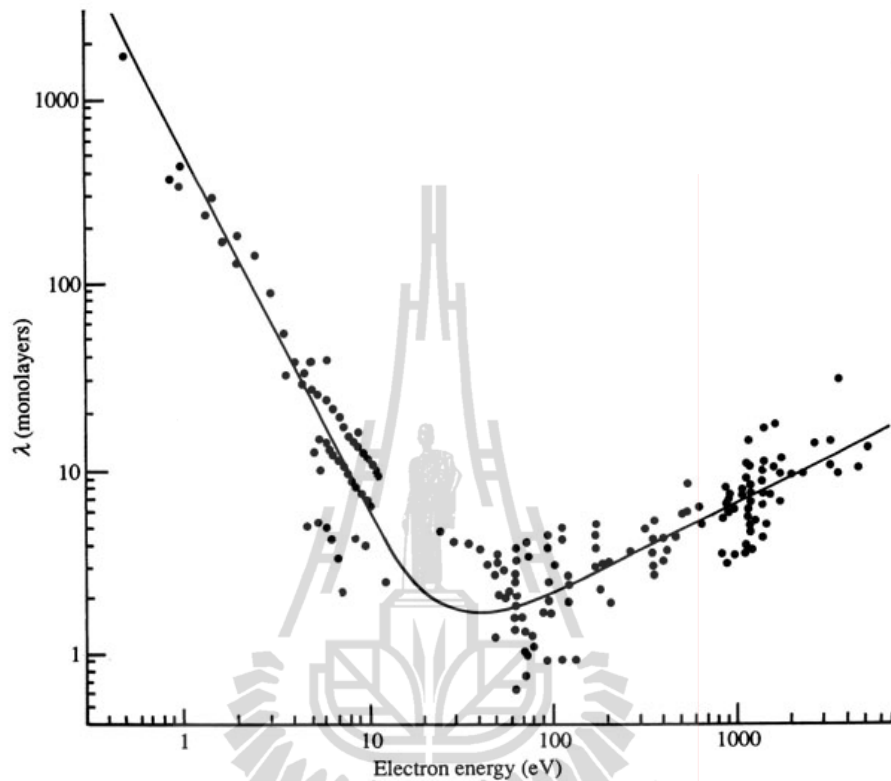


**Figure 2.4** The attenuation length plotted as a function of the electron kinetic energy. The dots correspond to the attenuation lengths measured in many different materials (Briggs and Seah, 1996).

#### 2.1.4 Dipole selection rules

Since the bands in the solid have distinct symmetry properties, dipole selection rules are very important in analyzing data from photoemission experiment, in particular if polarized light is used. Dipole selection rules can be used to consider the possible transitions between electronic states of distinct symmetries in a direct transition. Non-relativistic dipole selection rules for direct interband transitions in a fcc structure were summarized by Hermanson (1977). The dipole selection rules can be identified in the special cases form of photoemission in a mirror plane and the

normal emission. If we consider a transition located at the high symmetry lines of fcc BZ (see Figure 2.5). In normal photoemission along  $\Delta$  line (normal to (100) faces),  $\Sigma$  (normal to (110) faces), or  $\Lambda$  (normal to (111) faces), the final state has to be totally symmetric, i.e.  $\Delta_1$ ,  $\Sigma_1$ , or  $\Lambda_1$ . Under these conditions, the dipole-allowed transitions for normal emission from low-index faces of cubic metals are listed in Table 2.1. As an example from (100) faces, the  $\Delta_1$  and  $\Delta_5$  initial states are only excited in normal emission. In the case of  $p$ -polarized light (Figure 2.6), which the polar angles of incidence are large, a  $\Delta_1$  states is excited. On the other hand, excitation of  $\Delta_5$  states requires the  $s$ -polarized (Figure 2.6). From Table 2.1, it can be concluded that, in comparison with the ARPES data, one has to consider what final states can contribute to the photoemission process. However, the dipole selection rules listed in Table 2.1 are broken for off-normal emission. In order to determine the surface state symmetry of an angular distribution, photoemission measurement should be performed using mirror plane emission in polarized light (Dietz, Becker, and Gerhardt, 1975; 1976; Plummer and Eberhardt, 1979). In a mirror plane, the final states have to be even with respect to that mirror planes. The dipole operator  $\mathbf{A} \cdot \mathbf{p}$  is even (odd) if  $\mathbf{A}$  is parallel (perpendicular) to the mirror plane. Thus only even (odd) initial states can be observed.

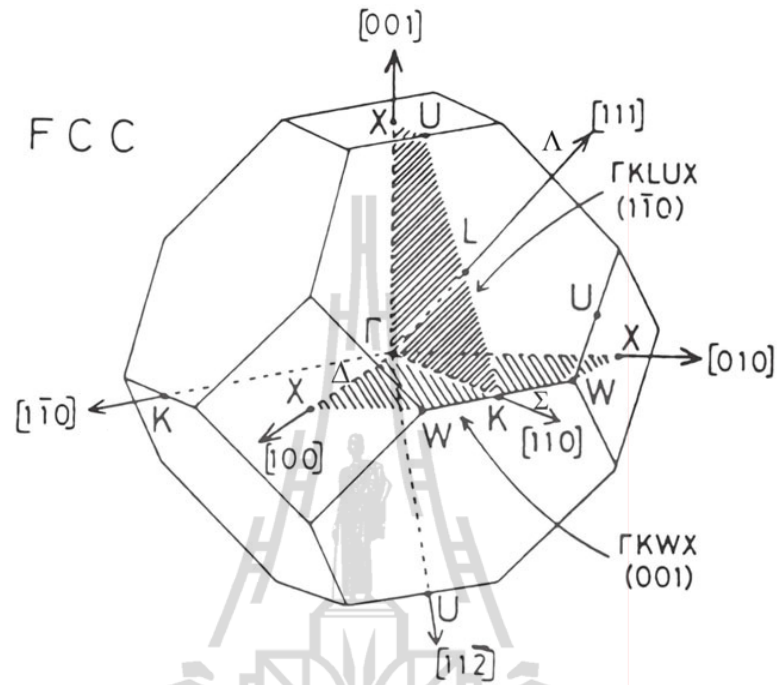


**Figure 2.5** Bulk Brillouin zone for the fcc lattice indicated with several high-symmetry lines (Hüfner, 1995).

**Table 2.1** Dipole selection rule using linear polarized light coming to single crystal surface (Hermanson, 1977).

| <b>Normal emission (nonrelativistic)</b> |                                 |                                       |                           |             |
|--|---------------------------------|---------------------------------------|---------------------------|-------------|
| Crystal plane                            | Final state                     | Allowed initial state                 |                           |             |
| (001)                                    | $\bar{A} \parallel [100]$       | $\bar{A} \parallel [010]$             | $\bar{A} \parallel [001]$ |             |
|  | $\Delta_1$                      | $\Delta_5$                            | $\Delta_5$                | $\Delta_1$  |
| (110)                                    | $\bar{A} \parallel [001]$       | $\bar{A} \parallel [1\bar{1}0]$       | $\bar{A} \parallel [110]$ |             |
|  | $\Sigma_1$                      | $\Sigma_3$                            | $\Sigma_4$                | $\Sigma_1$  |
| (111)                                    | $\bar{A} \parallel [\bar{1}10]$ | $\bar{A} \parallel [\bar{1}\bar{1}2]$ | $\bar{A} \parallel [111]$ |             |
|  | $\Lambda_1$                     | $\Lambda_3$                           | $\Lambda_3$               | $\Lambda_1$ |

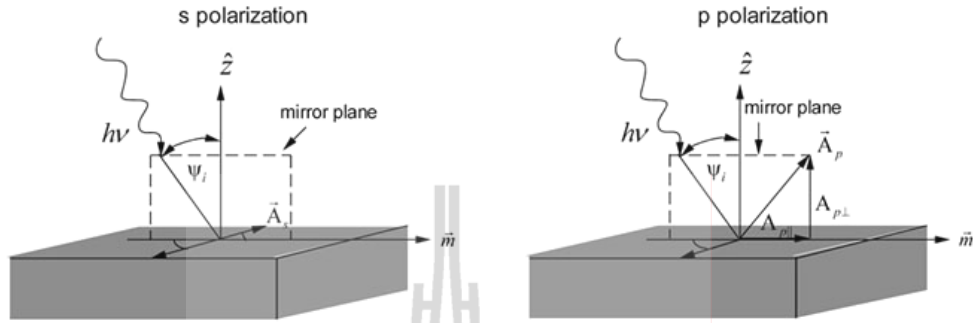


**Figure 2.6** Definition of directions used in a photoemission experiment with  $s$  and  $p$  polarized light. The incident light and detected electrons are in a mirror plane (Hüfner, 1995).

### 2.1.5 Spectral representation

Within the sudden approximation, the transition matrix element can be considered in the simplest approximation as one-electron view. In the one-electron approximation, the initial-state wave function for system consisting  $N$  electrons can be written as

$$\psi_i(N) = C\phi_{ik}\psi_{ik,R}(N-1), \quad (2.12)$$

where  $\psi_{ik,R}(N-1)$  is the wave function of the remaining electrons,  $\phi_{ik}$  is the one-electron orbital and  $C$  is the antisymmetrizing wave function operator.

Similarly, the final state is then written as

$$\psi_f(N) = C\phi_{fk}\psi_{fk,R}(N-1). \quad (2.13)$$

Thus, we can write the transition matrix element from Eq. (2.3) in the form

$$\langle \psi_f | H_{\text{int}} | \psi_i \rangle = \langle \phi_{fk} | H_{\text{int}} | \phi_{ik} \rangle \langle \psi_{fk,R}(N-1) | \psi_{ik,R}(N-1) \rangle. \quad (2.14)$$

Here, assume that the final state with  $N-1$  electrons has the energy  $E_s(N-1)$ , which  $s$  is the number of states. So, the photoelectron current detected in PES experiment can then expressed as

$$I \propto \sum_{f,i,k} \left| \langle \phi_{fk} | H_{\text{int}} | \phi_{ik} \rangle \right|^2 \sum_s |c_s|^2 \delta(E_{fk} + E_s(N-1) - E_0(N) - \hbar\omega), \quad (2.15)$$

where  $|c_s|^2 = \left| \langle \psi_{fk,R}(N-1) | \psi_{ik,R}(N-1) \rangle \right|^2$  is the probability of the electron that leave from the  $N$  electron ground state in the excited state  $s$  of the  $N-1$  electron system and  $E_0(N)$  is the ground state energy of the system consisting  $N$  electrons.

For solids, Eq. (2.15) can be rewritten in the form

$$I \propto \sum_{f,i,k} \left| \langle \phi_{fk} | H_{\text{int}} | \phi_{ik} \rangle \right|^2 A^<(\mathbf{k}, E), \quad (2.16)$$

where  $A^<(\mathbf{k}, E)$  is the single-particle spectral function and can be connected to the single-particle Green's function by

$$A^<(\mathbf{k}, E) = \frac{1}{\pi} \text{Im} [G(\mathbf{k}, E)] f(E, T), \quad (2.17)$$

where  $f(E, T)$  is the Fermi-Dirac function. For free particles with the one-electron band energy  $\varepsilon_{\mathbf{k}}^0$ , the Green's function can defined as (Mahan, 1981)

$$G_0(\mathbf{k}, E) = \frac{1}{E - \varepsilon_{\mathbf{k}}^0}, \quad (2.18)$$

and the spectral function is given by

$$A_0^<(\mathbf{k}, E) = \delta(E - \varepsilon_{\mathbf{k}}^0) f(E, T), \quad (2.19)$$

The spectral function is a  $\delta$ -function at the energies of the single particle states.

In an interacting electron system, the electron energy can be represented in terms of a complex self-energy  $\Sigma(\mathbf{k}, E) = \text{Re}[\Sigma(\mathbf{k}, E)] + i \text{Im}[\Sigma(\mathbf{k}, E)]$ , one finds

$$G(\mathbf{k}, E) = \frac{1}{E - \varepsilon_{\mathbf{k}}^0 - \Sigma(\mathbf{k}, E)}, \quad (2.20)$$

and

$$A^<(\mathbf{k}, E) = \frac{1}{\pi} \frac{\text{Im}\{\Sigma(\mathbf{k}, E)\}}{\left[E - \varepsilon_{\mathbf{k}}^0 - \text{Re}\{\Sigma(\mathbf{k}, E)\}\right]^2 + \left[\text{Im}\{\Sigma(\mathbf{k}, E)\}\right]^2} f(E, T). \quad (2.21)$$

Here, the self energy effects are directly reflected in the electron removal spectrum.

### 2.1.6 Photocurrent measured by ARPES

In the ARPES experiment the specified energy  $E$  and momentum  $\mathbf{K}$  of free photoelectrons are measured. Therefore, only absorption into final states with  $E = E_f$  is detected. The momentum component parallel to the surface is conserved, with arbitrary surface reciprocal lattice vector  $\mathbf{G}_{\parallel}$ :  $\mathbf{K}_{\parallel} = \mathbf{k}_{f\parallel} + \mathbf{G}_{\parallel}$ . Therefore, the photoelectron current at a fixed  $E$  and  $k_{\parallel}$  are expressed as

$$I(\mathbf{K}, E) \propto \sum_{\mathbf{k}_f, \mathbf{k}_i} \left| \langle \mathbf{k}_f | \mathbf{A} \cdot \mathbf{p} | \mathbf{k}_i \rangle \right|^2 \delta(E_f - E_i - h\nu) \times \delta(\mathbf{K}_{\parallel} - \mathbf{k}_{f\parallel} - \mathbf{G}_{\parallel}) \delta(E - E_f). \quad (2.22)$$

According to the matrix element of the one-electron model in Eq. (2.6), we can rewrite Eq. (2.22) into

$$I(\mathbf{K}, E) \propto \sum_{\mathbf{k}_f, \mathbf{k}_i} \left| M_{if} \right|^2 \delta(E_f - E_i - h\nu) \delta(\mathbf{k}_f - \mathbf{k}_i - \mathbf{G}) \delta(E - E_f) \delta(\mathbf{K}_{\parallel} - \mathbf{k}_{f\parallel} - \mathbf{G}_{\parallel}). \quad (2.23)$$

This expression describes the conservation of energy and the momentum components parallel to the surface during the photoexcitation deep in the solid (first two  $\delta$  functions) and at the solid-vacuum interface (last two  $\delta$ -functions). It is allowed to obtain the initial state band dispersions from energy and momentum of the photoelectrons measured in the ARPES experiment.

## 2.2 Electronic structure of correlated systems

### 2.2.1 Band structures of bulk Cu and Cu(100) surface

The energy band structure of bulk Cu calculated by Segall (1962) and Burdick (1963) is shown in Figure 2.7. Segall further calculated the band structure of bulk Cu based on the Green's function method (Kohn and Rostoker, 1954) with two distinct potentials. One of the potentials was constructed by Manning and Chodorow (1939) whereas another one is obtained from the Hartree-Fock functions of  $3d$  electron for the free  $\text{Cu}^+$  ion. The second potential is renormalized in the Wigner Seitz sphere in order to use the core and  $d$  electron Hartree-Fock functions of Cu. Then Burdick (1963) also calculated the band structure of bulk Cu by the APW method (Slater, 1937; Saffren and Slater, 1953) with the potential created by Manning and Chodorow (1939). The results of this calculation are corresponded to those of Segall for the same potential to within 0.15 eV. In Figure 2.7, the symmetry points are followed to the notation of Bouckaert, Smoluchowski, and Wigner (1936). The  $d$  flat bands are located approximately 2 to 6 eV below  $E_F$ . Therefore, these states are characterized relatively to high density of states according to the flatness of the  $d$  bands. The positions of  $E_F$  and of  $\Phi$  are also indicated in this calculated band. The  $sp$  bands exhibited the contribution as nearly-free-electron bands, while for the more localized

$d$  bands below  $E_F$  these have tight binding character. However, the  $sp$  bands are strongly interacted with the  $d$  bands. The transitions from the  $sp$  bands to the  $d$  bands occurred in the gap of  $L_1 - L_2$ , which the  $L_2'$  eigenvalue is shown by the dashed lines in Figure 2.7.

In particular, the results of bulk band structure of Cu have been used to describe the electronic surface states on the Cu surface. On the Cu(100) surface, the projected bulk band structures observed with both experimental (represented by open squares) and calculated inverse photoemission (IPE) structure (denoted by solid circles) are shown in Figure 2.8. In the IPE experiments (Grass et al., 1993), the four empty surface states  $SR$ ,  $S_1$ ,  $S_2$ ,  $S_3$  and two unoccupied bulk states  $B_1$ ,  $B_2$  have been detected along  $\Gamma XUL$  plane. Since  $SR$  is related to the  $X_{4'} - X_1$  gap denoted as the crystal-induced surface resonance and  $S_1$  denoted the first image-potential state in the same gap. On the other hand,  $S_2$  and  $S_3$  represent crystal-induced surface states that are derived from the  $L_2' - L_1$  gap.  $S_2$  becomes an occupied surface state near  $\bar{X}$  and has been detected in high-resolution PES (Kevan, 1983).

Calculated IPE spectra and the corresponding experimental data ( $\hbar\omega = 9.7$  eV) for different angles of electron incidence for Cu(100) surface along the  $\Gamma XUL$  bulk mirror plane are shown in Figure 2.9. The calculated spectra are obtained by convoluting the raw spectra with a Gaussian of 0.275 eV full width at half-maximum (FWHM). Note that the fraction of secondary emitted photons from the experimental spectra is neglected in the calculations of IPE spectra. Thus, the results from theory and experiment are in good agreement. In particular, the calculated IPE spectra are well reproduced in the polarization dependence of the intensity for the various peaks. These calculated IPE spectra for Cu(100) found that only the surface state  $S_2$  at  $\bar{X}$  is

considered as non-zero current for photons polarized in the surface plane. The comparison between the calculated surface states along the symmetry points of  $\bar{\Gamma}$  to  $\bar{X}$  with experimental data for Cu(100) is also summarized in Table 2.2. The energetic positions and effective masses are within the error bars of the experiment. The other study of IPE of Cu(100) at various photon energies found the surface state at the zone boundary  $\bar{X}$  with energy about 0.5 eV (Lange et al., 1990), which is not included in Table 2.2. In addition, the experimental IPE spectra show dispersionsless features in the range of 0-1.5 eV above the  $E_F$ . These features could be described as the transitions into weak maxima of the three-dimensional density of states (DOS) in this energy range.

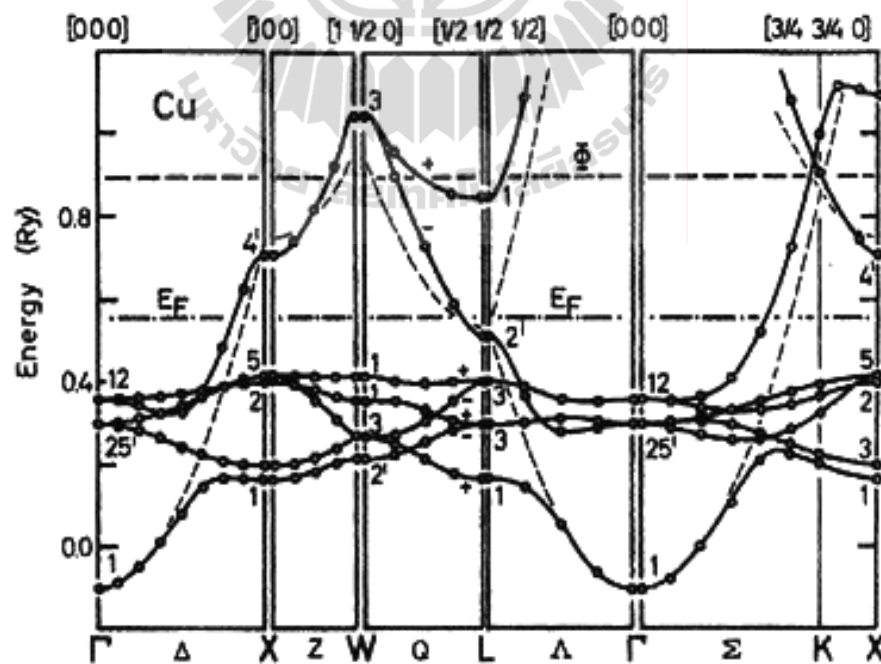


**Figure 2.7** Band structure of Cu along some symmetry points as calculated by Segall (1962) and Burdick (1963). The dashed curves represented the free electron eigenvalues.

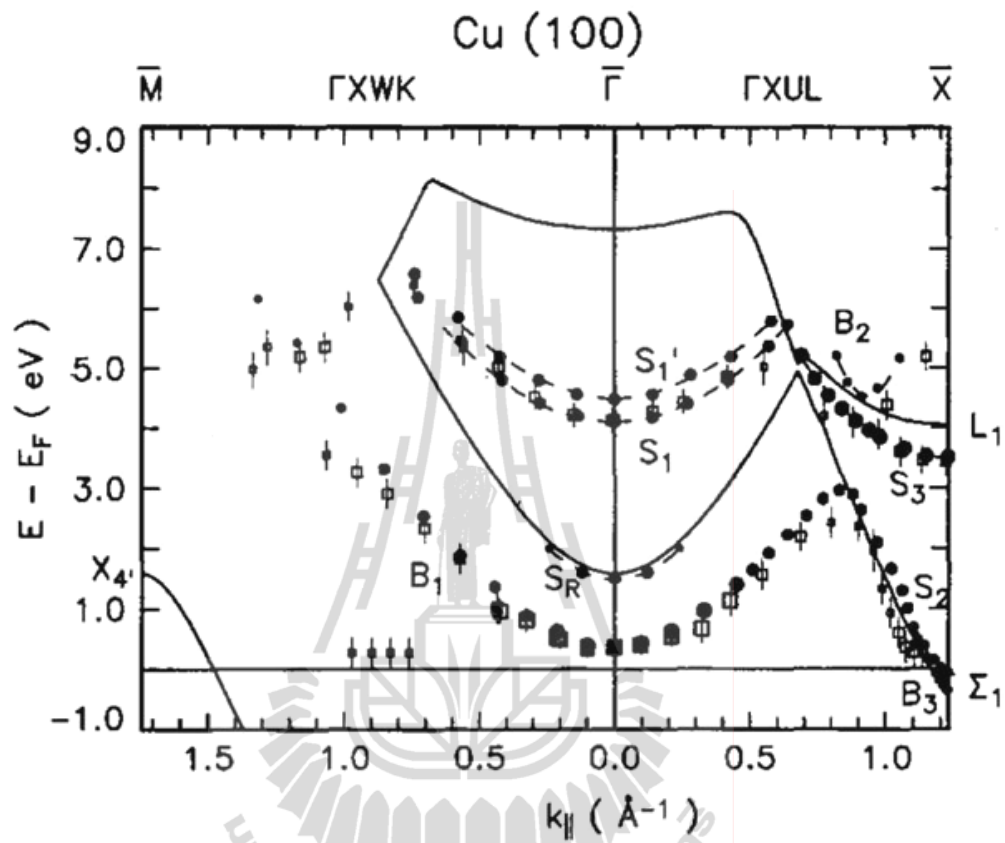


**Figure 2.8** Projected bulk band structure for Cu(100) onto the surface BZ along the  $\bar{\Gamma}$ - $\bar{X}$  and  $\bar{\Gamma}$ - $\bar{M}$  directions. Solid circles and open squares with error bars are indicated the calculated and measured band dispersions, respectively (Grass et al., 1993).

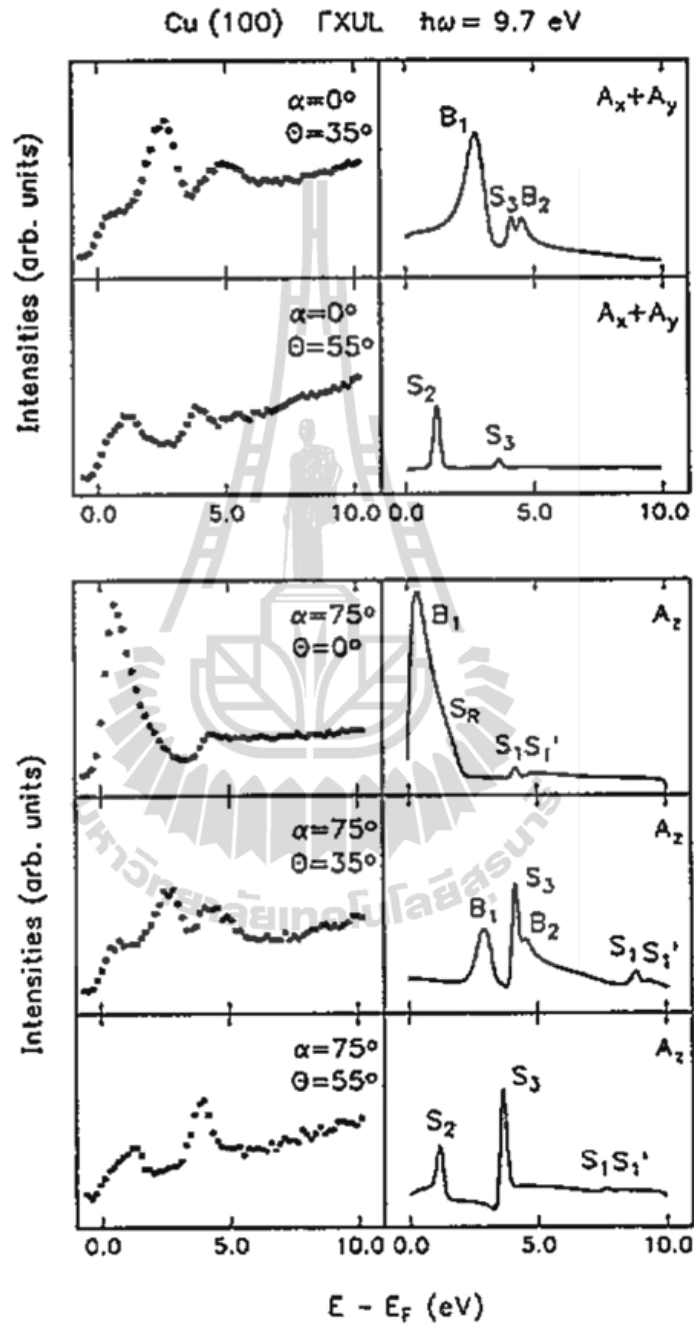


**Figure 2.9** Experimental (left) and theoretical (right) inverse photoemission spectra ( $\hbar\omega = 9.7$  eV) for Cu(100) along the  $\Gamma$ XUL bulk mirror plane.  $\Theta$  is represents the angle of electron incidence and  $\alpha$  denotes the photon detection angle (Grass et al., 1993).

**Table 2.2** Comparison of experiment and calculated binding energies and effective masses of surface states on Cu(100) (Grass et al., 1993).

| Symmetry point | Type   | $E-E_F$ (eV)<br>(theor.) | $m^*/m_e$<br>(theor.) | $E-E_F$ (eV)<br>(exp.) | $m^*/m_e$ (exp.)   |
|----------------|--------|--------------------------|-----------------------|------------------------|--------------------|
|                |        |                          |                       | $4.13 \pm 0.20^a$      |                    |
| $\bar{\Gamma}$ | $S_1$  | 4.10                     | 0.990                 | $4.00 \pm 0.20^b$      | $1.2 \pm 0.20^b$   |
|                |        |                          |                       | $4.06 \pm 0.20^c$      | $0.90 \pm 0.10^c$  |
| $\bar{\Gamma}$ | $S'_1$ | 4.48                     | 1.010                 | $4.45 \pm 0.20^c$      |                    |
|                |        |                          |                       | $1.15^d$               |                    |
| $\bar{\Gamma}$ | $S_R$  | 1.50                     | 0.427                 | $1.20 \pm 0.30^a$      |                    |
|                |        |                          |                       | $1.48 \pm 0.06^e$      |                    |
| $\bar{X}$      | $S_2$  | -0.065                   | 0.076                 | $-0.058 \pm 0.025^f$   | $0.067 \pm 0.01^f$ |
| $\bar{X}$      | $S_3$  | 3.52                     | 0.630                 | $3.60 \pm 0.02^g$      | $0.70 \pm 0.02^g$  |
|                |        |                          |                       | $3.45 \pm 0.02^a$      |                    |

<sup>a</sup>Schneider et al. (1990).

<sup>b</sup>Dose et al. (1984).

<sup>c</sup>Steinmann (1989).

<sup>d</sup>Woodruff, Hulbert, and Johnson (1985).

<sup>e</sup>Wegehaupt, Rieger, and Steinmann (1988).

<sup>f</sup>Kevan (1983).

<sup>g</sup>Donath et al. (1986).

### 2.2.2 Band structures of bulk Ni and Ni(100) surface

The calculated bulk band structure for Ni along high symmetry directions has been obtained by the empirically fitting using a combined interpolation scheme as shown in Figure 2.10, which is proposed by Weling and Callaway (1982). These empirical adjusted band structures are determined by results of ARPES (Eastman, Himpsel, and Knapp, 1978; Dietz, Gerhardt, and Maetz, 1978; Himpsel, Knapp, and Eastman, 1979; Eberhardt and Plummer, 1980). The point across the  $E_F$  has been determined using an accurate Fermi surface data. This approach does not include the effect of the spin orbit interaction. The interpolation results of this method comparing with the experimental data of Eberhardt and Plummer (1980) are given in Table 2.3. The parameters of the paramagnetic band structure are determined from the averages data of spin up and spin down levels. The effects of exchange splitting have been included in the calculations in order to obtain the ferromagnetic band structure. From this fitting procedure, the computed  $E_F$  and the magnetic moment for Ni are given by:

$$E_F = 0.0548 \text{ eV and } m = 0.56 \mu_B.$$

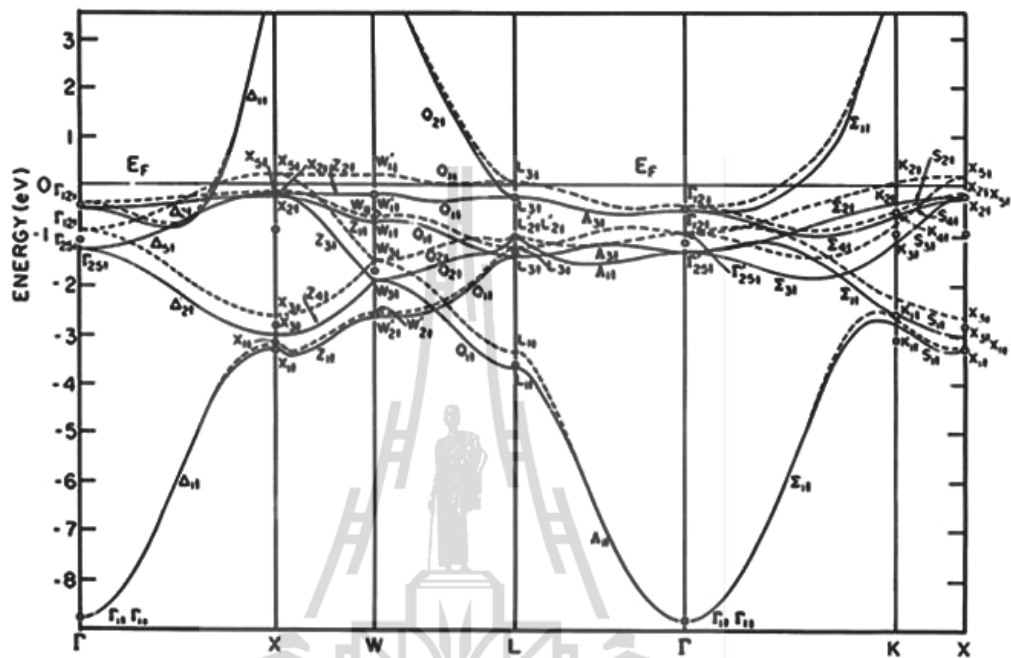


**Figure 2.10** The empirical bulk band structure of Ni along certain symmetry lines in the Brillouin zone. The solid (dash) lines represented majority (minority) states of spin. The squares indicated the experimental values (Weling and Callaway, 1982).

**Table 2.3** The energy levels in the units of electron volts at symmetry points of Ni (Eberhardt and Plummer, 1980).

| Symmetry       | Experiment <sup>a</sup> |                 | Theory <sup>c</sup> |         | Fit <sup>d</sup> |           |
|----------------|-------------------------|-----------------|---------------------|---------|------------------|-----------|
|                | average <sup>b</sup>    | spin-up         | average             | average | spin-up          | spin-down |
| $\Gamma_1$     | $-8.8 \pm 0.2$          |                 | -8.93               |         | -8.8000          | -8.8000   |
| $\Gamma_{25}'$ | $-1.1 \pm 0.2$          |                 | -2.04               |         | -1.3000          | -0.9000   |
| $\Gamma_{12}$  | $-0.4 \pm 0.1$          |                 | -0.92               |         | -0.4500          | -0.3500   |
| $X_1$          | $-3.3 \pm 0.2$          |                 | -4.31               | -3.24   | -3.2789          | -3.1942   |
| $X_3$          | $-2.8 \pm 0.2$          |                 | -3.81               |         | -3.0000          | -2.6000   |
| $X_2$          | $-0.85 \pm 0.1$         |                 | -0.18               | -0.16*  | -0.2079          | -0.1079   |
| $X_5$          |                         |                 | 0.02                | 0.05    | -0.1500          | 0.2500    |
| $L_1$          | $-3.6 \pm 0.2$          |                 | -4.63               | -3.50   | -3.6638          | -3.3413   |
| $L_{31}$       | $-1.3 \pm 0.1$          |                 | -2.07               |         | -1.4035          | -1.2045   |
| $L_{2}'$       | $-1.0 \pm 0.2$          |                 | -0.40               |         | -1.0000          | -1.0000   |
| $L_{32}$       |                         | $-0.2 \pm 0.1$  | -0.17               | -0.06*  | -0.2016          | 0.0994    |
| $W_{2}'$       | $-2.6 \pm 0.2$          |                 | -3.59               |         | -2.6422          | -2.5583   |
| $W_3$          | $-1.7 \pm 0.2$          |                 | -2.77               |         | -1.8937          | -1.5067   |
| $W_1$          | $-0.65 \pm 0.1$         |                 | -1.00               |         | -0.6998          | -0.6000   |
| $W_{1}'$       |                         | $-0.15 \pm 0.1$ | 0.02                |         | -0.1500          | 0.2500    |
| $K_1$          | $-3.1 \pm 0.2$          |                 | -3.66               | -2.70   | -2.7549          | -2.6549   |
| $K_1$          | $-2.55 \pm 0.1$         |                 | -3.45               | -2.40   | -2.5787          | -2.2119   |
| $K_3$          | $-0.9 \pm 0.2$          |                 | -1.81               |         | -1.0916          | -0.7088   |
| $K_4$          | $-0.45 \pm 0.1$         |                 | -0.77               | -0.50*  | -0.5492          | -0.4492   |
| $K_2$          |                         |                 | -0.25               | -0.09   | -0.2881          | 0.1119    |

<sup>a</sup>Eberhardt and Plummer (1980). The experimental Fermi energy was chosen as zero of energy.

<sup>b</sup>Average over the spin directions.

<sup>c</sup>Theory by Wang and Callaway (1974) using vBH potential.

<sup>d</sup>The values of the energy levels, which have not been used for fit, are only indicated for the sake of clarity.

\*The readjusted input values. As for the column based on experiment, the values are given relative to the experimental Fermi energy.

In order to study the surface band of Ni, Zhu and Hermanson (1984) have calculated the electronic structure of five-plane films of ferromagnetic Ni(100) with the use of an atomic orbital basis, as shown in Figure 2.11. According to the experimental results from Plummer and Eberhardt (1979), who studied the surface band dependence on the polarization of the incident light, the results of band structures depend on their parity. This calculation based on the linear combination of atomic orbitals method (LCAO) by Dempsey and Kleinman (1977) suggested that the observed two surface bands using ARPES (Plummer and Eberhardt, 1979; Erskine, 1980) near  $\bar{M}$  and  $\bar{\Gamma}$  may be considered to the  $\bar{M}_3\bar{\Sigma}_2\bar{\Gamma}_5$  band. The calculated band structure shows that the most of electron are accumulated at the surface near  $E_F$  (denoted by solid circles) with more than 60%. The surface states may be attributed from these states. However, this calculation has not distinguished between surface states and surface resonances. The majority  $d$  bands of Ni surface are almost completely filled due to these electrons are essentially confined to the lattice site. Therefore these electrons have a more localized character. In particular, this calculation predicted an enhancement of the surface magnetic moment by 8% compared with the bulk value denoted by a center plane of  $0.55 \mu_B$ . In addition, The surface magnetic moment under the constraint for Ni(100) surface has also been considered by Tersoff and Falicov (1982). They found that the surface magnetic moment of Ni(100) increased to be  $0.74 \mu_B$  larger than the bulk moment of 32%. These results are corresponded to the first-principles calculations even though the calculation of exchange splitting is overestimated due to the neglected correlation effects. On the other hand, Zhu and Hermanson (1984) suggested that the reduction of magnetism for the contracted film was due to the creation of holes in majority  $d$  band.

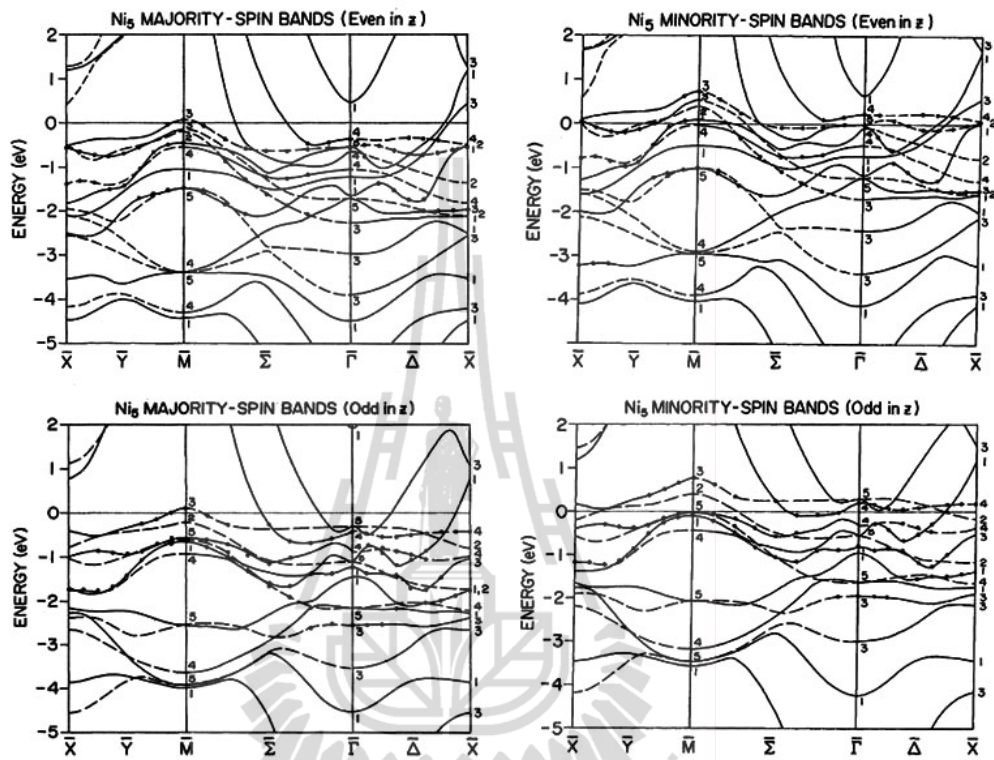


**Figure 2.11** Calculated spin-resolved surface electronic states in a five-plane Ni(100) film. The bands are separated into two independent sets according to their spin character (majority or minority) and their parity with respect to reflection in the plane of incident at the surface plane (even or odd) (Zhu et al., 1984).

## 2.3 Magnetism in thin films

### 2.3.1 Basic concepts in the magnetism

The origin of magnetism and the magnetic properties of materials are based on the orbital and spin motions of electrons. Generally, there are five classifications of magnetism: diamagnetism, paramagnetism, ferromagnetism, antiferromagnetism, and ferrimagnetism. The magnetic moments in the first two groups are only order under an external magnetic field. However, the materials in the last three groups exhibit long-range spontaneous magnetic order even with no applied external field below a certain critical temperature (Curie temperature,  $T_C$ ). The energy concerned in the transition from the ferromagnetic to the paramagnetic state is of the order of  $k_B T_C / \text{atom}$  ( $\cong 0.1$  eV/atom). The mechanism that driven the formation of a long-range magnetically ordered ground state in the material is so-called exchange interaction, which is in the different energies for the parallel and antiparallel spin states as an effect of the Pauli principle and the Coulomb interaction between electrons. This is the atomic origin of ferromagnetism.

In the solid state magnetism, the elements playing a fundamental role in ferromagnetism are the  $3d$  transition metals and the  $4f$  rare earths elements because the shell is incompletely filled. Normally, there are two models applied to explain the ferromagnetism of solids, so-called localized and itinerant (delocalized) models. The magnetic moments of the localized model are occurred from unpaired electrons in localized wave functions. This is mostly found in  $3d$  metal oxides,  $4f$  metals and their compounds, which are well described by the Heisenberg and Ising systems. While for the itinerant (delocalized) model, the unpaired electrons responsible for the magnetic

moments are delocalized close to  $E_F$ , which the classical prototype Fe, Co, and Ni. In order to explain these electrons, the electronic band theories are required.

The original atomic energy levels in the itinerant model are broadened into the narrow bands. The simplest and most frequently applied model has been proposed by Hubbard (1963)

$$H = \sum_{i,j,\sigma} t_{ij} c_{i\sigma}^{\dagger} c_{j\sigma} + U \sum_i n_{i\uparrow} n_{i\downarrow} = H_1 + H_U. \quad (2.24)$$

This model represents an approach for a single band consisting of an electron hopping terms with spin  $\sigma$  between the lattice sites  $i$  and  $j$  and the Coulomb interactions between electrons. Here,  $c_{i\sigma}^{\dagger}$  and  $c_{i\sigma}$  represent the annihilation and creation operators with spin  $\sigma$  at the lattice site  $i$ . However, the Hubbard Hamiltonian has no exact solution to all metals. Therefore, the Stoner-Wohlfarth model (Wohlfarth, 1953) has been proposed to approximate the Hubbard model problem.

In the Stoner-Wohlfarth model, the magnetization is equal to the local magnetization  $M$ , can be written as

$$M = \mu_B \int^{E_F} [D^{\uparrow}(E) - D^{\downarrow}(E)] dE, \quad (2.25)$$

where  $\mu_B$  is the Bohr magnetrons as atomic unit for the magnetic moment. The definition of the magnetization originates from the difference in the DOS between spin up and spin down electrons. Then, the exchange-correlation potential for spin up and spin down electrons can be written as

$$V_{xc}^{\uparrow\downarrow}(\mathbf{r}) = V_{xc}^0(\mathbf{r}) \mp \frac{1}{2} IM. \quad (2.26)$$

Here  $I$  is the Stoner parameter and  $V_{xc}^0(\mathbf{r})$  is the exchange-correlation contribution for the nonmagnetic case. Considering the energy eigenvalues, it displays a symmetric energy splitting as

$$\varepsilon^{\uparrow\downarrow}(\mathbf{k}) = \varepsilon(\mathbf{k}) \mp \frac{1}{2} IM. \quad (2.27)$$

This result describes that a spin-splitting of the electronic bands structure is responsible to the constant value of  $IM$ . If one considers the nonmagnetic band structure, the Stoner criterion is widely used to identify a stable ferromagnetic state at  $T = 0$  K as

$$I \cdot D(E_F) > 1. \quad (2.28)$$

Here  $D(E_F)$  denotes the value of DOS at the  $E_F$  in the nonmagnetic state and  $I$  is the intra-atomic exchange interaction depending on a given element as shown in Figure 2.12. In this model, the paramagnetic energy band state splits into a pair of bands. So, a sufficient condition for ferromagnetism requires a high DOS of the nonmagnetic band structure at  $E_F$  and its bandwidth should be small enough. Therefore, this Stoner criterion is appropriate to describe the relation between electronic structure and magnetism in itinerant systems phenomenologically.

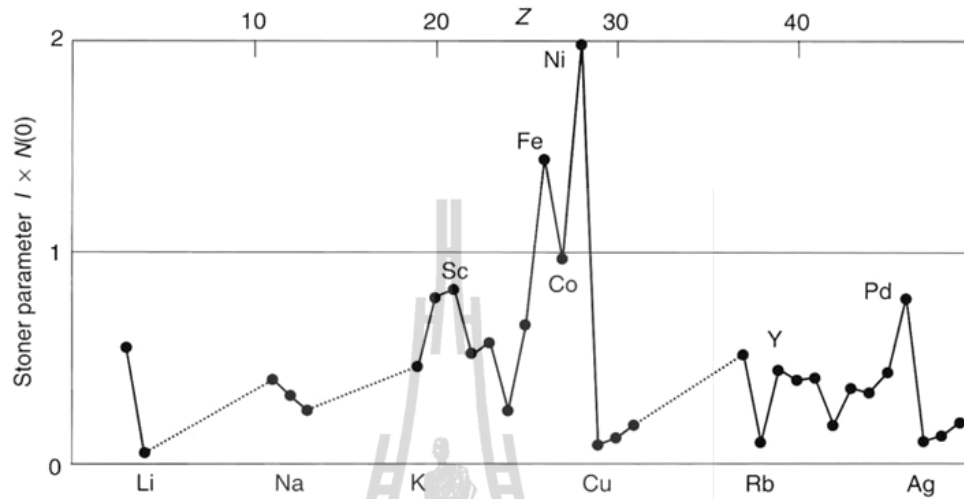


**Figure 2.12** Stoner parameters for the element metals calculated from DOS and spin-dependent mean-field interactions based on density functional theory (Kübler and Eyert, 1992).

### 2.3.2 Surface magnetism

Nowadays, surface magnetism is an active field of research due to its important applications. In particular, the new magnetic properties mostly exhibit at surface. The surfaces and interfaces often exhibit the fundamental magnetic properties different from those in bulks due to the electronic structure or geometric arrangement. Since surface and a monolayer films have lower atomic coordination, leading to reduced overlap of  $d$  electron wave functions and a reduction in bandwidth, DOS at  $E_F$  ( $D(E_F) \sim 1/W_d$ ) increases. This result leads to enhanced magnetic moments. Moreover, the atomic coordination at the surface should also depend on the crystallographic orientation of surface. A following section describes the characteristic features of magnetic properties arising from surface.

### 2.3.2.1 Dimensionality effects

A dimensionality crossover from 3D to 2D behavior is expected when the thickness of a magnetic film decreases to the monolayer limit. Since  $T_C$  in bulk has been defined depending on their composition (Kittel, 1976). However,  $T_C$  in thin film is varied as a function of film thickness. From the results of  $T_C$  dependence on thickness as measured from various epitaxial thin film systems, it was found that the data for Ni were fitted to the bulk relation as

$$n^{-\lambda} \propto \frac{T_C(\text{bulk}) - T_C(n)}{T_C(n)}. \quad (2.29)$$

Here,  $n$  is the number of monolayers (MLs) in the film and  $\lambda$  denoted to the shift exponent. In the case of Ni/Cu(001),  $T_C$  was determined from susceptibility measurement as shown in Figure 2.13 (Bovensiepen et al., 1998).

Considering the 2D systems, the order parameter of spontaneous magnetization at the phase transition from ferromagnetism to paramagnetism was described by a power law of the form

$$M(T) = M(0) \left(1 - \frac{T}{T_C}\right)^\beta, \quad (2.30)$$

where  $\beta$  is the critical exponent of different dimensionality depended on the model of calculation. Determination of critical exponents describes how the magnetization  $M$  vanishes near  $T_C$ . In order to evaluate  $\beta$ , the  $M(T)$  curve with  $T_C$  in the separated experiment should be plotted. For Ni/Cu(100) ultrathin films, the measured values close to 0.24 are characteristic of Ising like systems (Huang et al., 1994).

### 2.3.2.2 Magnetic moments at surfaces

For  $3d$  transition metals, the magnetic moment of itinerant magnetism is determined by the electronic band structure. The electronic band structure splitting due to the exchange interaction leads to a majority and minority bands at the  $E_F$  in different DOS. The average magnetic moment is determined by the difference in the number of occupied states between majority and minority bands. Since the broken symmetry and the reduced coordination number at the surface at a metal surface result in a small value of the  $d$  band width and localized surface states or surface resonance states. These affect to the magnetic properties close to the surface region. Several calculations based on density functional theory (Fu, Freeman, and Oguchi, 1985; Falicov, Victora, and Tersoff, 1985; Freeman and Wu, 1991; Weinert and Blügel, 1993) showed that  $3d$  transition metal atoms may be enhanced the magnetic moment at surface. The calculated results are summarized in Table 2.4. Moreover, the spin-polarized low-energy electron diffraction (SPLEED) experiment provided qualitative agreement with the theoretical predictions for Fe(110), Ni(100) and Ni(111) surfaces (Feder et al., 1983; Mulhollan et al., 1988; Tamura et al., 1990; Wagner et al., 1997).

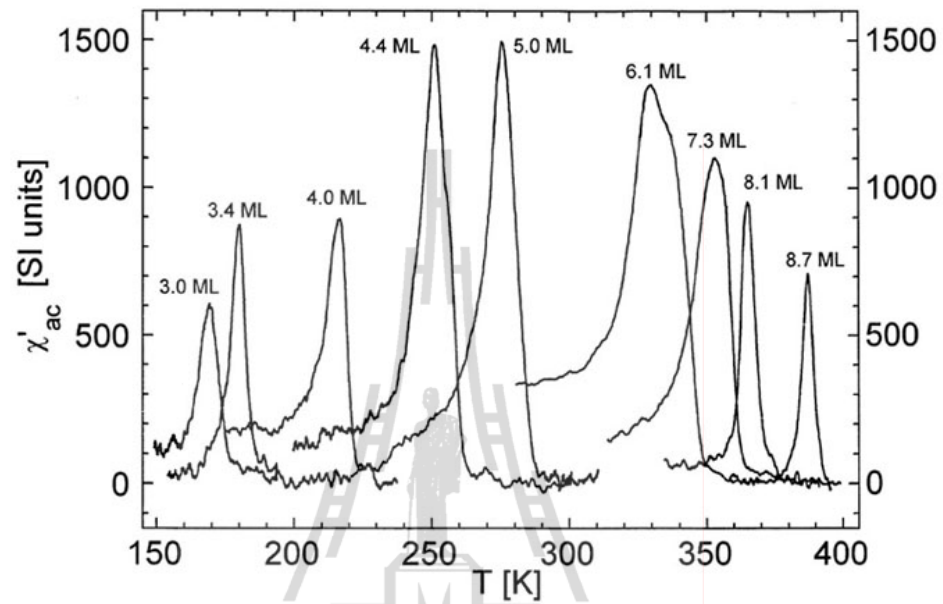


**Figure 2.13** Calibrated in-phase susceptibility versus temperature for several thickness of Ni/Cu(001) (Bovensiepen et al., 1998).

**Table 2.4** Magnetic moments (in  $\mu_B$ ) of 3d transition metal atoms at the surface and in the center layer, and the corresponding enhancement for the surface atoms (Freeman and Wu, 1991).

| System       | Surface | Center | Enhancement (%) |
|--------------|---------|--------|-----------------|
| bcc Fe(001)  | 2.96    | 2.27   | 30              |
| bcc Fe(110)  | 2.65    | 2.22   | 19              |
| bcc Fe(111)  | 2.70    | 2.30   | 17              |
| hcp Co(0001) | 1.76    | 1.64   | 7               |
| fcc Ni(001)  | 0.68    | 0.56   | 23              |
| fcc Ni(110)  | 0.63    | 0.56   | 13              |
| fcc Ni(111)  | 0.63    | 0.58   | 9               |
| fcc Fe(001)  | 2.85    | 1.99   | 43              |
| bcc Co(001)  | 1.95    | 1.76   | 11              |
| bcc Co(110)  | 1.82    | 1.76   | 3               |
| fcc Co(001)  | 1.86    | 1.65   | 13              |
| bcc Cr(001)  | 2.49    | 0.59   | 322             |

## **CHAPTER III**

### **THE CALCULATION METHOD**

A modern computational science based on a quantum-mechanical description of the interactions between electrons and atomic nuclei is one of the most influenced developments in materials science. Eventually, the fundamental basis for understanding materials and phenomena relies on understanding electronic structure. Naturally, the properties of matter are determined by the electronic ground state and the electronic excited states. The stable structure of a specific system is given by the structure with the minimal total energy at zero temperature. So, the ground state total-energy calculations are greatly important for the structural determination of surfaces. This chapter serves as a brief introduction to the calculation method and software used to model the structure involved in this work.

#### **3.1 Density functional theory**

Nowadays, many computational methods are used in materials science for electronic structure calculations. The determination of the total energies is a prerequisite for a theoretical treatment of any property. Normally, two main techniques based on the total energy calculation are available using wave function and electron-density methods. One method has become more popular in recent years is density functional theory (DFT), in which the total energy is expressed in terms of the total electron density, rather than the wave function.

### 3.1.1 The Hohenberg-Kohn theorems

DFT is based on the Hohenberg and Kohn theorem (1964) in which they proved two fundamental mathematical theorems. The first theorem states that the ground-state energy of a system of interacting electrons in an external potential is a functional of the ground state density only  $E[\rho(\mathbf{r})]$ . The second theorem leads to the fundamental statement of DFT that the total energy  $E[\rho(\mathbf{r})]$  is variational with respect to the density and the exact ground state energy and density can be determined by the minimization of the energy functional  $E[\rho(\mathbf{r})]$ .

### 3.1.2 Kohn and Sham equation

Kohn and Sham (1965) who proposed the energy functional of Hohenberg and Kohn theorem in a compact form:

$$E[\rho(\mathbf{r})] = T[\rho(\mathbf{r})] + \int V_{ext}(\mathbf{r})\rho(\mathbf{r}) + \frac{e^2}{2} \iint \frac{\rho(\mathbf{r})\rho(\mathbf{r}')}{|\mathbf{r}-\mathbf{r}'|} d\mathbf{r}d\mathbf{r}' + E_{xc}[\rho(\mathbf{r})], \quad (3.1)$$

where the first term is the kinetic energy functional of the non-interacting electrons system, the second term is the Coulomb interactions between the electrons and the nuclei, the third is so-called Hartree energy and the last term is the exchange-correlation energy that contains the many-electron effects. Kohn and Sham developed the electron density as a sum over the probabilities of single-particle states, can be written as

$$\rho(\mathbf{r}) = \sum_{i=1}^N |\psi_i(\mathbf{r})|^2, \quad (3.2)$$

where  $N$  is the number of electrons.

Since Kohn and Sham reduce the many-electron problem to an essentially single-particle problem with the effective potential  $V_{eff}$  can be written as,

$$V_{\text{eff}}(\mathbf{r}) = V_{\text{ext}}(\mathbf{r}) + \frac{\delta E_{\text{xc}}[\rho(\mathbf{r})]}{\delta \rho(\mathbf{r})} + \int \rho(\mathbf{r}') \frac{1}{|\mathbf{r} - \mathbf{r}'|} d\mathbf{r}', \quad (3.3)$$

where this effective potential composes of the external potential  $V_{\text{ext}}(\mathbf{r})$ , the exchange- correlation potential  $V_{\text{xc}}(\mathbf{r})$  and the Hartree potential  $V_{\text{Hartree}}(\mathbf{r})$ .

Therefore, the Schrödinger equation for single-particle state called the Kohn-Sham equations is given by (Kohn and Sham, 1965)

$$\left[ -\frac{\hbar^2}{2m} \nabla^2 + V_{\text{eff}}(\mathbf{r}) \right] \psi_i(\mathbf{r}) = \varepsilon_i \psi_i(\mathbf{r}). \quad (3.4)$$

In order to solve Eq. (3.4), initially, a trial electron density,  $\rho(\mathbf{r})$  to find the single-particle wave function, and  $\psi_i(\mathbf{r})$  is defined. Then, the Kohn-Sham equations are calculated by using the single-particle wave function from the initial step. If the two-electron densities in two steps are the same, and then the ground state electron density is reached. If the two electron densities are different, then the process is repeated again. This iterative method can lead to a solution of the Kohn-Sham equations being self-consistent.

### 3.1.3 The local density approximation (LDA)

In general the exchange-correlation energy cannot be exactly derived. Thus, it is necessary to create some approximations to solve the whole problem of many-body interactions. The simplest and most frequently used approximation is the so-called local density approximation (LDA). In this approximation, the exchange-correlation energy has a form similar to that for a homogeneous electron gas (Ceperley and Alder, 1980). But the density at any point in space is replaced by the local density of the actual system.

So, the exchange-correlation energy on the local density approximation can be expressed as (Kohn and Sham, 1965)

$$E_{xc}^{LDA}[\rho(\mathbf{r})] = \int \rho(\mathbf{r}) \varepsilon_{xc}[\rho(\mathbf{r})] d\mathbf{r}^3, \quad (3.5)$$

where  $\varepsilon_{xc}$  is the exchange-correlation energy density in which related to the exchange-correlation potential  $V_{xc}(\mathbf{r})$  by:  $V_{xc} = \delta E_{xc} / \delta \rho = \varepsilon_{xc} + \rho \partial \varepsilon_{xc} / \partial \rho$ . In the special case of the uniform electron gas, the exchange-correlation energy can be written in a term of Slater determinant of single-particle orbitals (Slater, 1974) as (Parr and Yang, 1989)

$$\varepsilon_{xc}[\rho(\mathbf{r})] = -\frac{3}{4} \left( \frac{3}{\pi} \rho(\mathbf{r}) \right)^{1/3}. \quad (3.6)$$

Normally, the functional form for the correlation energy density,  $\varepsilon_{xc}$ , is unknown and has been derived in numerical quantum Monte Carlo calculations which yield essentially exact results (Ceperley and Alder, 1980). The LDA is more accurate for perfect metal but less accurate for systems with varying electron density.

### 3.1.4 Generalized gradient approximation (GGA)

Although the LDA gives surprisingly good results in a wide range of bulk and surface problems, the LDA results always show the overestimated total energy larger than that in experiment. Therefore, the generalized gradient approximation (GGA) has been proposed. In the GGA, a functional is based on the local electron densities and their gradients at considered point (Perdew, Burke, and Ernzerhof, 1996), can be expressed as

$$E_{xc}^{GGA}[\rho(\mathbf{r})] = \int \rho(\mathbf{r}) \varepsilon_{xc}(\rho(\mathbf{r}), |\nabla \rho(\mathbf{r})|) d^3\mathbf{r}. \quad (3.7)$$

This approximation is significantly improved over the LDA results. DFT calculations in the GGA lead to sufficient enough results in the chemical accuracy for many chemical reactions.

### 3.2 Plane waves

Plane waves are the most common approach used to expand the single-particle states of the Kohn and Sham equations into a set of basis functions. In a periodic crystals structure, the Bloch's theorem states that the electron wave function can be written as the product of a cell-periodic part and a plane wave part (Ashcroft and Mermin, 1976),

$$\psi_i(\mathbf{r}) = e^{i\mathbf{k}\cdot\mathbf{r}} u_i(\mathbf{r}). \quad (3.8)$$

The cell-periodic part of the wave function can be expanded in terms of a special set of plane waves as

$$u_i(\mathbf{r}) = \sum_{\mathbf{G}} c_{i,\mathbf{G}} e^{i\mathbf{G}\cdot\mathbf{r}}, \quad (3.9)$$

where  $\mathbf{G}$  is the reciprocal lattice vector of the crystal. By using the definition of the reciprocal lattice vector, the reciprocal lattice vectors  $\mathbf{G}$  are defined by  $\mathbf{G}\cdot\mathbf{s} = 2\pi m$  for all  $s$ . Here,  $s$  is a lattice vector of the crystal and  $m$  is an integer.

Combining Eqs. (3.8) and (3.9), one gives the electronic wave function as a sum of plane waves,

$$\psi_i(\mathbf{r}) = \sum_{\mathbf{G}} c_{i,\mathbf{k}+\mathbf{G}} e^{i(\mathbf{k}+\mathbf{G})\cdot\mathbf{r}}. \quad (3.10)$$

The solution of this expression has a simple explanation as the solution of the Schrödinger equation, it can be written as

$$E = \frac{\hbar^2}{2m} |\mathbf{k} + \mathbf{G}|^2. \quad (3.11)$$

In practice, the solutions with lower kinetic energies are more physically important than solutions with very high kinetic energies. So, the solution is included only in the infinite sum with kinetic energies less than some values, so-called cut off energy ( $E_{\text{cut}}$ ) (Martin, 2004). Then, Eq. (3.10) is reduced to

$$\psi_i(\mathbf{r}) = \sum_{|\mathbf{k} + \mathbf{G}| < G_{\text{cut}}} c_{i, \mathbf{k} + \mathbf{G}} e^{i(\mathbf{k} + \mathbf{G} \cdot \mathbf{r})}. \quad (3.12)$$

Although plane waves are usually used as a basis set to expand the electronic wave functions in periodic systems, plane waves are not efficient to describe wave functions of electrons in core-region.

### 3.3 Pseudopotentials

#### 3.3.1 The concept of pseudopotentials

In principle, the electron potential in matter can be separated into two regions. The first part is the core-region where the electrons are strongly localized in the closed inner atomic shells that defined by the cut-off radius  $r_c$ . The electron potential in this region is strongly attractive. The second part is the interatomic region where the electrons exist outside the core. In this region the electron potential varies very slowly. As a result, a plane wave method is generally not suitable for describing the properties of core electrons. This problem can be overcome by using, so-called pseudopotential method (Phillips, 1958; Phillips and Kleinman, 1959; Heine, 1970). Conceptually, the pseudopotential is replaced by the strong core potential  $V_c(\mathbf{r})$  with a weak pseudopotential that behaves on a set of pseudo-wave functions rather than the

true valence wave functions (Figure 3.1). The pseudopotential is developed based on an all-electron calculation for the isolated atom. Thus, a pseudo-wave function can be written as (Phillips and Kleinman, 1959; Cohen and Chelikowsky, 1988)

$$|\psi_{\text{PS}}\rangle = |\psi_v\rangle - \sum_i |\psi_{c_i}\rangle \langle \psi_{c_i} | \psi_{\text{PS}} \rangle. \quad (3.13)$$

This approximation is the most important approach to reducing the computational effort.

The results of pseudo-wave function  $\psi_{\text{PS}}(\mathbf{r})$  are very smooth for many elements.

### 3.3.2 Norm-conserving pseudopotentials

As the exchange-correlation energy is a function of the electron densities in total-energy calculations. In order to obtain the exchange-correlation energy accurately, the all-electron wave function is replaced by a soft nodeless pseudo-wave function inside the core radius  $r_c$ , and the pseudo-wave functions and the all-electron wave functions outside the core radius  $r_c$  should be identical. Norm-conserving pseudopotentials is described as the scattering properties of an ion in a variety of atomic environments inside the core radius  $r_c$  (Hamann, Schlüter, and Chiang, 1979; Bachelet, Hamann, and Schlüter, 1982). The most general form for a norm-conserving pseudopotential is given by

$$V_{\text{PS}}(\mathbf{r}) = \sum_{lm} |Y_{lm}\rangle V_l(\mathbf{r}) \langle Y_{lm}|. \quad (3.14)$$

where  $|Y_{lm}\rangle$  are the spherical harmonics and  $V_l$  is the pseudopotential for angular momentum  $l$ . Actually, the pseudopotential wave function and eigenvalue are different for different angular momenta  $l$ , the pseudopotentials in this form are often called semi-local. The norm-conserving pseudopotentials are required to reproduce full-potential wave functions accurately in the valence regions.

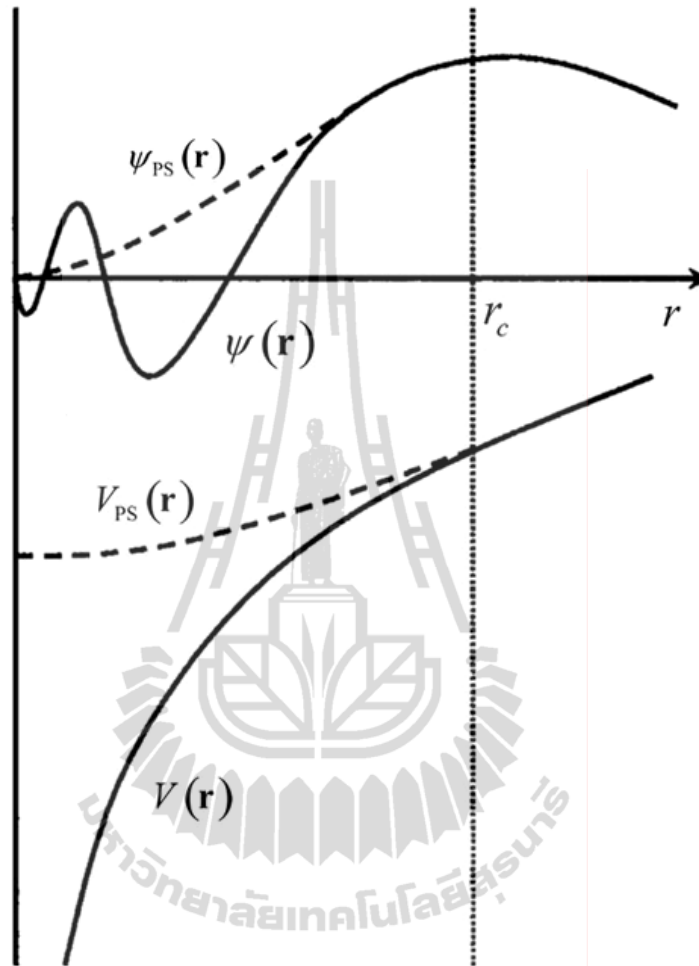


**Figure 3.1** A schematic illustration concept of the pseudopotential (dash lines) and all-electron potential (solid lines) and their corresponding wave functions. The vertical line is indicated the core radius  $r_c$  (Singh and Nordström, 1994).

### 3.3.3 Ultrasoft pseudopotentials (USPP)

For the first-row elements, transition metals and rare-earth elements, a large of plane wave basis set of pseudopotentials is required in the core region and the pseudo-wave functions should be as soft as possible, allowing a low kinetic energy cut-off to be used. To resolve this problem, the ultrasoft pseudopotentials (USPPs) that proposed by Vanderbilt (1990) have been developed. This method can extremely reduce the plane wave cut-off needed in calculations, since it is required quite large value of the core radius  $r_c$ . In the Vanderbilt approach, the basis of norm-conservation is released to obtain smoother pseudo-wave functions in the core region and the charge density difference between the all-electron and pseudo-wave function is calculated from a small number of localized augmentation charges. It becomes possible to choose the core radius of pseudopotential around half of the nearest-neighbor distance. The augmentation charges are required only in a small cut-off radius which is used to recover the moments and the charge distribution of the all-electron wave function accurately (Laasonen et al., 1993). One of disadvantage of this method is the rather difficult construction of the pseudopotentials.

### 3.3.4 Projector augmented waves (PAW)

The PAW method (Blöchl, 1994; Holzwarth et al., 1997; Kresse and Joubert, 1999) was developed based on the USPPs method, which works with the full all-electron wave functions. The PAW method was firstly proposed by Blöchl (1994). The PAW method describes the wave function by a superposition of the pseudo-wave functions and the all-electron wave function by using a linear transformation and modified the total energy functional consistent with the transformation to the Kohn-Sham functional. In the PAW, a linear transformation  $\tau$  is given by

$$|\psi_n\rangle = \tau |\tilde{\psi}_n\rangle \quad (3.15)$$

where  $|\psi_n\rangle$  is the all-electron wave function and  $|\tilde{\psi}_n\rangle$  is the pseudo-wave function. The important point is to construct the all-electron wave function from the pseudo-wave function through a linear transformation as

$$|\psi_n\rangle = |\tilde{\psi}_n\rangle + \sum_i (|\phi_i\rangle - |\tilde{\phi}_i\rangle) \langle \tilde{p}_i | \tilde{\psi}_n \rangle. \quad (3.16)$$

Here,  $|\phi_i\rangle$  is the all-electron partial waves obtained for a reference atom,  $|\tilde{\phi}_i\rangle$  is the pseudo-partial waves equivalent to the all-electron partial waves outside a core radius  $r_c^l$  and also match continuously onto  $|\tilde{\phi}_i\rangle$  inside the core radius, and  $|\tilde{p}_i\rangle$  is the projector function for each pseudo-partial wave satisfied the relation  $\langle \tilde{p}_i | \tilde{\psi}_n \rangle = \delta_{ij}$ . Therefore, a linear transformation can be obtained from Eq. (3.16) as

$$\tau = 1 + \sum_i (|\phi_i\rangle - |\tilde{\phi}_i\rangle) \langle \tilde{p}_i |. \quad (3.17)$$

Considering materials with strong magnetic moments, the PAW method provides more reliable results than that of USPPs.

### 3.4 The Vienna *Ab initio* Simulation Package (VASP)

In the present work, all of calculations are performed with the Vienna *Ab initio* Simulation Package (VASP), which developed by Georg Kresse and co-workers (Kresse and Hafner, 1993; 1994; Kresse and Furthmüller, 1996a, 1996b; Kresse and Joubert, 1999). VASP is described by the interaction between ions and electrons by using pseudopotentials or the projector-augmented wave method and a plane wave basis set. So, the number of plane waves per atoms for transition metals and first row

elements can be reduced. In VASP, forces and the full stress tensor can be calculated and used to relax atoms. VASP is mainly used with an iterative matrix-diagonalization scheme to minimize the total energy. Most of algorithms implemented are based on the conjugate gradient (CG) scheme (Teter, Payne, and Allan, 1989; Bylander, Kleinman, and Lee, 1990), the blocked Davidson scheme (Liu, 1978; Davidson, 1983), or a residual minimization scheme–direct inversion in the iterative subspace (RMM-DIIS) (Pulay, 1980; Wood and Zunger, 1985). The charge density mixing is used within an efficient method of Broyden or Pulay scheme (Pulay, 1980; Johnson, 1988). The forces acting on the ions can be evaluated with the Hellmann-Feynman theorem (Feynman, 1939). The k-point mesh was generated automatically on the basis of the Monkhorst and Pack scheme (1978).

### **3.5 Surface calculations**

#### **3.5.1 Slab models for surfaces**

Since the surface is formed by truncate a bulk crystal, surface atoms have fewer neighbors than bulk atoms. Thus, the ideal model to create the surface would be a slice of the bulk crystal structure in two dimensions and repeated periodically along the surface normal to form a supercell (Figure 3.2). This model is called a slab model. In a supercell, the empty space separating atoms in the slab along the surface normal direction is called the vacuum layer. If the vacuum layer is thick enough so that the electron density of the material spills out into the vacuum and can minimize any interactions between atoms of the next slab.

### 3.5.2 Computational details

In the present studies, the structure of Ni/Cu(001) films was modeled using the VASP code. The Ceperley-Alder functional (1980) together with the Perdew and Wang formulae (1992) of generalized gradient approximation are used to describe the electron ion-interactions. For the correlation part of the exchange correlation functional, the interpolation formula is performed according to the Vosko-Wilk-Nusair parameterization (1980). The residuum minimization method direct inversion in the iterative subspace is used to optimize the structure. The PAW basis of VASP code was used to describe the wave functions and potentials with the plane wave energy cut-off of 270 eV.

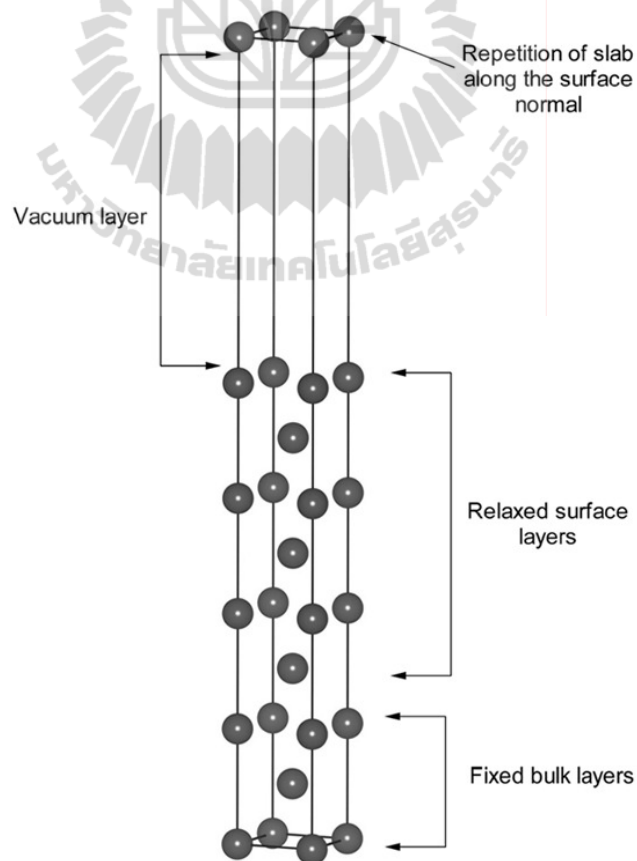


**Figure 3.2** A schematic of basic idea of slab model.

### 3.5.3 Ni/Cu(001) surfaces

The structures of Ni/Cu(001) films were modeled by periodically repeated slabs with five layers of Cu in the (001) orientation and Ni films of 1 to 11 layers placed pseudomorphically on both sides of this slab to maintain the inversion symmetry. The in-plane lattice constant ( $a_0$ ) is fixed at 3.58 Å according to the experimental data (Platow et al., 1999). The Brillouin-zone integrations were performed using grids of (9×9×1) k-points in the surface cell. The slab surface cells were separated by  $3a_0$  of vacuum layer. The examples of supercell used to create Cu(001) and Ni/Cu(001) surfaces are shown in Figure 3.3.

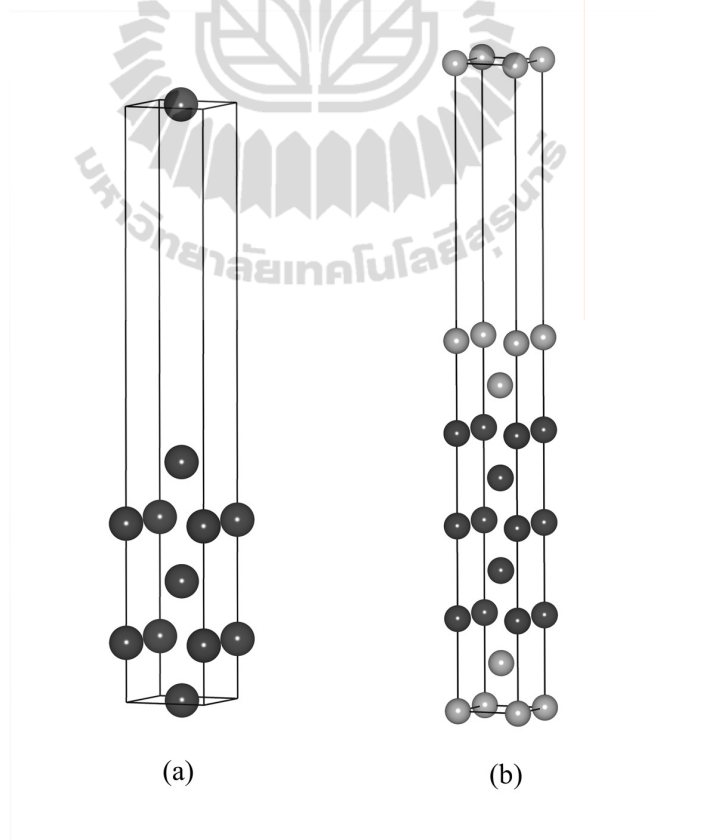


**Figure 3.3** A schematic diagram of a supercell that used to model: (a) 5 ML Cu(001) and (b) 2 ML Ni on each side of 5 ML Cu(001) slab.

## CHAPTER IV

### EXPERIMENTAL TECHNIQUES AND INSTRUMENTS

This chapter consists of a description of the important techniques, the experimental instruments and the sample preparation used in this thesis work. In addition, parameters used in the ARPES are also described.

#### 4.1 Experimental techniques

##### 4.1.1 Auger electron spectroscopy (AES)

Auger electron spectroscopy is an analytical technique to identify the atomic element in materials. It has been extensively used to check impurities in high-purity metals and to determine the chemical composition of the adsorbed atom. The emitted secondary electrons generated in the Auger process are analyzed and their kinetic energies are measured. The Auger process is initiated by creation of a core hole in an inner shell of the atom, excited by an electron beam (Figure 4.1). Then the hole in an inner shell is filled by an electron in the outer shell. A released energy is transferred to excite another electron. The ejected electron is called the Auger electron. Therefore, the energy of the Auger electron depends on the energy levels realized in the atom. A kinetic energy of the Auger electron from the various electron levels can also be written in the form:

$$E_{\text{kin}} = E_K - E_{L_1} - E_{L_{2,3}}. \quad (4.1)$$

The capability of AES as a tool for determining film thickness is based on the relaxation effect of the Auger electrons produced by interior atoms (Figure 4.2). For the simple case of an overlayer of element, A, on a substrate of element, B, one can write an intensity of the Auger electron,  $I_A$ , emitted from an overlayer of thickness  $d$  as (Cumpson and Seah, 1997)

$$I_A = I_A^\infty \left\{ 1 - \exp \left[ - \frac{d}{\lambda_{\text{imfp}}^A(E_A)} \cos \theta \right] \right\}, \quad (4.2)$$

and an intensity for the substrate composed of element B can be written as

$$I_B = I_B^\infty \exp \left[ - \frac{d}{\lambda_{\text{imfp}}^A(E_B)} \cos \theta \right], \quad (4.3)$$

where  $I^\infty$  is the intensity from pure element,  $s$  a sensitivity factor, and  $\lambda_{\text{imfp}}^x$  the inelastic mean free path (IMFP) of electrons, which is depend on a kinetic energy of the Auger electron from the overlayer.  $E_A$  and  $E_B$  are the kinetic energy of electrons from the overlayer and substrate, respectively.

Further, Powell (1985) suggested that the appropriate length scale should be involved into the quantification equation as the attenuation length (AL) instead of IMFP. AL is obtained from overlayer-film experiments based on a model in which the effects of elastic electron scattering are ignored. It was found that, a factor of AL gives more accurate results than that of IMFP. In the case of the energy of the peak from element A closed to element B, we can assume that ALs of signal electrons, which are a function of kinetic energy from overlayer and substrate, are identical (Fulghum et al., 1992), i.e.  $\lambda_{\text{AL}}^A(E_A) = \lambda_{\text{AL}}^A(E_B) = \lambda_{\text{AL}}$ , so that we can obtain thickness as

$$d = \lambda_{AL} \cos \theta \ln \left[ 1 + \frac{(I_A / s_A)}{(I_B / s_B)} \right]. \quad (4.4)$$

Here,  $s_{Ni}$  of 1.0478 and  $s_{Cu}$  of 1.1435 were used in our experiment. One can see that both the overlayer and substrate signals show a linear change with the measurement of the thickness of an overlayer.

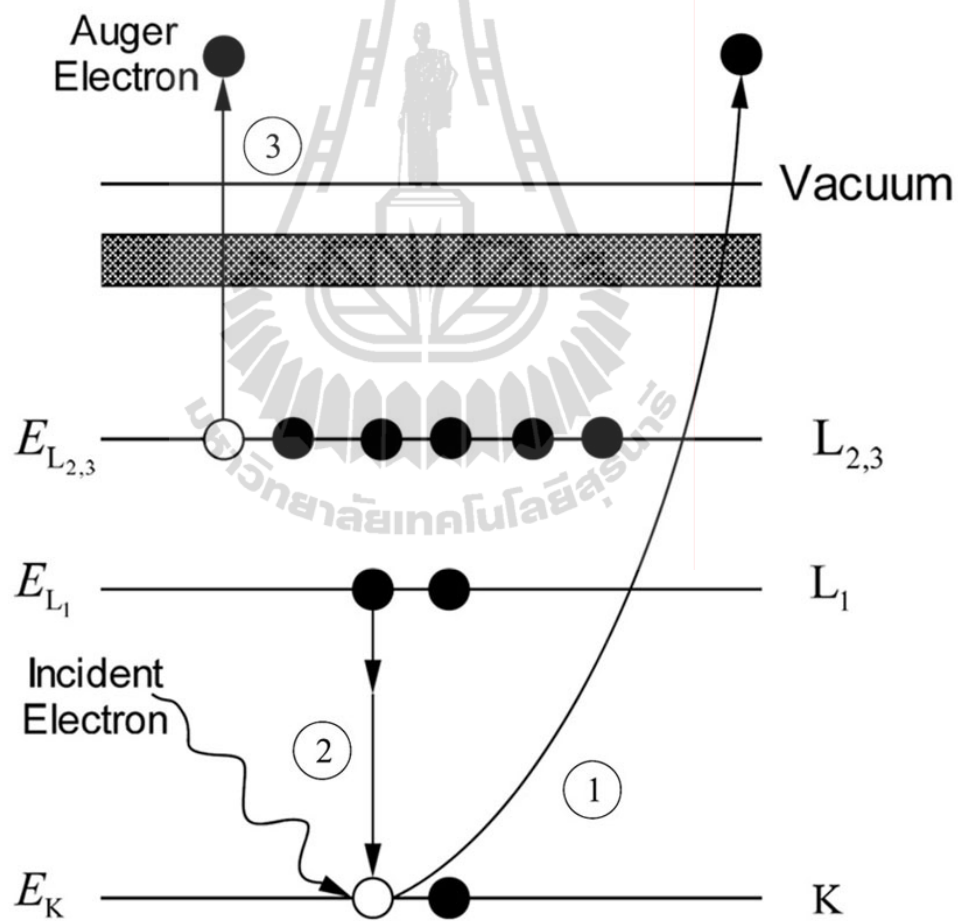


**Figure 4.1** A schematic diagram of the Auger process. A hole is firstly created in the K shell when the atom is ionized by an incident electron. This hole is filled by an electron in the L<sub>1</sub> shell.

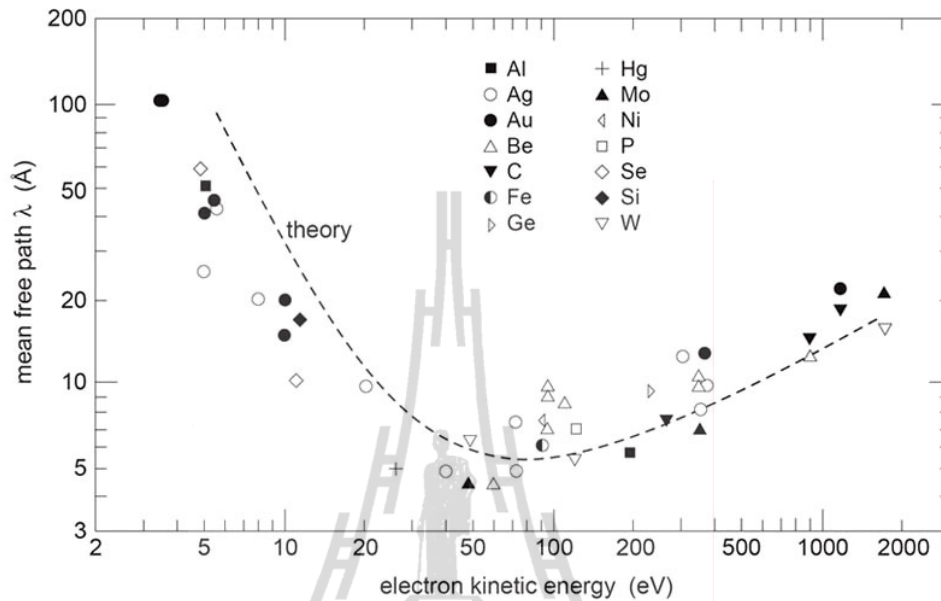


**Figure 4.2** The mean free path of the electron in solid. The dots correspond to the measurement results, and the dashed curve the calculation (Werner, 2004).

#### 4.1.2 Low energy electron diffraction (LEED)

LEED is the main technique used to study the morphology and structure of surface. In the LEED optics, the low-energy electron beam is incident on a surface normal, and the diffracted electrons against the surface are detected on a fluorescent screen by accelerating electrons through a mesh in a high electric field (Figure 4.3). The electrons incident on perpendicular to surface are elastically scattered within a depth of only a few atomic layers, which are comparable to the spacing between atoms of the crystal surface. Therefore, the diffracted pattern in a LEED experiments reflects the surface reciprocal lattice rods projected on the Ewald sphere (Oura et al., 2003).

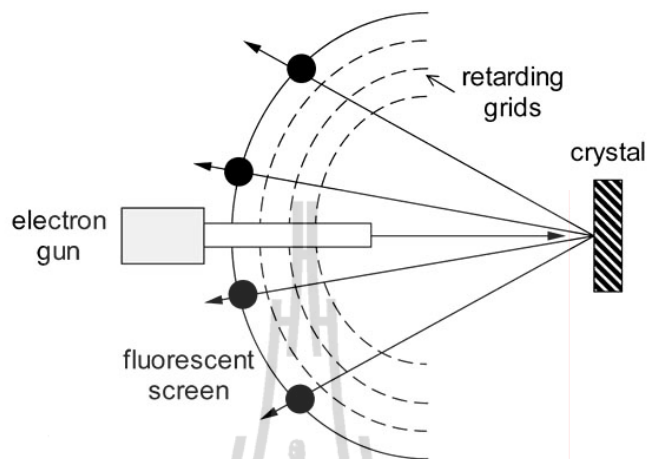


**Figure 4.3** A schematic diagram of LEED optics.

#### 4.1.3 Reflection high energy electron diffraction (RHEED)

RHEED is an important *in situ* analysis technique used to monitor a film quality during the film growth. RHEED patterns give information on the morphology of the growing film surface (Figure 4.4). The oscillations in the intensity of the diffracted beams in RHEED pattern are possible to monitor the atomic layer-by-layer growth of epitaxial films (Ichimiya and Cohen, 2004). In the RHEED experiment, the high-energy electron beam (5-20 keV) is incident on a surface in a grazing angle, and the diffracted electrons on the surface are detected on a fluorescent screen (Figure 4.5). Owing to the electron beam on the sample surface at grazing incidence, the electrons penetrate a limited depth and probe the surface lattice order. The diffracted patterns correspond to the projection of the surface reciprocal rods on a part of the Ewald sphere. The grazing electron beam optics is not interfered with the other instruments in the surface normal direction, so that RHEED patterns can be monitored during a deposition process. Figure 4.6 illustrates the typical streaky RHEED patterns of an ultrathin film of Ni grown on Cu(001).

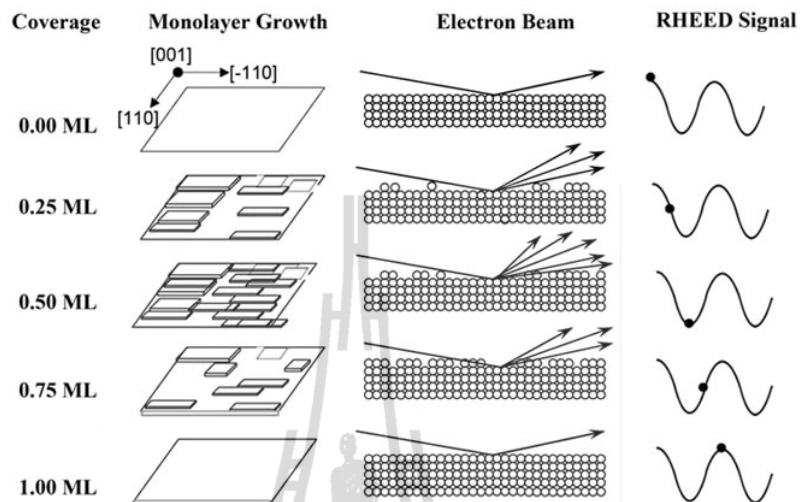


**Figure 4.4** Schematic pictures showing the relationship between the intensity oscillations of the RHEED pattern and the film morphology for layer-by-layer growth (Ploog, 1988).

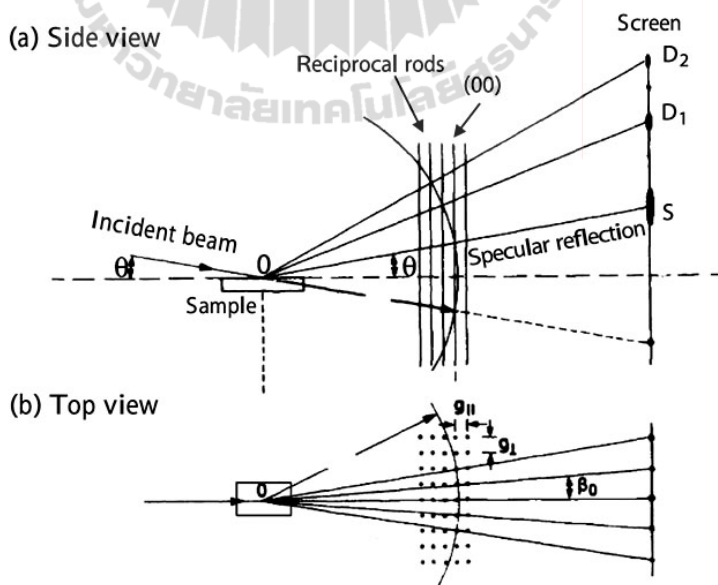


**Figure 4.5** A schematic picture of diffraction geometry of RHEED. Intensity maxima on the screen correspond to projected intersections of the Ewald's sphere with the reciprocal rods (Wuttig and Liu, 2004).



**Figure 4.6** RHEED patterns after 5 ML Ni was grown on Cu(001) at room temperature.

#### 4.1.4 Molecular beam epitaxy (MBE)

MBE technique has been developed to synthesize new functional crystals in combination with well-known materials on a well defined substrate (Cho and Arthur, 1975). Because the electronic and magnetic properties of ultra-thin films strongly depend on their thicknesses, MBE technique has also been used to grow films in various thicknesses for surface, interface, and multilayer studies.

MBE is a kind of vacuum evaporation techniques, so that MBE requires a well-defined UHV condition to obtain the high quality of target evaporation and deposition on a substrate. A growth rate is easily controlled by adjusting a power to the heater, and monitored by *in-situ* flux monitors and/or RHEED intensity oscillations. Deposition duration is controlled by opening and closing a shutter located in between the evaporator and the substrate. The present MBE experimental setup is illustrated in Figure 4.7.

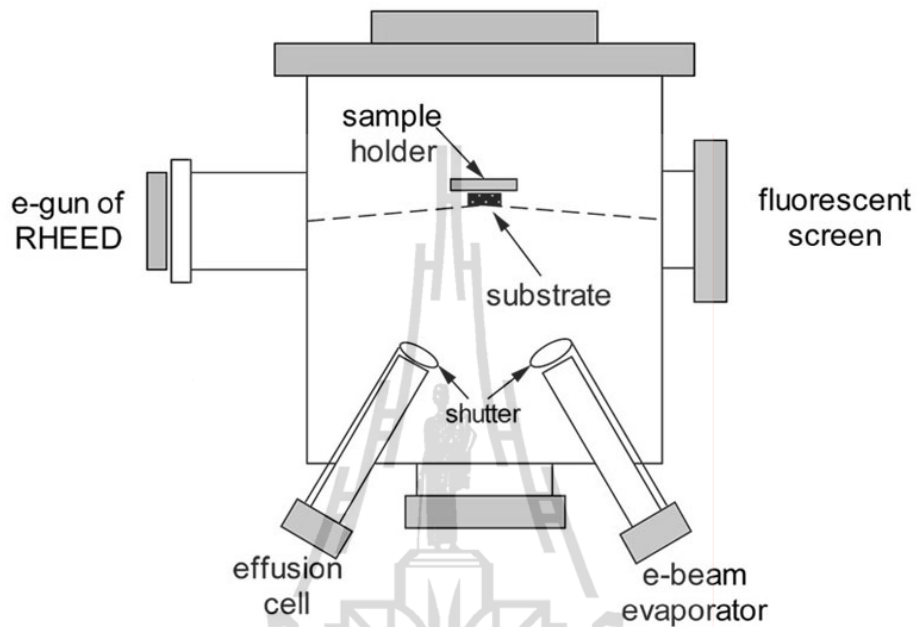


**Figure 4.7** A schematic of the MBE system at the BL4 beamline.

#### 4.1.5 Surface magneto-optical Kerr effect (SMOKE)

The magnetization of magnetic materials induces an optical anisotropy leading to various optical responses depending on a light polarization incident on materials. In particular, among these various magneto-optic effects, SMOKE has been getting more attentions because the surface magnetism plays an important role in the development of high-density recording media. The experimental setup of SMOKE is simple and developed without any advanced instrument. The magneto-optic Kerr effect (MOKE) is attributed from the interaction between the electrical field of the light and the electron spin within a magnetic medium, originating from the spin-orbit interaction. As it is well known, the optical properties of a medium are determined by a dielectric tensor corresponding to the motion of the electron in the medium. The electric field of

the light introduces the motion of the electrons in the medium where a beam of light propagates through a medium. Then, MOKE shows the different response of the electrons to left- and right circularly polarized lights.

Consider the following antisymmetric dielectric constant tensor (Qiu and Bader, 2000):

$$\tilde{\epsilon} = \epsilon \begin{pmatrix} 1 & iQ_z & -iQ_y \\ -iQ_z & 1 & iQ_x \\ iQ_y & -iQ_x & 1 \end{pmatrix}, \quad (4.5)$$

where  $\mathbf{Q} = (Q_x, Q_y, Q_z) = \mathbf{Q}(\alpha, \beta, \gamma)$  is called the Voigt vector (Voigt, 1915), and  $\alpha, \beta, \gamma$  are the direction cosines of the magnetization vector  $\mathbf{M}$ . These modes are left- and right-circularly polarized lights. The refraction index of left- and right-circularly polarized lights are  $n_L = n\left(1 - \frac{1}{2}\mathbf{Q} \cdot \hat{\mathbf{k}}\right)$  and  $n_R = n\left(1 + \frac{1}{2}\mathbf{Q} \cdot \hat{\mathbf{k}}\right)$ , respectively. Two parameters are used to describe the Kerr effect i.e., the Kerr rotation  $\alpha_K$  and the ellipticity  $\epsilon_K$ . The Kerr rotation is due to the different phase shifts of the two circularly polarized modes, while the ellipticity is caused by the different absorption rates of the medium for the two circularly polarized modes.

In SMOKE, a linearly polarized light is incident on a magnetic sample surface, and then a reflected light polarization is rotated as a result of the optical anisotropy, namely, the Kerr effect (Figure 4.8). The Kerr rotation angle and polarized ellipticity depend on the magnetization and the incident angle of the light on the material surface, respectively. The linearly polarized light can be decomposed into left-handed and right-handed circularly polarized light with equal amplitudes.

In the case of normal incidence of linearly polarized light, these two modes have different complex reflection coefficients as

$$r^j = \frac{E_r^j}{E_i^j} = -\frac{n^j - 1}{n^j + 1} = |r^j| e^{i\phi_j}, \quad j \in (\text{L}, \text{R}), \quad (4.6)$$

where  $E_i$  and  $E_r$  are the light intensity of the incoming and reflected wave fields and  $n$  is the refractive index. Therefore, the recombination of two circularly polarized modes from the magnetized medium after reflection relates to the Kerr rotation ( $\alpha_K$ ) and the Kerr ellipticity ( $\varepsilon_K$ ). The Kerr ellipticity is given by the normalized difference between the amplitudes,

$$\varepsilon_K = -\frac{|r^L| - |r^R|}{|r^L| + |r^R|}, \quad (4.7)$$

and the Kerr rotation is given by

$$\alpha_K = -\frac{1}{2}(\phi^L - \phi^R). \quad (4.8)$$

There are two different SMOKE geometries depending on the orientation of the magnetization vector  $\mathbf{M}$  relative to the incidence plane, i.e. the longitudinal and polar Kerr geometries (Figure 4.9). In the longitudinal geometry, the magnetization vector is parallel to the surface plane and also the plane of incidence. In the polar geometry, the magnetization vector is perpendicular to the surface plane and parallel to the plane of incidence. This geometry gives the highest signal when the polarized light beam hits the surface near normal incidence. The magnetic anisotropy energy corresponds to the area difference between hysteresis loops obtained in the longitudinal and polar Kerr effects.

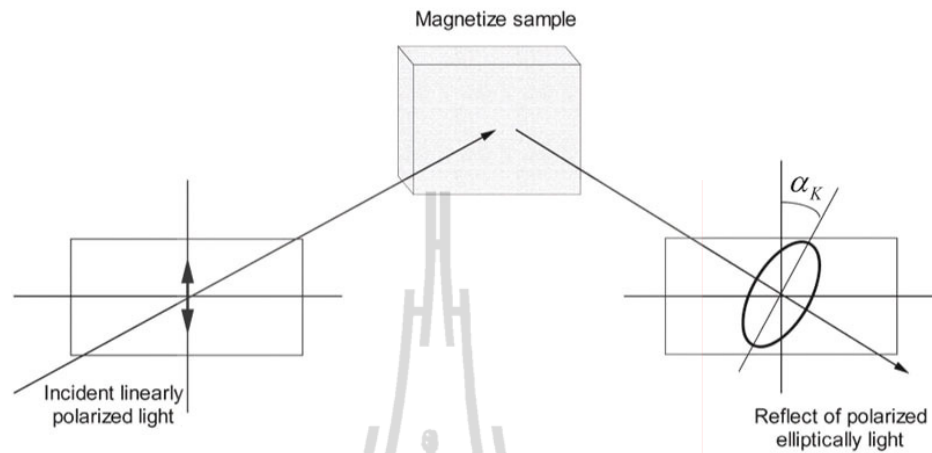


**Figure 4.8** A schematic diagram of magneto-optic Kerr effect. Upon reflection of linearly polarized light from a magnetized sample, an elliptical polarization and rotation of the polarized plane occur.

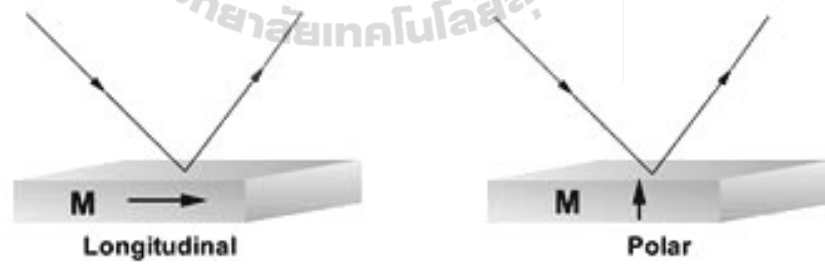


**Figure 4.9** Orientation of the magnetization and the incidence plane for the two main Kerr geometries.

## 4.2 Experimental instruments

### 4.2.1 Vacuum chamber

The experimental station of the beamline 4 (BL4) at the Siam Photon Laboratory in the Synchrotron Light Research Institute (SLRI) has been providing the synchrotron radiation from a bending magnet source with a photon energy between 40 and 240 eV. This enables us to map a whole energy band dispersion in both surface and bulk Brillouin zones (BZs) using ARPES techniques. A linearly polarized light from the synchrotron radiation allows us to identify the initial state symmetry. This is a great advantage for this research to reveal a relationship between the energy band and its orbital symmetry responsible for the magnetic anisotropy owing to a spin-orbit interaction.

The end-station of BL4 (Figure 4.10) is equipped with sample manipulators, electron energy analyzers, LEED optics, electron and ion guns, the MBE system with RHEED optics, and the SMOKE system. All instruments are operating in ultra-high-vacuum (UHV) conditions and samples are transferred between systems without breaking UHV.

The photoemission chamber consists of the preparation chamber and the analysis chamber as illustrated in Figure 4.11. The preparation chamber equipped with the ion gun allows us to treat a surface by an ion sputtering technique. The surface characterizations have been performed in the analysis chamber. The analysis chamber is equipped with the electron gun, LEED optics and two electron energy analyzers; ARUPS 10 and Alpha 110. The manipulator is mounted on the preparation chamber with the sample holder system. The sample holder has heating and cooling units with temperature monitoring sensors.

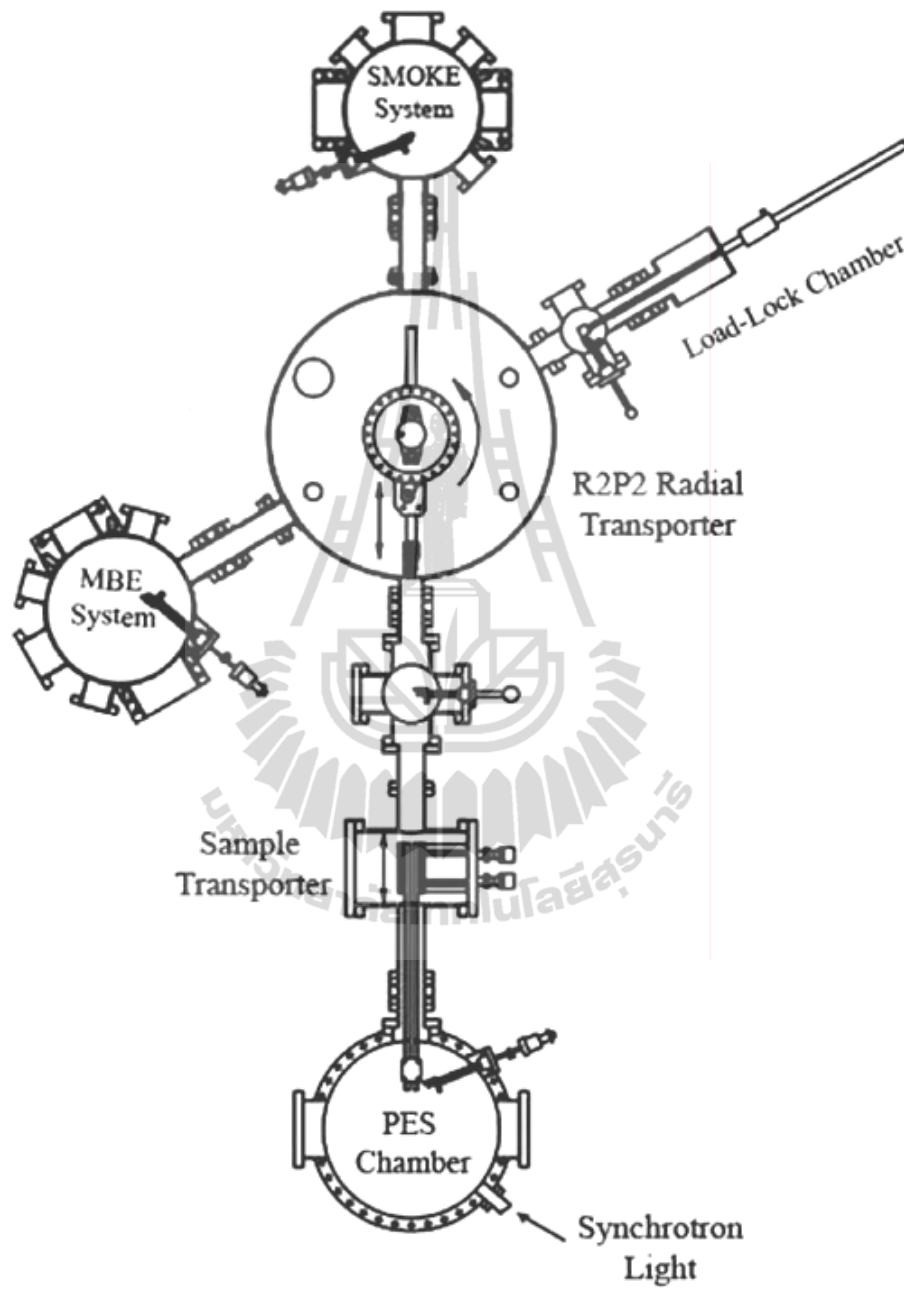


**Figure 4.10** A schematic diagram of the experimental station for the BL4 at SLRI.

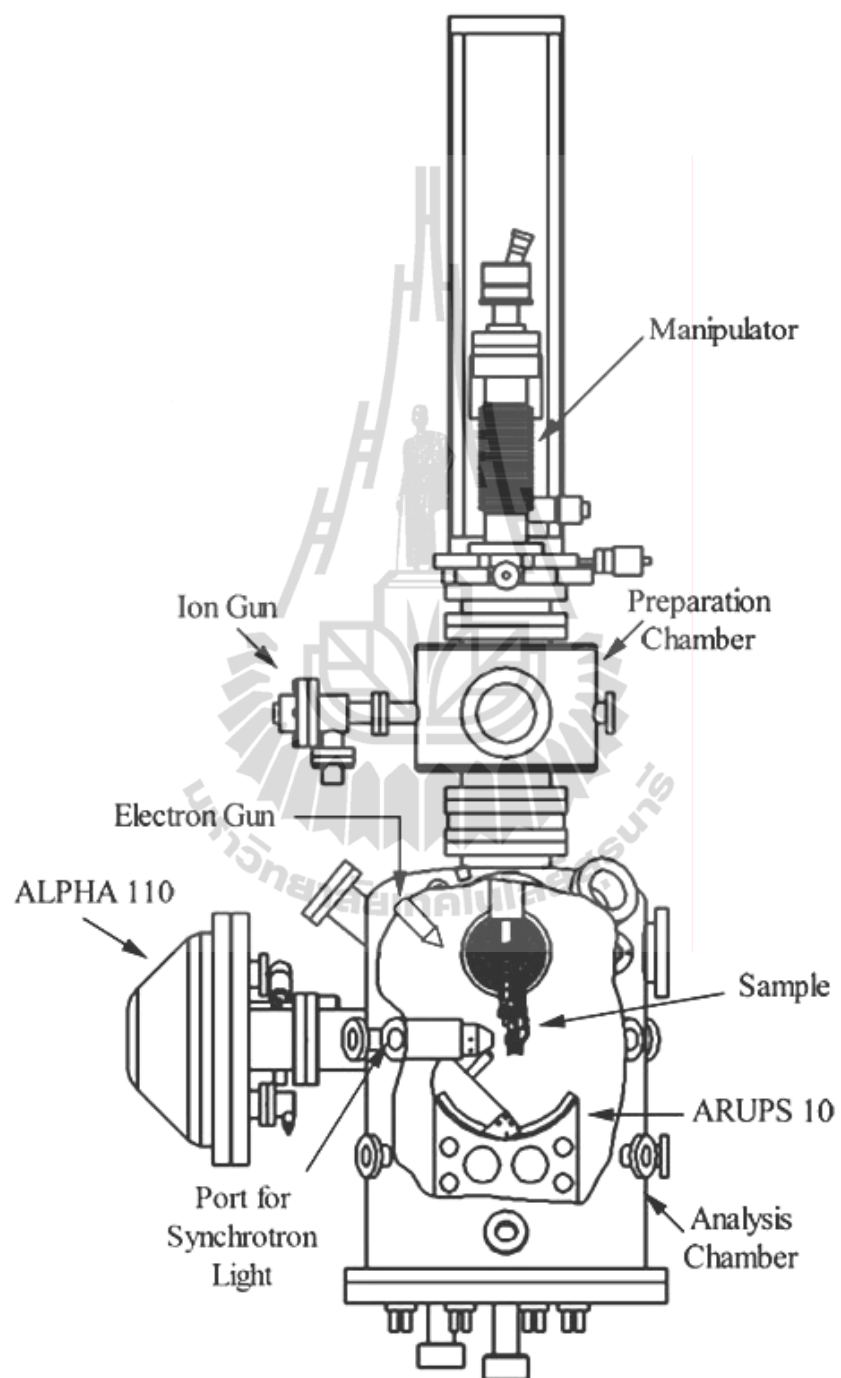


**Figure 4.11** A schematic diagram of the photoemission system at BL4.

#### 4.2.2 Electron energy analyzer

In this work, two types of energy analyzers were used, one is the Alpha 110 and the other ARUPS 10. The Alpha 110 is a 180° hemispherical electron energy analyzer with mean radius of 110 mm (Figure 4.12). It is installed with 7 channel-detectors and the three lens elements corresponding to small area, large area or angle resolved experiments. It has two modes of measurement; one is CAE (Constant Analyzer Energy), in which the analyzer pass energy and the energy resolution is constant, and the other CRR (Constant Retard Ratio), in which the analyzer pass energy and the energy resolution varies as a constant ratio of the kinetic energy. For measurements of ARPES spectra, we used ARUPS 10, which is a hemispherical analyzer with a mean radius of 75 mm mounted on goniometer. The goniometer rotates the analyzer along two axes: 360° polar and 100° azimuthal rotation. The analyzer has the multi-channel detector including the lens with variable acceptance angles from  $\pm 0.2$  to  $\pm 2.0^\circ$ .

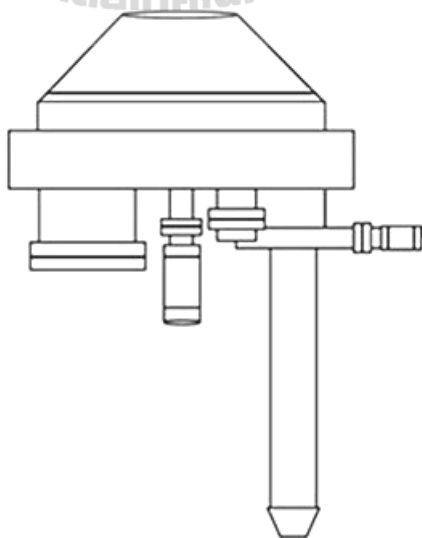


**Figure 4.12** A schematic diagram of Alpha 110 (Thermo Electron Corporation, 2004).

### 4.3 Sample preparations

High-purity copper single crystals (99.999%) available in the commercial market were purchased to prepare a substrate for Ni film growths. The single crystal rod aligned to the [001] direction was sliced to several disk-shaped samples by a cutting machine with the silicon carbide cut-off wheel. The Cu(001) disks were further mechanically grinded on a silicon carbide paper up to 4000 grade. The polishing surfaces were finalized with a diamond suspension down to 0.8  $\mu\text{m}$  diameter. The samples were chemically cleaned with acetone and ethyl-alcohol solutions in the ultrasonic bath before loading to a UHV chamber at a base pressure of  $2 \times 10^{-10}$  mbar. Several cycles of 1 keV Ar ion sputtering and subsequent annealing at 600°C for 10 min remove surface impurities such as sulfur, carbon, and oxygen detected by the AES measurements. Finally, a surface long-range lattice order was inspected in terms of a good sharpness and clear contrast to the background in the LEED patterns.

According to the several reports previously published, epitaxial nickel films can be grown on the Cu(001) surface at room temperature. The mini electron-beam evaporator was used to deposit Ni films on the Cu(001) surface. High-purity nickel rod (99.99%) was purchased from the commercial company with a diameter of 2 mm as a target. The Ni rod was cut in a length of 24 mm loading to the evaporator. The operating pressure of the evaporation was below  $7 \times 10^{-9}$  mbar. The crystal lattice orders of each film have been checked by LEED (Figure 4.13). The LEED pattern shows a sharp  $p(1 \times 1)$  and low background intensity, resulting from a good structural order in the topmost surface layer. All of Ni films were deposited at room temperature without subsequent annealing to avoid interfacial mixing. The growth of the films was

monitored by RHEED, performing with an electron energy of 15 keV. An average deposition rate of Ni films of about 0.6-1.6 ML/min obtained from RHEED oscillations (Figure 4.14). Figure 4.15 shows the AES spectra for the particular Ni film thickness.

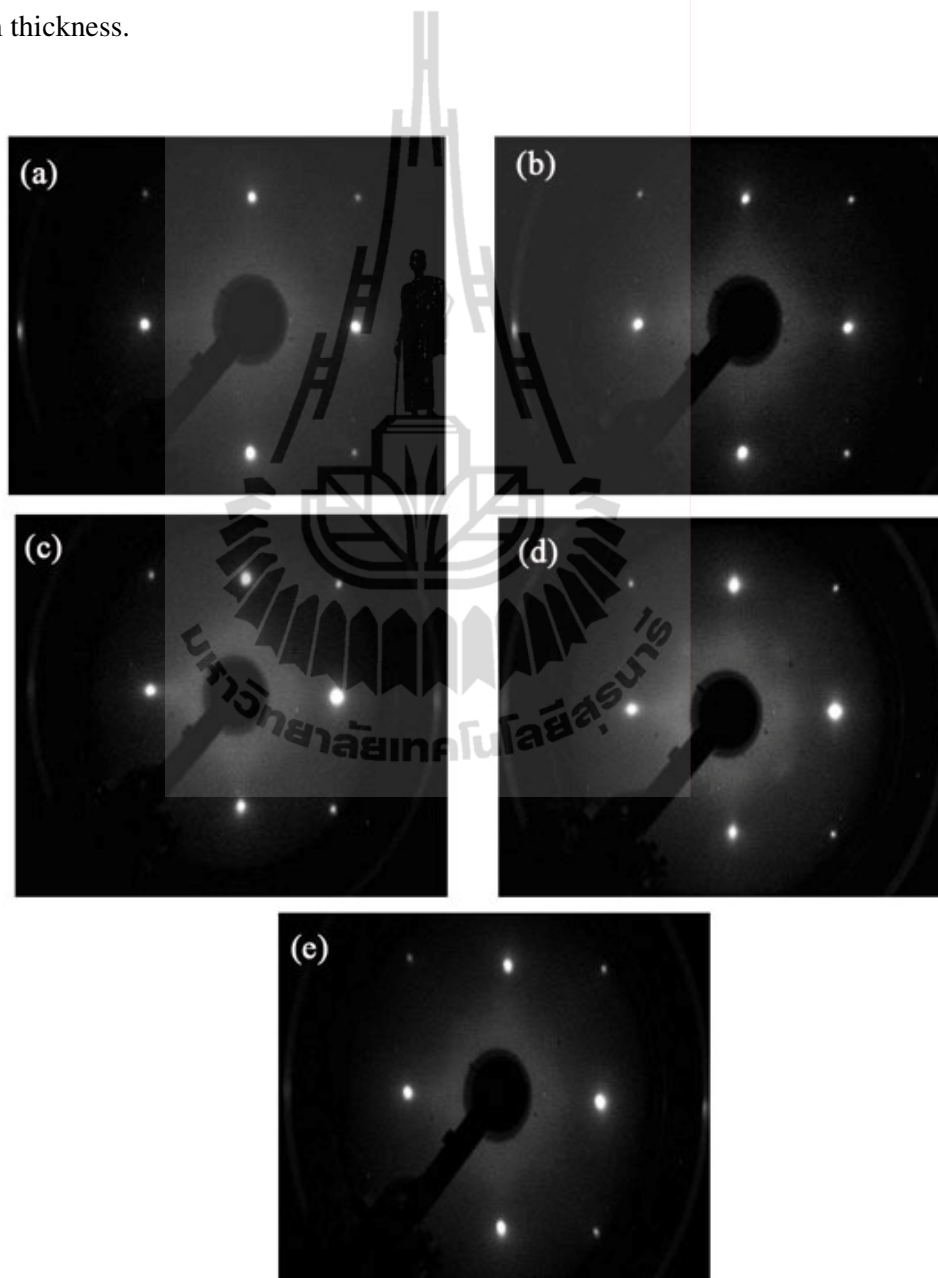


**Figure 4.13** LEED patterns of (a) 1.7 ML, (b) 3.6 ML, (c) 5.5 ML, (d) 7 ML, and (e) 10 ML Ni/Cu(001) at an electron energy of 76 eV.

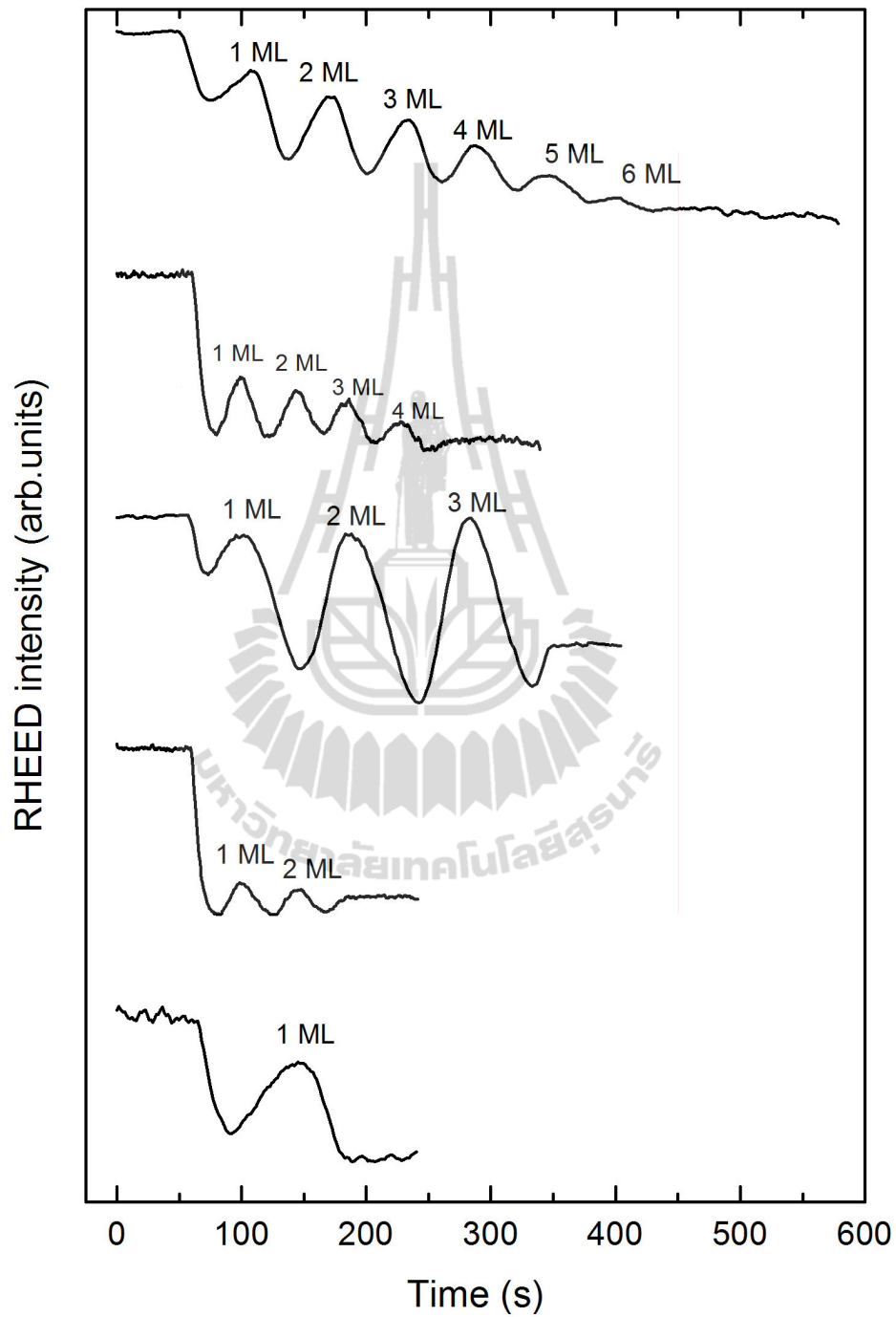


**Figure 4.14** Thickness dependence of the oscillations in RHEED patterns in MBE growth of Ni on Cu(001) at room temperature.

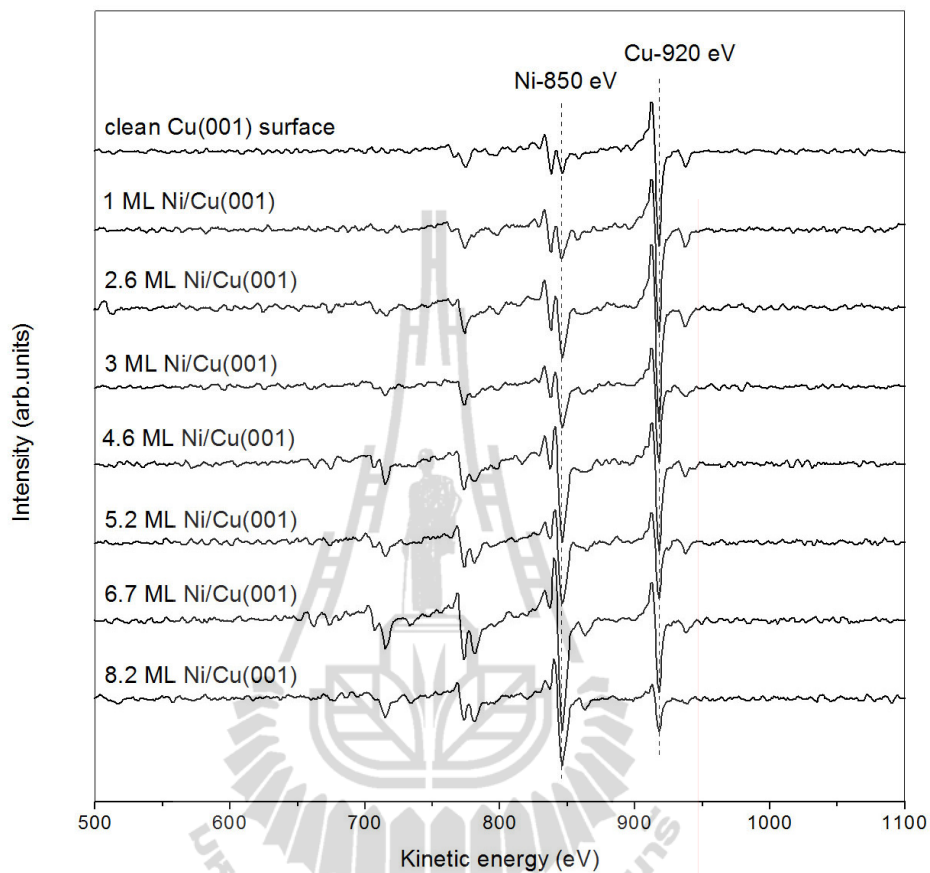


**Figure 4.15** AES spectra on various Ni films thicknesses including comparing to clean Cu(001) surface.

#### 4.4 Thickness calibration

Since the lattice structure and magnetic properties of the studied films are sensitively dependent on the film thickness, it is of importance to control and measure the film thickness precisely. In this work the film thickness is mainly determined by RHEED oscillations at an electron energy of 15 keV. Since both Ni and Cu materials have the same fcc crystal structure with only 2.5% lattice mismatch, the growth of Ni on Cu(001) surface displays a good epitaxial film. The oscillatory behavior during

deposition shows the layer-by-layer growth. The RHEED oscillations have been observed as a good layer-by-layer mode up to 7 ML (Figure 4.14).

The interpretation of the RHEED results has been combined with the AES measurements. The thickness calibration for the Ni overlayer was performed by measuring the AES signal of Ni LMM (850 eV) and Cu LMM (920 eV) for all films at the end of growth using an electron energy of 5 keV. The correlation between the RHEED oscillation and AES signal ratio can be obtained by taking a linear fit according to Eq. (4.4). In this calculation, AL of  $\lambda_{AL} = 7.4$  ML was used. Figure 4.16 shows the correlation of Ni film thickness obtained from the RHEED oscillation and AES signal. The thickness calibration curve shows less accurate at the range of overlayer thicknesses for  $d < 1$  ML and  $d > 12$  ML corresponding to the interval AES signal ratio limits suggested from Compson and Seah (1997).

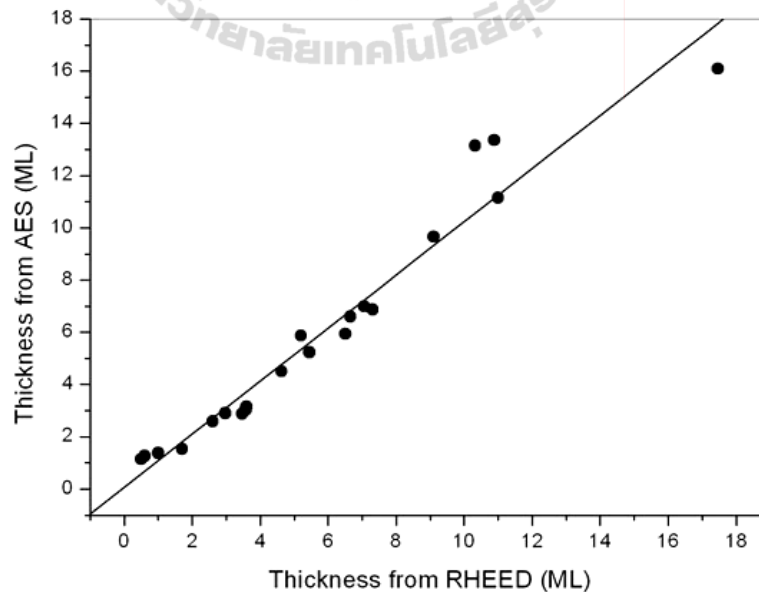


**Figure 4.16** Calibration of Ni films thickness obtained from the RHEED oscillation and AES measurements.

## 4.5 Angle-resolved photoemission measurements

ARPES experiments were performed by using the synchrotron radiation at the BL4 of SPL of SLRI (Nakajima et al., 2007). The ARPES apparatus consists of an ion gun, an electron gun for AES, a temperature-controlled sample holder, and an electron-energy analyzer (Thermo VG Scientific; ARUPS10). Pressure in the analysis chamber was below  $2 \times 10^{-10}$  mbar during the ARPES measurements. The synchrotron light was incident at angle of  $20^\circ$  and  $45^\circ$ . The angle of  $20^\circ$  corresponds to the *s*-polarization dominant incident light, and the angle of  $45^\circ$  includes composition of *s* and *p* polarizations equivalently. In the spectra measured at  $45^\circ$  incidences, the  $\Delta_1$  symmetry in the spectra is more distinguishable than that measured at an incident angle of  $20^\circ$ . The overall energy resolution of the measured spectra was 170 meV at a photon energy of 45 eV, which was confirmed on the Fermi edge ( $E_F$ ) of a gold sample at room temperature. The acceptance angle of ARUPS10 was set to  $\pm 1^\circ$ . The angle-scanned data for different thicknesses were taken with a photon energy of 44 eV, which is close to the  $\Gamma$  point of bulk Ni along [100] for binding energies near  $E_F$ . Normal emission spectra excited by a photon energies from 40 to 110 eV in 4-eV steps and in 2-eV steps to 110 eV, covering the  $\Gamma$  to X points in the bulk BZ. For a surface energy band mapping, the in-plane surface orientation was adjusted in the high-symmetry plane ( $\bar{\Gamma}$ - $\bar{X}$ ) where the linearly polarized light was incident and the ARPES analyzer was scanned (Figure 4.17).

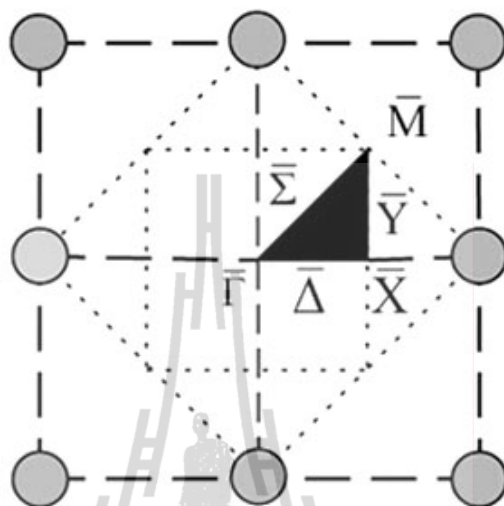


**Figure 4.17** A schematic illustration of LEED pattern on Ni/Cu(001) surfaces. First surface BZs are also shown with corresponding irreducible representations in the inset of LEED pattern.

#### 4.6 Surface magneto-optic Kerr effect measurements

The magnetic properties in this study were measured *in-situ* using SMOKE with the experimental setup shown in Figure 4.18. A light source was performed with a linearly polarized He-Ne laser ( $\lambda = 632.8$  nm). A polarized light reflected from the sample surface is detected by a silicon photo detector, with an extinction ratio of  $10^{-6}$ . The external magnetic field was generated from a c-shape electromagnet, which allows to be applied either parallel (longitudinal) or perpendicular (polar) to the film plane. A c-shape electromagnet can be produced in the magnetic field up to about 1600 Oe. In this study, the substrate can be cooled down to about 123 K, monitored by a type-K thermocouple.

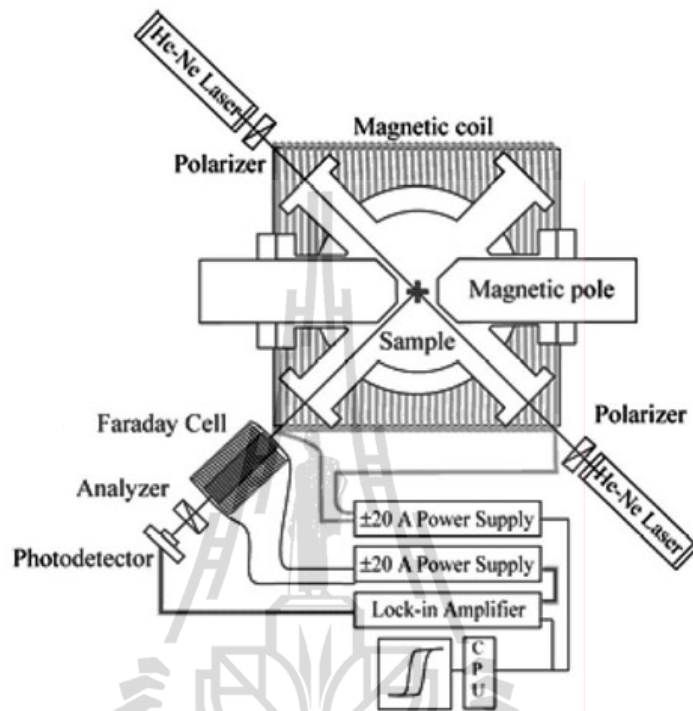


**Figure 4.18** A schematic diagram of the SMOKE experimental setup at the BL4 at SPL in SLRI (Chai-ngam et al., 2010).

## CHAPTER V

### RESULTS AND DISCUSSION

The main propose of this work is to investigate the thickness-dependent electronic structure of Ni films on Cu(001) surface by both ARPES and a first-principles energy-band calculation. The obtained information gives understanding of the origin of PMA. The magnetic and structural properties of Ni films have been confirmed by SMOKE and LEED. In this chapter, the electronic structures and magnetic properties of Ni/Cu(001) films have been discussed.

#### 5.1 Normal emission data

First, we studied how the electronic structures develop as the Ni film grows. The energy band structures along  $k_{\perp}$  can be identified in normal-emission ARPES spectra by varying the photon energy. Since the thin film has two-dimensional-like lattice structures, no band dispersion is expected with respect to the surface normal direction. Figure 5.1 shows the photon energy dependence of normal emission ARPES spectra on the Ni/Cu(001). The photon energy is increased in 4-eV steps from 40 to 108 eV and in 2-eV steps from 108 to 110 eV, covering the  $\Gamma$  to X points in the bulk BZ. The probing depth or inelastic electron mean free path (IMFP) is estimated to be about 4.25 to 5.0 Å at a specified photon energy range (Tanuma, Powell, and Penn, 1988).  $k_{\perp}$  along the  $\Gamma$ -X direction ( $\Delta$ -line) in the bulk of Ni and Cu are 1.785 and 1.74 Å<sup>-1</sup>, respectively. The spectra were measured at an incident angle of 20° and 45°.

At an incident angle of  $20^\circ$ , the vector potential ( $\vec{A}$ ) parallel to the surface dominantly contributes to the spectra. However, at an incident angle of  $45^\circ$ , the vector potential perpendicular to the surface effectively contributes to the spectra even though  $\vec{A}$  parallel to the surface still remains. For this experiment, all spectra are excited with a linearly polarized light. According to the dipole selection rule for linearly polarized light on the (001) surface (Hermanson, 1977), the *s* and *p* polarizations excite the initial states of odd and even symmetries with respect to the mirror plane corresponding to the excitation of the  $\Delta_5$  and  $\Delta_1$  initial state symmetries, respectively (Table 2.1). In Figure 5.1, the features on the spectra measured at an incident angle of  $20^\circ$  are represented by circles, while triangles denote the features of  $45^\circ$ . Note that, in this experiment, the plane of incidence was set in the off-mirror plane geometry, so the dipole selection rule mentioned above does not work. However, in the other sense, all possible initial state symmetries are into the spectra.

The Cu *3d* states around 2-4 eV binding energy for 0.6 ML show a significant dispersion with  $k_\perp$  and in reasonable agreement with those in the energy band calculation and experiment (Burdick, 1963; Rader et al., 2009). However, the Ni *3d* states do not have any dispersion due to the non-periodic potential normal to the surface. Two peaks are observed at a binding energy of 0.2 and 0.5 eV with excitation energy below 72 eV, and a single peak at 0.5 eV of binding energy is observed at photon energy above 76 eV. At 3.6 ML, the Ni *3d* states are appeared at 0.25 and 0.5 eV in high photon energies, and three peaks are observed at 0.5, 1.1, and 1.3 eV in low photon energies as non-dispersive bands. However, the peak at 0.5 eV is not clearly distinguishable as observed in the spectra of 0.6 ML. The feature at 0.5 eV is

expected to be the interface electronic structure. Various dispersive bands seem to be developed from those at 3.6 ML and more recognizable at 6.3 ML. In the spectra at 6.3 ML, the three non-dispersive peaks observed at 3.6 ML are still recognizable except the peak at 0.5 eV resulting from the interface state.

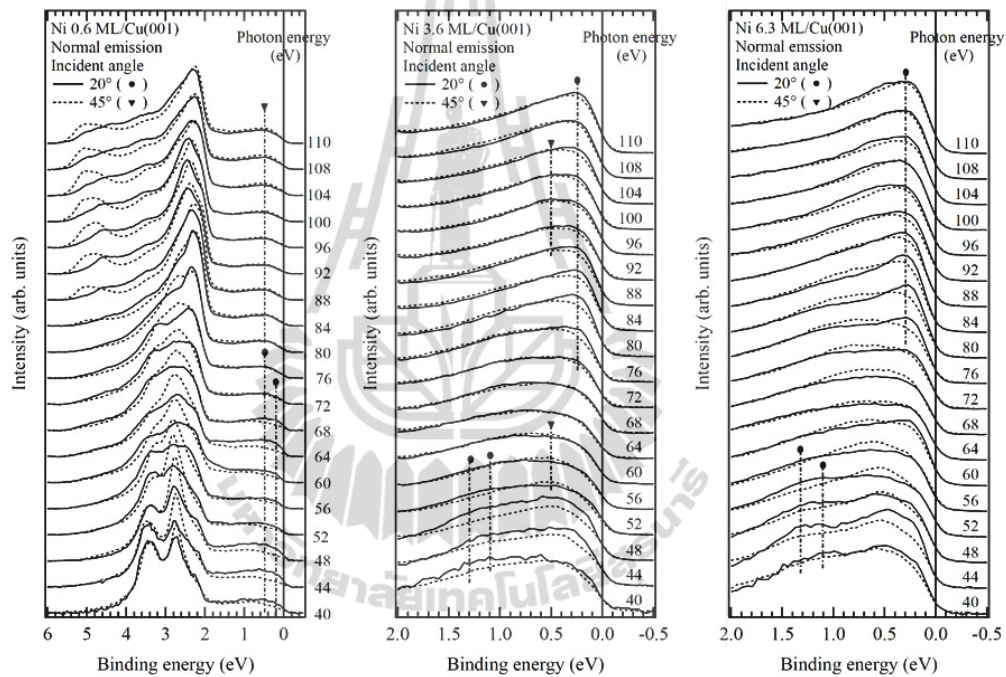


**Figure 5.1** Photon energy and symmetry dependence obtained from normal-emission ARPES spectra on film thicknesses of 0.6, 3.6, and 6.3 ML. Two incident angles of  $20^\circ$  and  $45^\circ$  were applied for the photoelectron excitation with a photon energy from 40 to 110 eV. The  $\Gamma$  and X points correspond to 44 and 108 eV, respectively.

The obtained information from normal-emission spectra indicates that the three non-dispersive bands at 0.25, 1.1, and 1.3 eV in the spectra for 3.6 ML originate from the two-dimensional film band formed in the Ni film, because they are clearly distinguished in the thick films. However, the band at 0.5 eV originates from the interface band because it is difficult to observe that profile in the thick films. In the spectra for 6.3 ML, the dispersive bands resemble to the three-dimensional film band structure, which are gradually formed above 3.6 ML. So that the electronic structure of Ni films shows a bulk-like electronic structure at a thickness above 3 ML.

## 5.2 Surface energy band dispersion along $\bar{\Gamma} - \bar{\Delta} - \bar{X}$ direction

In order to clarify the thickness dependence of surface electronic structures, the angular distribution of photoelectrons data was measured. The development of the electronic structure along the  $\bar{\Delta}$  direction as a function of Ni film thickness is shown in Figures 5.3 to 5.11. The spectra were measured at emission angles of  $0^\circ$  to  $17^\circ$  with the Ni film thicknesses up to 30 ML. The incident angle of light was set in either  $20^\circ$  or  $45^\circ$ . The excited photon energy was fixed at 44 eV corresponding to the  $\Gamma$  point of the bulk BZ.

Because the photoionization cross sections are nearly equivalent for the Ni and Cu  $3d$  electrons in the soft x-ray energy range, all spectra as shown in the figures were normalized with their integrated intensities. We employed  $p$ -polarized light with the vector potential parallel to the plane of incidence ( $\bar{A}_\parallel$ ), within a mirror plane of  $\bar{\Delta}$  direction, and the ARPES analyzer was deployed in the mirror plane. According to the dipole selection rule, the dipole operator  $\bar{A} \cdot \bar{P}$  is even (odd) if  $A$  is parallel (perpendicular) to the mirror plane. Therefore, our ARPES geometry tells us only

even initial states with respect to the  $\bar{\Delta}$  mirror plane. So that the bands with  $d_{z^2}$  and  $d_{x^2-y^2}$  orbital characters are possibly excited in off-normal emission ARPES spectra corresponding to  $\bar{\Delta}_1$  and  $\bar{\Delta}_2$  symmetries, respectively (Hermanson, 1977). Because the surface BZ coordinate (Figure 5.2) described in our  $d$  orbital representations is different by  $45^\circ$  from the bulk BZ coordinate,  $\Delta_2$  corresponds to  $\bar{\Delta}'_2$ , and  $\Delta'_2$  to  $\bar{\Delta}_2$ . In connection with the bulk state, the  $\bar{\Delta}_2$  state is possibly converged into the  $\Gamma'_{25}$  state decomposing into  $\bar{\Delta}'_2$  and  $\bar{\Delta}_5$  as shown in Appendix C. The selection of the initial state symmetries depends on the direction of the vector potential to normal to surface. If the vector potential ( $\vec{A}$ ) is parallel to the surface, the initial state with the  $\bar{\Delta}_5$  band is preferably excited in normal emission as discussed in the previous section. If the vector potential is perpendicular to the surface then the initial state with the  $\bar{\Delta}_1$  band is dominantly excited. In off-normal emission,  $\bar{\Delta}_2$  is possibly excited. In this experiment, it should be noted that the initial states of all both symmetries are possibly observed for both incident angles of  $20^\circ$  and  $45^\circ$ , since the ARPES analyzer and vector potential ( $\vec{A}$ ) cannot be definitely aligned in the normal or parallel to the sample surface under our experimental condition.

In Figures 5.3 to 5.11, the Cu  $3d$  bands are located in the binding energy range between 2 and 4 eV, while the Ni  $3d$  bands appear below 2 eV of binding energy. For clean Cu(001) surface, the feature near the  $E_F$  corresponds to the Cu  $4sp$  bands. The intensity of Cu  $3d$  band peaks is reduced as the increasing of the Ni film thickness. At the Ni film thickness above 7 ML, the Cu band does not appear in the spectra due to the short mean free path of photoelectrons.

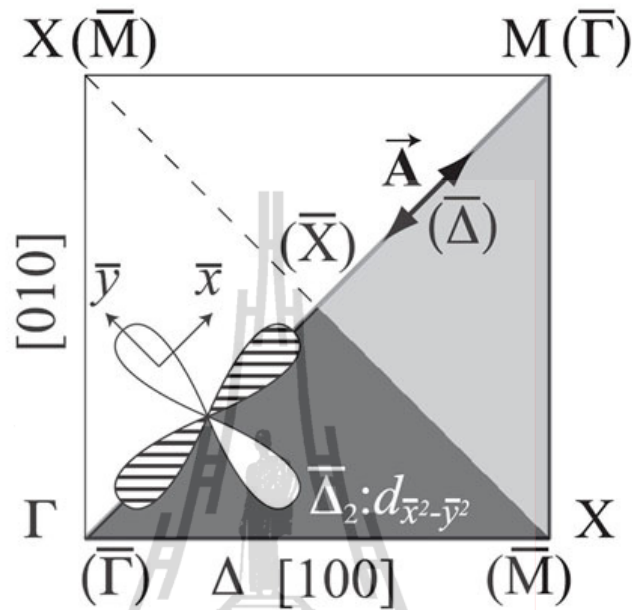


**Figure 5.2** A simple drawing of the  $d_{\bar{x}^2-\bar{y}^2}$  orbital along the  $\bar{\Delta}$  mirror plane in the surface BZ coordinate. The bulk BZ (light gray) is also shown including the surface BZ (dark gray). In this figure, irreducible representations and coordinates in the surface BZ are described with a overline and parentheses.

Figure 5.3 shows the ARPES spectra measured at normal emission. The Ni 3d bands are dominated by two-peak structure. At the Ni film thicknesses below 3ML, the two-peak structure displays in the broad features around 0.32 and 0.66 eV, and they separate as peaks at 0.45 and 1.15 eV for film thicknesses above 3 ML. The energy positions agree with previous published photoemission data on Ni/Cu(100) at normal emission (Thompson and Erskine, 1985; Pampuch et al., 2001). On the basis of the reported calculations of Cu monolayers (Noffke, Brunn, and Hermann, 1978), the peak positions at 0.32 and 0.66 eV are assigned to  $\bar{\Gamma}_5$  and  $\bar{\Gamma}_1$ , respectively. The

energy position at 0.45 eV for thicker thicknesses originates from the  $\Delta_1$  band converging to  $\Gamma_{12}$ , and the peak at a binding energy of 1.15 eV originates from the  $\Delta_5$  band converging to  $\Gamma'_{25}$ . These states are due to a formation of two-dimensional band structures including surface, interface, and film depending on the Ni film thickness. It can be concluded that each peak component in the broad feature is varied its intensity with increasing film thickness as denoted by the lines with dots in Figure 5.3. Considering the spectra measured in two incident angles, the measured spectra show small differences. At an incident angle of  $45^\circ$ , the intensity of the energy position at 0.45 eV in 4.7 and 6.6 ML smaller than that in the spectra measured at an incident angle of  $20^\circ$ . However, the intensity of this peak becomes higher than that in the spectra measured at an incident angle of  $20^\circ$  for the Ni film thickness above 20 ML due to the developing of  $\Gamma_{12}$  state of the bulk electronic structure. In terms of energy position, the normal-emission spectra do not show any significant thickness and polarization dependences. However, the corresponding spectra with increasing the emission angle clearly show the dependence of the thickness and polarization.

Figure 5.4 shows the ARPES spectra measured at an emission angle of  $2^\circ$ . The peak positions appeared at this emission angle are similar to the spectrum measured at normal emission, except in the high binding energy from 1.2 to 1.4 eV. One peak at 1.25 eV in 4.7 ML shifts to a high binding energy of 1.4 eV above 6.6 ML. For the Ni film thickness of 20 ML, the small differences of spectra measured in two incident angles can be observed with the equivalent intensity. At an incident angle of  $20^\circ$ , the peak position appears at 0.35 eV while peak is seen at 0.45 eV of a  $45^\circ$  incidence.

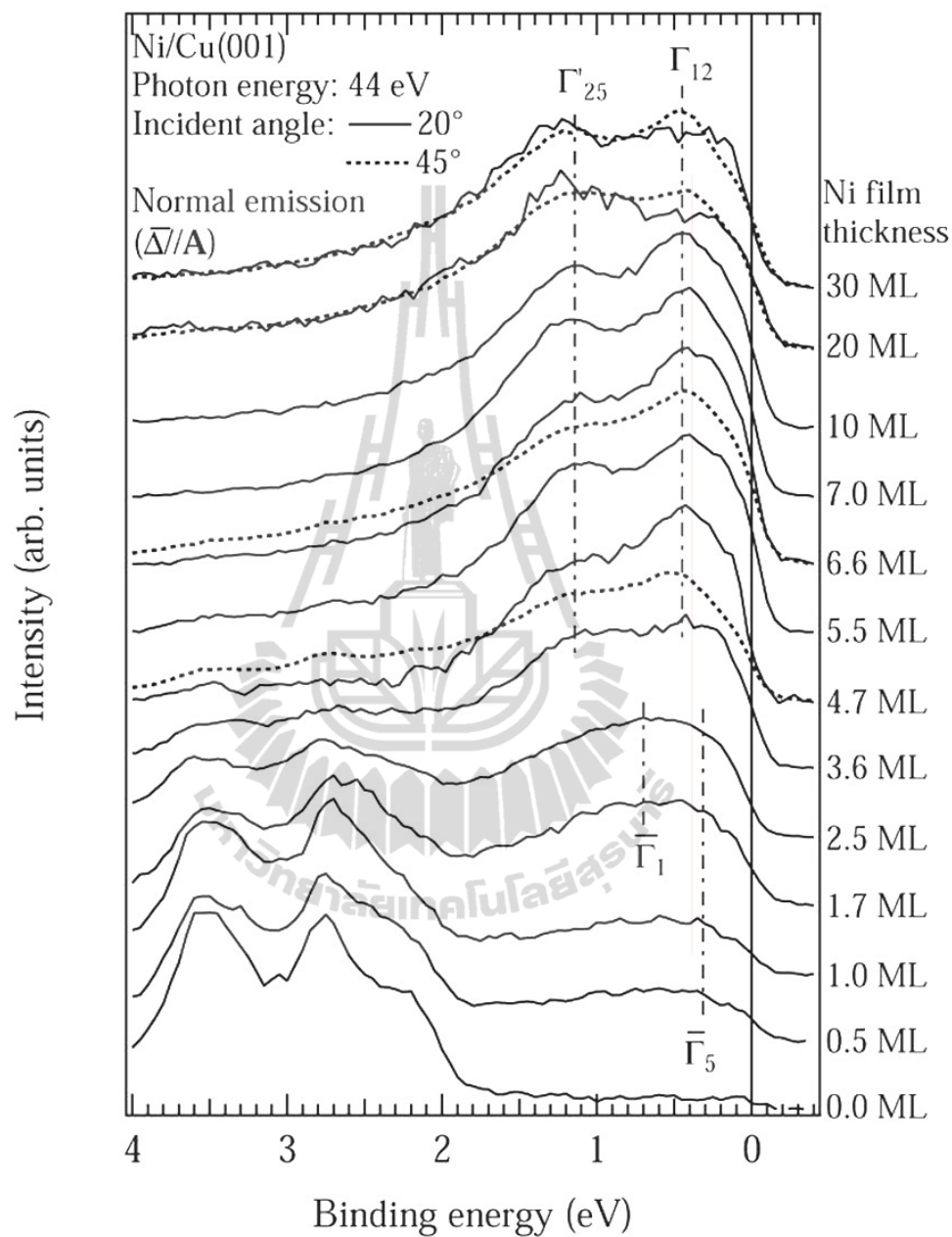


**Figure 5.3** Thickness dependence of ARPES spectra on the Ni/Cu(001). Spectra were measured at normal emission for various thicknesses as indicated on the right hand side of each spectrum. The photon energy and incident angle are 44 eV and 20°. Some spectra at an incident angle of 45° are also shown.

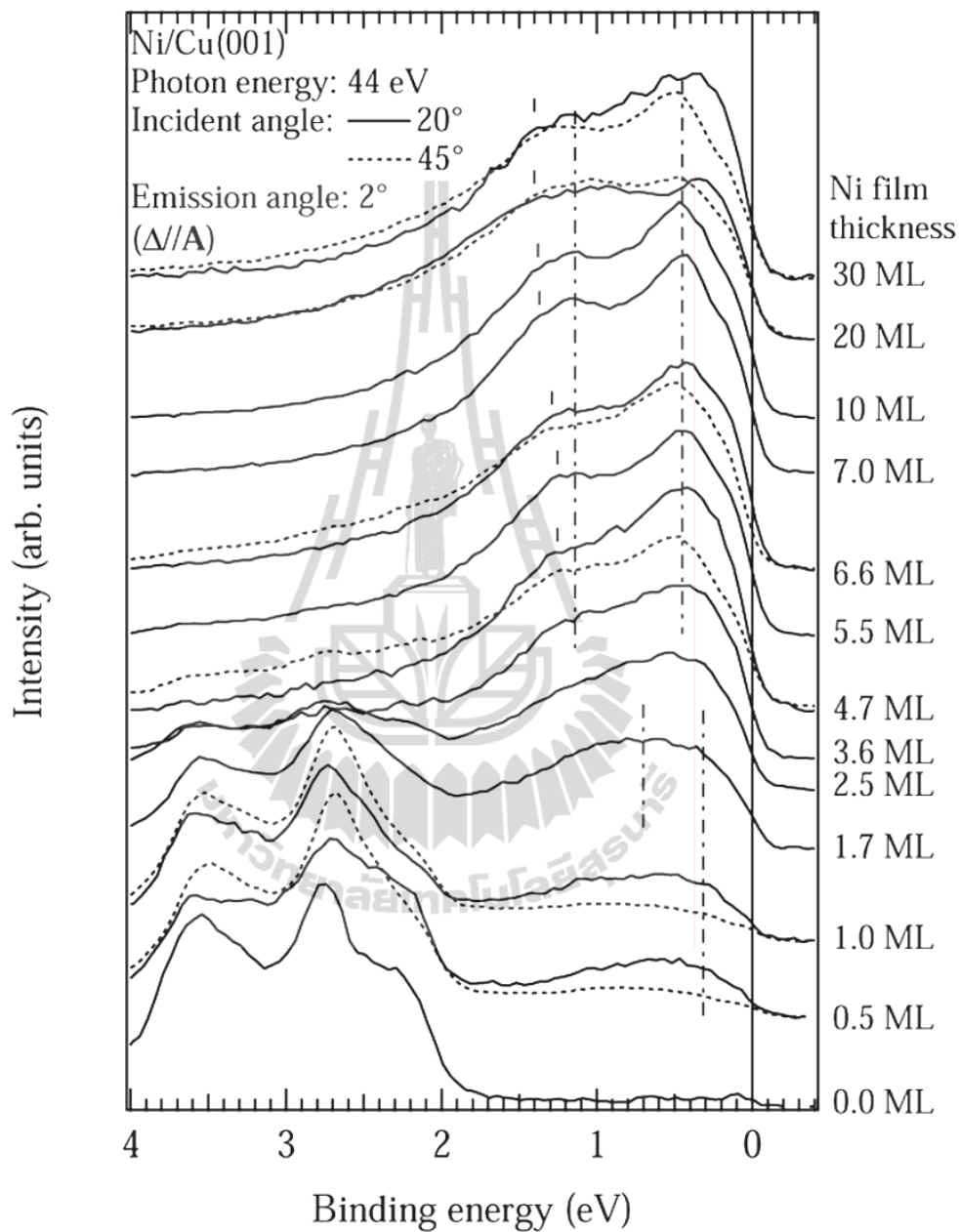


**Figure 5.4** Thickness dependence of ARPES spectra on the Ni/Cu(001). Spectra were measured at an emission angle of  $2^\circ$  for various thicknesses as indicated on the right hand side of each spectrum. The photon energy and incident angle are 44 eV and  $20^\circ$ . Some spectra at an incident angle of  $45^\circ$  are also shown.

The ARPES spectra measured at an emission angle of  $4^\circ$  are shown in Figure 5.5. Below 1.7 ML, a single peak is observed at 0.75 eV while two peaks appear at 0.4 and 0.95 eV for 1.7 ML. At an incident angle of  $20^\circ$ , the former peak shows a slightly shift to binding energy of 0.45 eV for 2.5-20 ML but shifts to binding energy of 0.55 eV in 30 ML. The latter peak shows a shift to high binding energy of 1.1 eV up to 30 ML. The feature in the high binding energy range shows a slight shift from 1.25 eV in 4.7 ML to 1.3 eV above 5.5 ML. At an incidence angle of  $45^\circ$ , one peak at 0.45 eV in 2.5 ML slightly shifts to a binding energy of 0.5 eV in 30 ML. The peak intensities in incident angles of,  $20^\circ$  and  $45^\circ$  are almost equivalent each other in 6.6 ML.

Figure 5.6 shows the ARPES spectra measured at an emission angle of  $6^\circ$ . The energy positions in each thickness are similar to those at an emission angle of  $4^\circ$  except for the spectrum of 1.7 ML. Two peaks are observed with a slight shift to a low binding energy. In the high binding energy range, one peak at 1.2 eV in 4.7 ML shifts to a high binding energy of 1.4 eV above 6.6 ML.

The bands related to the  $\bar{\Delta}_1$  and  $\bar{\Delta}_2$  symmetries, which is corresponding to the band with  $d_{z^2}$  and  $d_{x^2-y^2}$  orbital characters, are clearly distinguished at an emission angle from  $8^\circ$  to  $17^\circ$  as shown in Figures 5.7 to 5.11. The thickness dependences of corresponding spectra are observed above 3 ML when the emission angle increases. For the spectra measured at an incident angle of  $20^\circ$  as shown in Figure 5.7, the peak at 0.5 eV in 2.5 ML shifts to a low binding energy of 0.28 eV at 6.6 ML and shifts back to a high binding energy of 0.35 eV above 6.6 ML. The peak at 1.1 eV in 3.6 ML shifts to a high binding energy of 1.5 eV above 6.6 ML. At an incident angle of  $45^\circ$ , the former peak shows slightly shifts to low binding energy from 0.4 eV in 4.7

ML to 0.33 eV in 6.6 ML. However, the peak at 1.6 eV in 6.6 ML does not appear in the spectra, so this peak originates from the band related to  $d_{x^2-y^2}$  orbital.

In the spectra measured at an emission angle of  $10^\circ$  (Figure 5.8), the peak at 0.42 eV in 2.5 ML shifts to a low binding energy of 0.23 eV at 6.6 ML, and the peak in the high binding energy shifts from 1.62 eV in 5.5 ML to 1.78 eV up to 10 ML at an incident angle of  $20^\circ$ . At an incident angle of  $45^\circ$ , the former peak shows a slight shift from 0.35 eV in 4.7 ML to 0.3 eV up to 20 ML. It was found that the peak intensities from 0.2 to 0.3 eV observed in both incident angles are almost similar each other, while slightly different energy positions upon the polarization are observed. These results suggest that two peaks are overlapped; one observed at an incident angle of  $20^\circ$  originates from the band with  $d_{x^2-y^2}$  orbital, the other in an incident angle of  $45^\circ$  originates from the band with  $d_{z^2}$  orbital. In comparison with the spectra at an emission angle of  $8^\circ$ , the peak position at 1.75 eV in 6.6 ML was not found in the spectra at a  $45^\circ$  incident angle, so it is reasonable to assign this band to  $d_{x^2-y^2}$  orbital.

In the measured spectrum at an emission angle of  $12^\circ$  (Figure 5.9) and an incident angle of  $20^\circ$ , the peak observed at an emission angle of  $10^\circ$  shifts toward  $E_F$  up to 20 ML and shifts back to 0.3 eV in 30 ML. In the high binding energy range, the peak at 1.7 eV in 5.5 ML shifts to 1.8 eV in 10 ML and slightly shifts back to 1.78 eV above. At an emission angle of  $14^\circ$  (Figure 5.10), the peak at 0.2 eV in 3.6 ML shifts to a low binding energy of 0.15 eV at 6.6 ML and shifts to high binding energy above 6.6 ML, while the peak at 1.8 eV in 6.6 ML stays at the fixed binding energy up to 30 ML. The peak position in the low binding energy from  $E_F$  to 0.3 eV obtained in an emission angle of  $14^\circ$  show shifts to high binding energy at an emission angle of  $17^\circ$  in the

both incident angles as shown in Figure 5.11. The peak at 1.6 eV in 5.5 ML shifts to a high binding energy of 1.9 eV up to 30 ML.

All the energy band dispersions and shifts in the wide range of Ni film thicknesses on Cu(001) surface are summarized in an energy band picture in Figure 5.12. Here, we discuss only two even symmetries on each peak near  $E_F$  with respect to the  $\bar{\Delta}$  mirror plane. In the binding energy below 0.5 eV, the  $\bar{\Delta}_2$  ( $d_{x^2-y^2}$ ) and  $\bar{\Delta}_1$  ( $d_{z^2}$ ) bands shift to lower binding energies as the film thickness increases up to 6.6 and 20 ML, and then shift to higher binding energies above these thicknesses. These shifts are clearly observed in the spectra at an emission angle of  $10^\circ$ , where the wave vector is equivalent to about  $0.55 \text{ \AA}^{-1}$ . Note that the  $d$  orbitals assigned here are one of the basis sets in the surface BZ (Figure 5.2) to discuss the orbital contribution to the magnetic anisotropy. The assignment on their symmetries was found to be in good agreement with the first-principle energy-band calculation as shown in Figure 5.13.

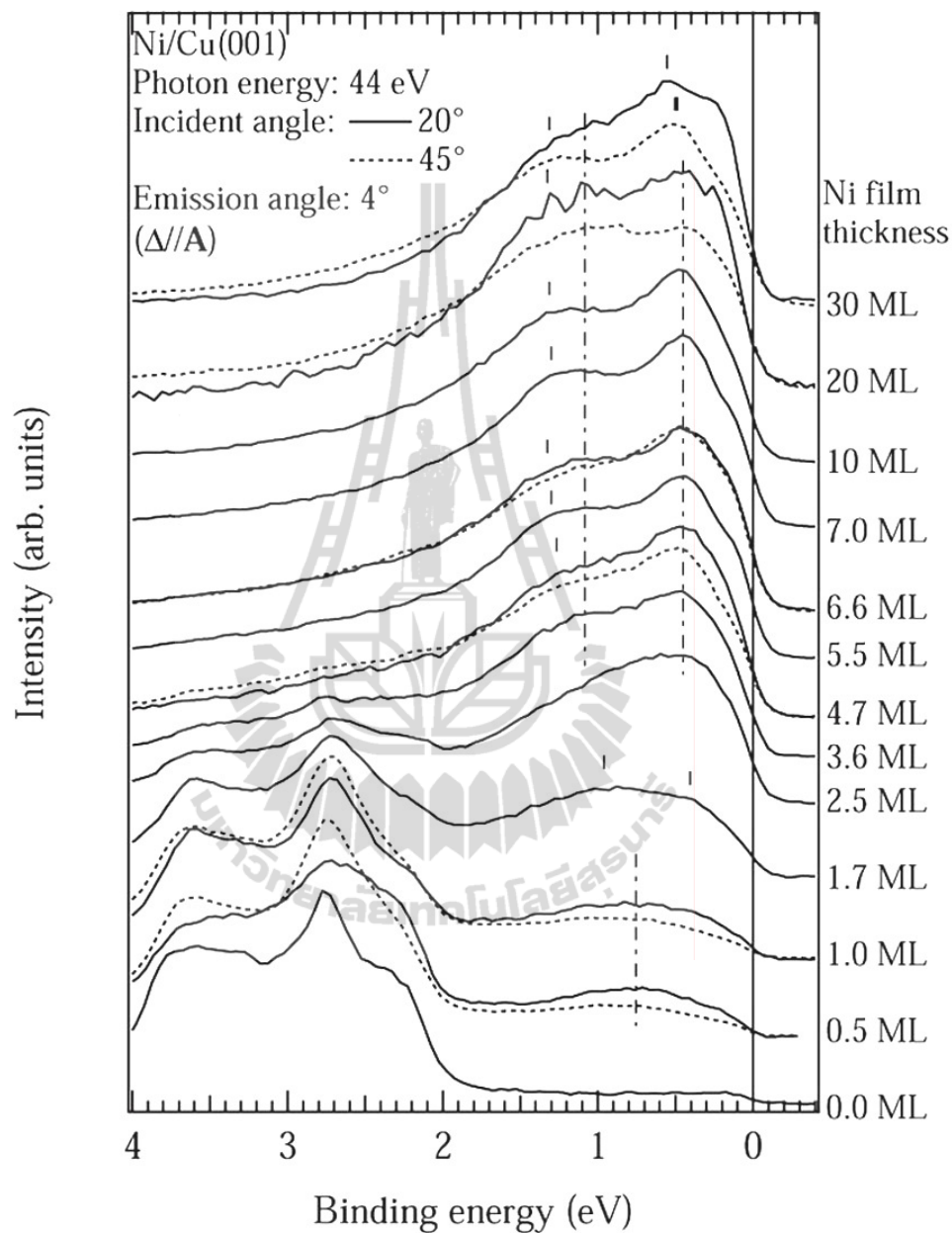


**Figure 5.5** Thickness dependence of ARPES spectra on the Ni/Cu(001). Spectra were measured at an emission angle of  $4^\circ$  for various thicknesses as indicated on the right hand side of each spectrum. The photon energy and incident angle are 44 eV and  $20^\circ$ . Some spectra at an incident angle of  $45^\circ$  are also shown.

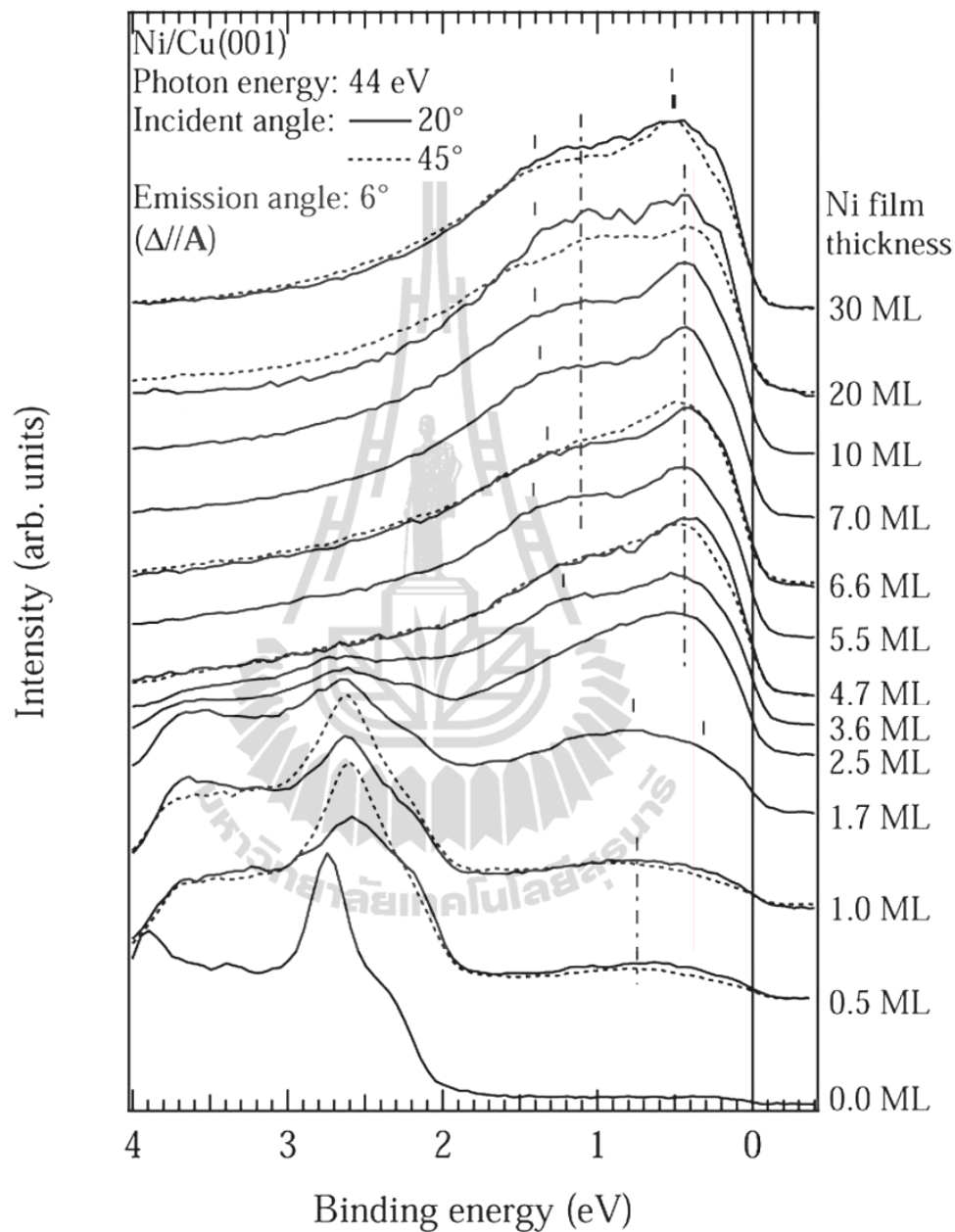


**Figure 5.6** Thickness dependence of ARPES spectra on the Ni/Cu(001). Spectra were measured at an emission angle of  $6^\circ$  for various thicknesses as indicated on the right hand side of each spectrum. The photon energy and incident angle are 44 eV and  $20^\circ$ . Some spectra at an incident angle of  $45^\circ$  are also shown.

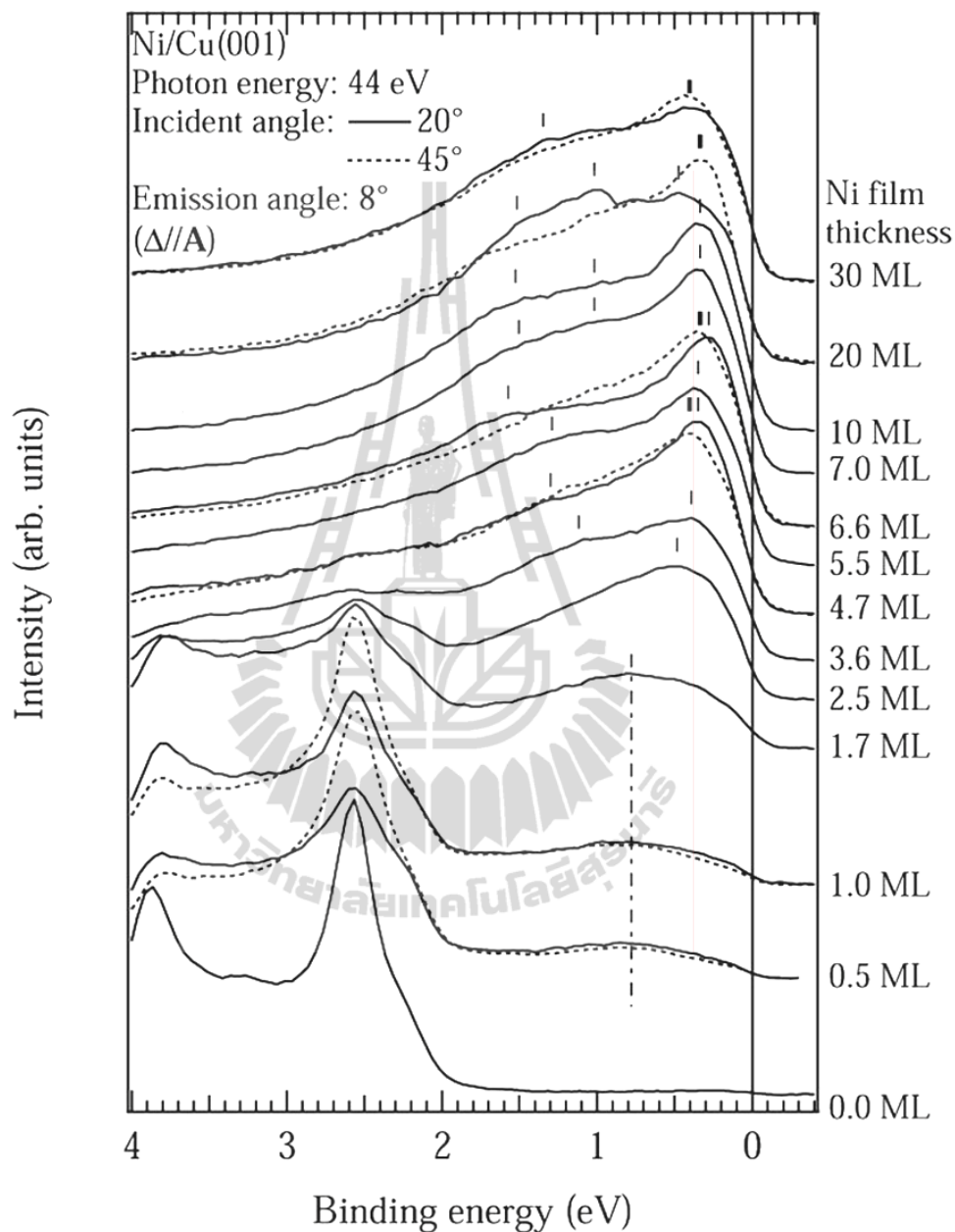


**Figure 5.7** Thickness dependence of ARPES spectra on the Ni/Cu(001). Spectra were measured at an emission angle of  $8^\circ$  for various thicknesses as indicated on the right hand side of each spectrum. The photon energy and incident angle are 44 eV and  $20^\circ$ . Some spectra at an incident angle of  $45^\circ$  are also shown.

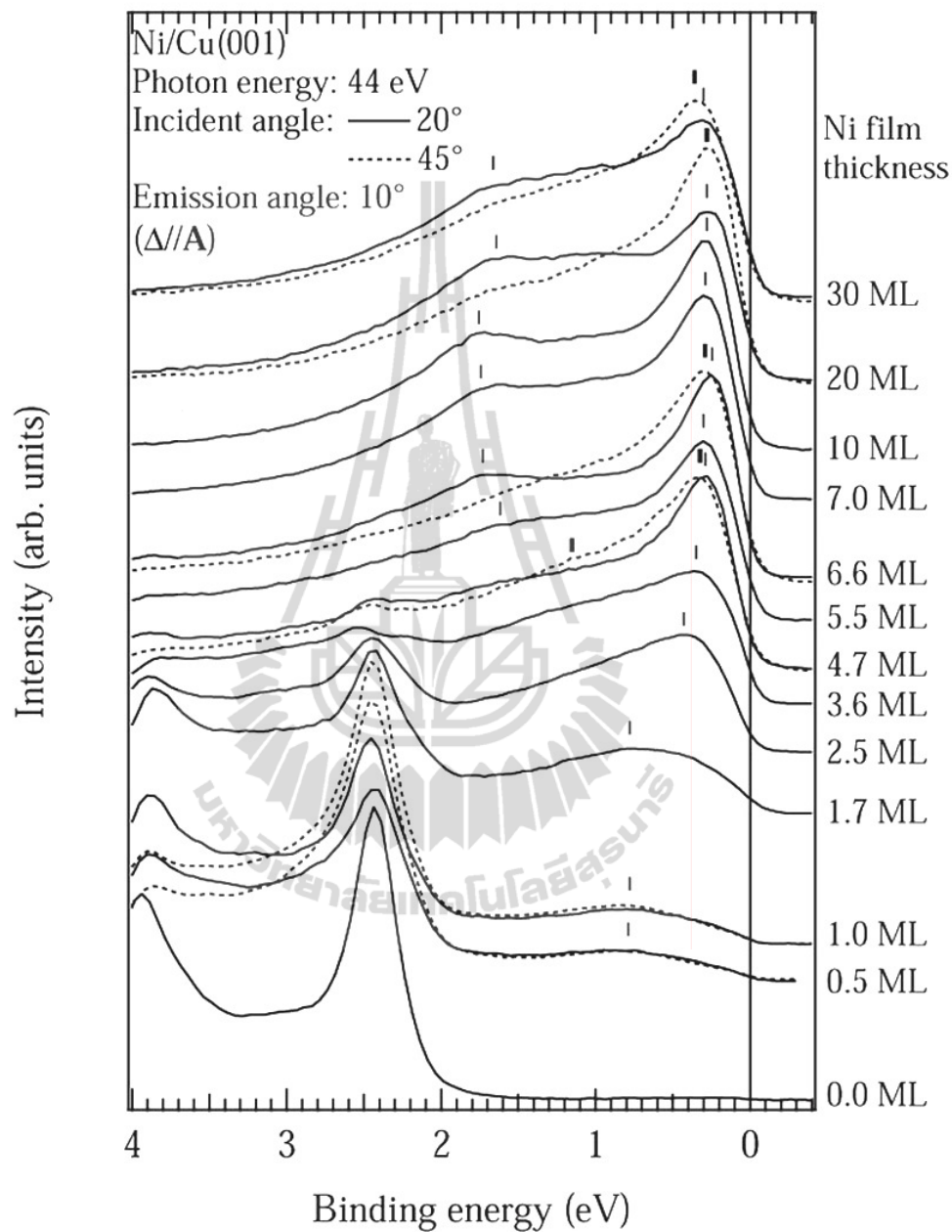


**Figure 5.8** Thickness dependence of ARPES spectra on the Ni/Cu(001). Spectra were measured at an emission angle of 10° for various thicknesses as indicated on the right hand side of each spectrum. The photon energy and incident angle are 44 eV and 20°. Some spectra at an incident angle of 45° are also shown.

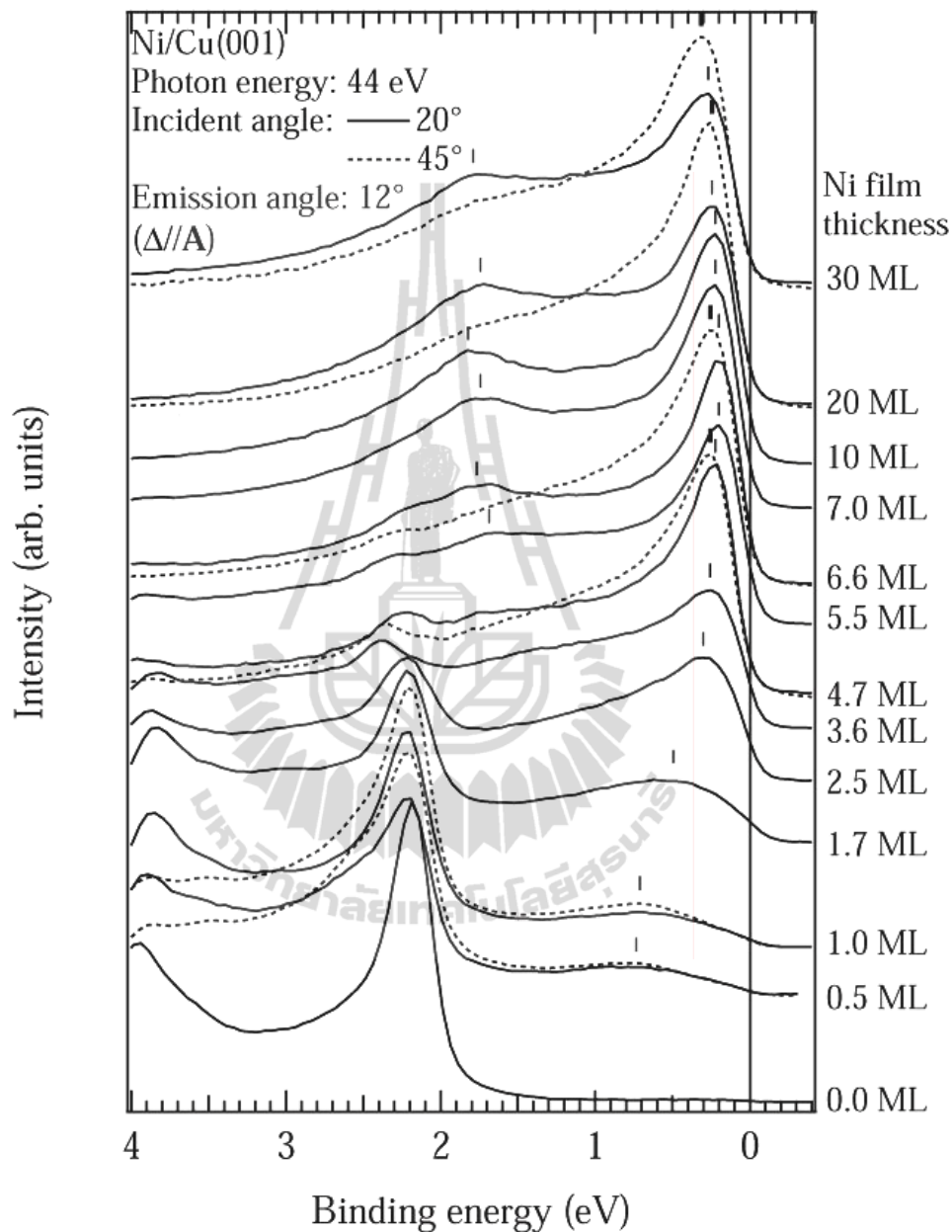


**Figure 5.9** Thickness dependence of ARPES spectra on the Ni/Cu(001). Spectra were measured at an emission angle of  $12^\circ$  for various thicknesses as indicated on the right hand side of each spectrum. The photon energy and incident angle are 44 eV and  $20^\circ$ . Some spectra at an incident angle of  $45^\circ$  are also shown.

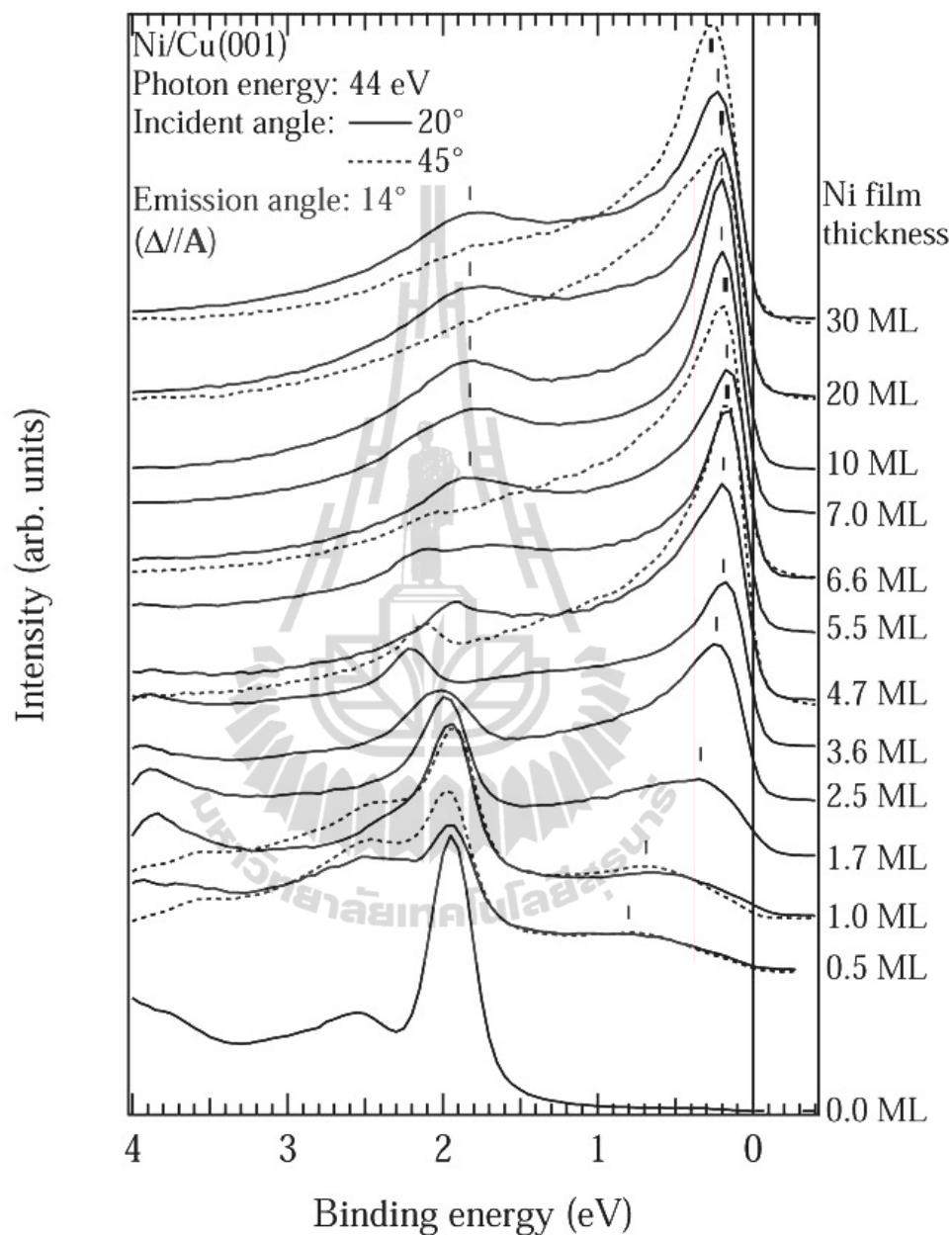


**Figure 5.10** Thickness dependence of ARPES spectra on the Ni/Cu(001). Spectra were measured at an emission angle of  $14^\circ$  for various thicknesses as indicated on the right hand side of each spectrum. The photon energy and incident angle are 44 eV and  $20^\circ$ . Some spectra at an incident angle of  $45^\circ$  are also shown.

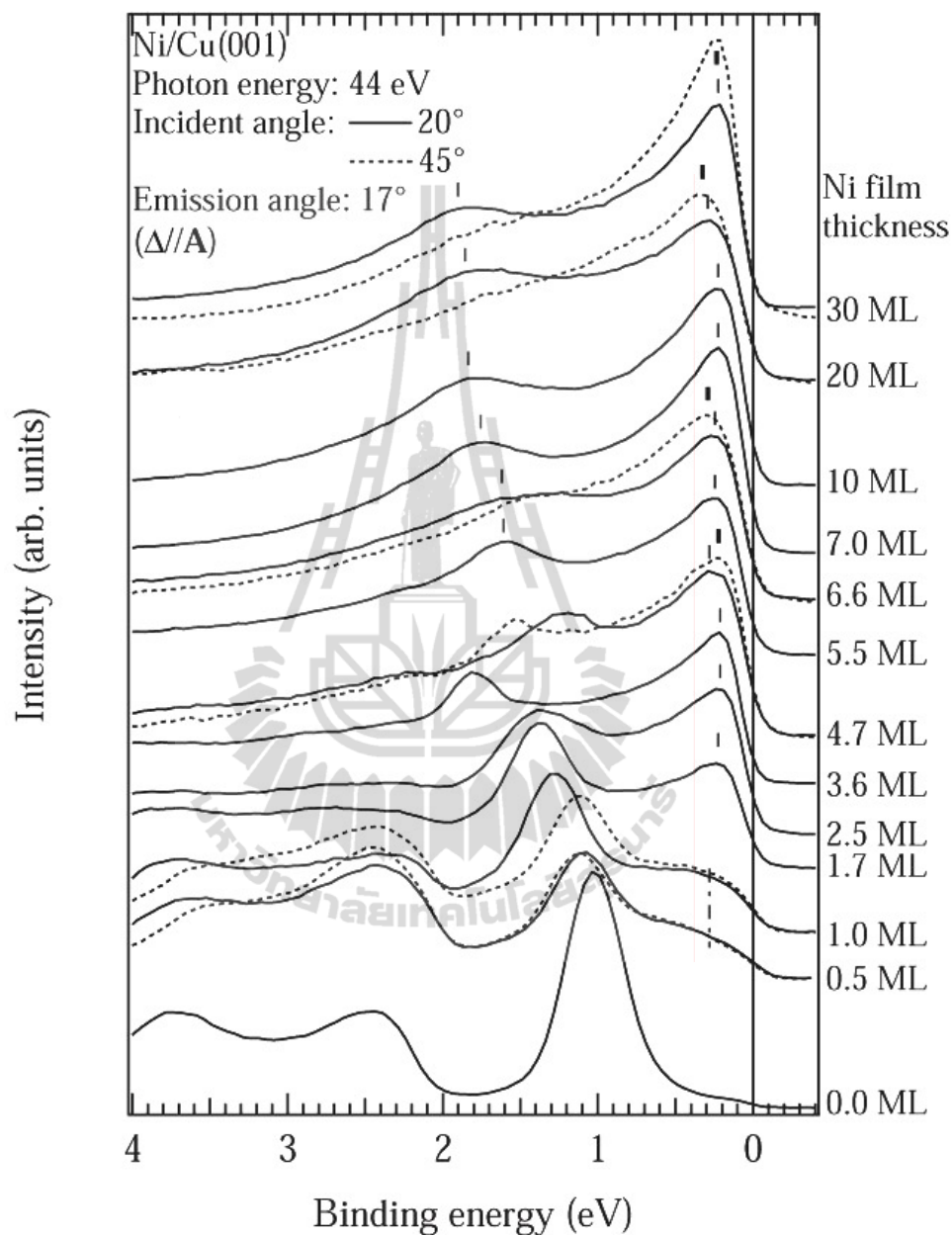


**Figure 5.11** Thickness dependence of ARPES spectra on the Ni/Cu(001). Spectra were measured at an emission angle of 17° for various thicknesses as indicated on the right hand side of each spectrum. The photon energy and incident angle are 44 eV and 20°. Some spectra at an incident angle of 45° are also shown.

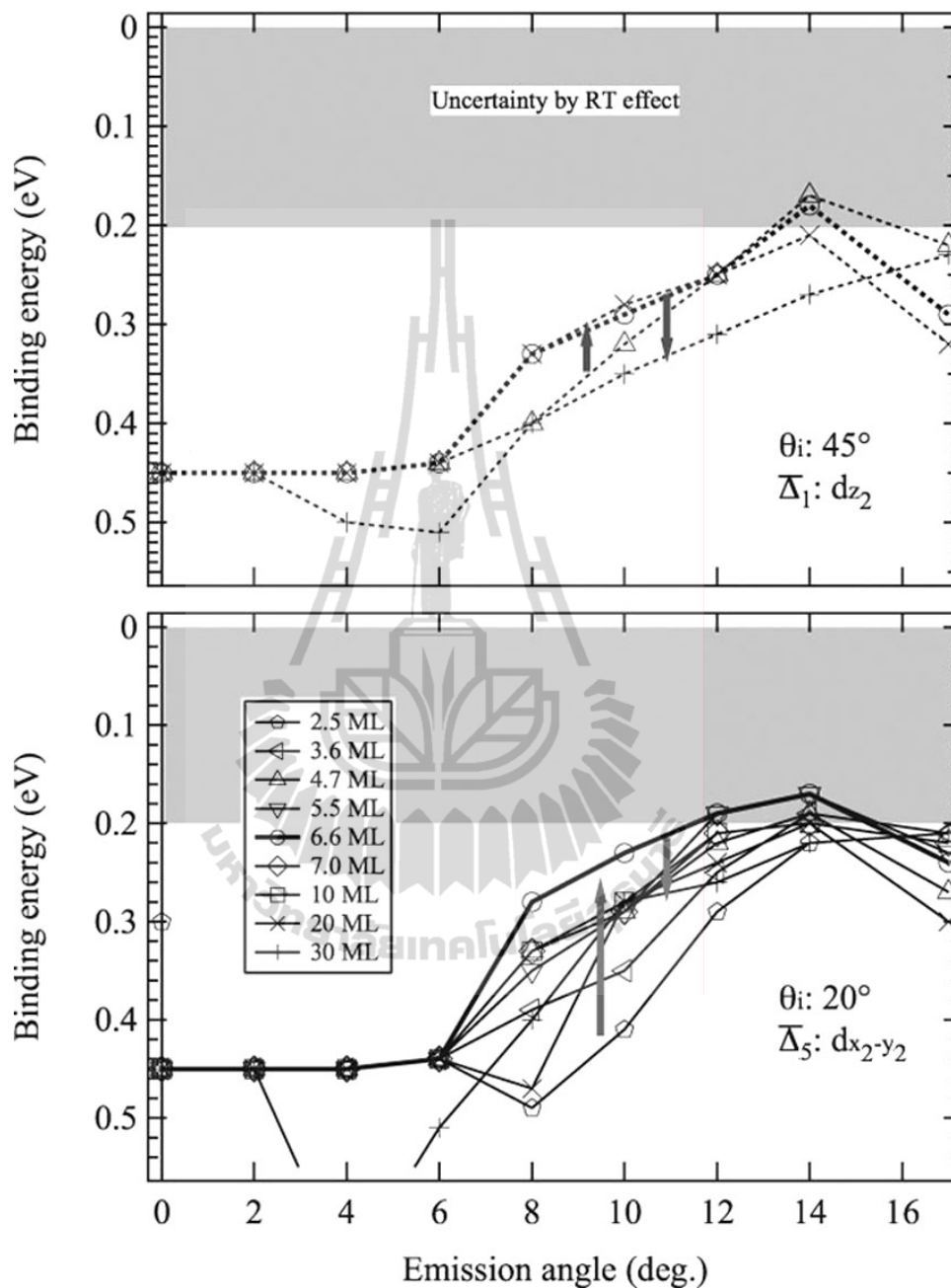


**Figure 5.12** Thickness dependence of energy band structures obtained from ARPES spectra on the Ni/Cu(001). Top figure represents the band structures observed in the spectra measured at an incident angle of  $45^\circ$ , and the band structures observed at an incident angle of  $20^\circ$  shown in bottom figure.

Figure 5.13 shows the calculated  $d$ -orbital dependent energy-band structure for Ni film thicknesses between 3 and 11 ML on both sides of 5 ML-Cu(001) surface, where the repetition of supercell for 5-ML Ni/5-ML Cu(001)/5-ML Ni is shown in Figure 5.14. The calculation was performed for paramagnetic Ni because the  $T_C$  in thin Ni films is lower than room temperature. However, the local magnetic order still remains in the finite temperature above  $T_C$ . Here, the energy-band dispersions are indicated only a thickness-dependent contribution from each  $d$  orbitals to the bands in the middle layer of each Ni film depending on the Ni film thickness. The angular momentum contributed to each band is calculated by projecting the plane-wave components of the eigenstates onto spherical harmonics within atomic spheres. In the energy band dispersion of 7 ML, the band at 1.02 eV at the  $\bar{\Gamma}$  point originates from  $d_{z^2}$  showing a large dispersive  $sp-d$  hybridized band across  $E_F$  and slightly shifts to low binding energy as the Ni film thickness increases. The band at 0.78 eV in 3 ML originates from  $d_{x^2-y^2}$ , showing a dispersion to high binding energy along the  $\bar{\Gamma}-\bar{X}$  direction, which shifts to high binding energy as the Ni film thickness increases. These calculated orbital-resolved energy band dispersions and binding energy shifts depending on the film thickness for each band were found to be in good agreement with the ARPES spectral profiles shown in Figure 5.12. The two-band  $d_{x^2-y^2}$  orbital sets from -0.1 to 0.4 eV and partly shifting to low binding energy might correspond to the peak at 0.2 eV in 6.6 ML observed in the spectra at a  $20^\circ$  incident angle. The calculated energy band dispersion with  $d_{x^2-y^2}$  orbital character shifting toward low binding energies is in agreement with the Ni film thickness up to 6.6 ML, while not with the shift to high binding energy above 6.6 ML.

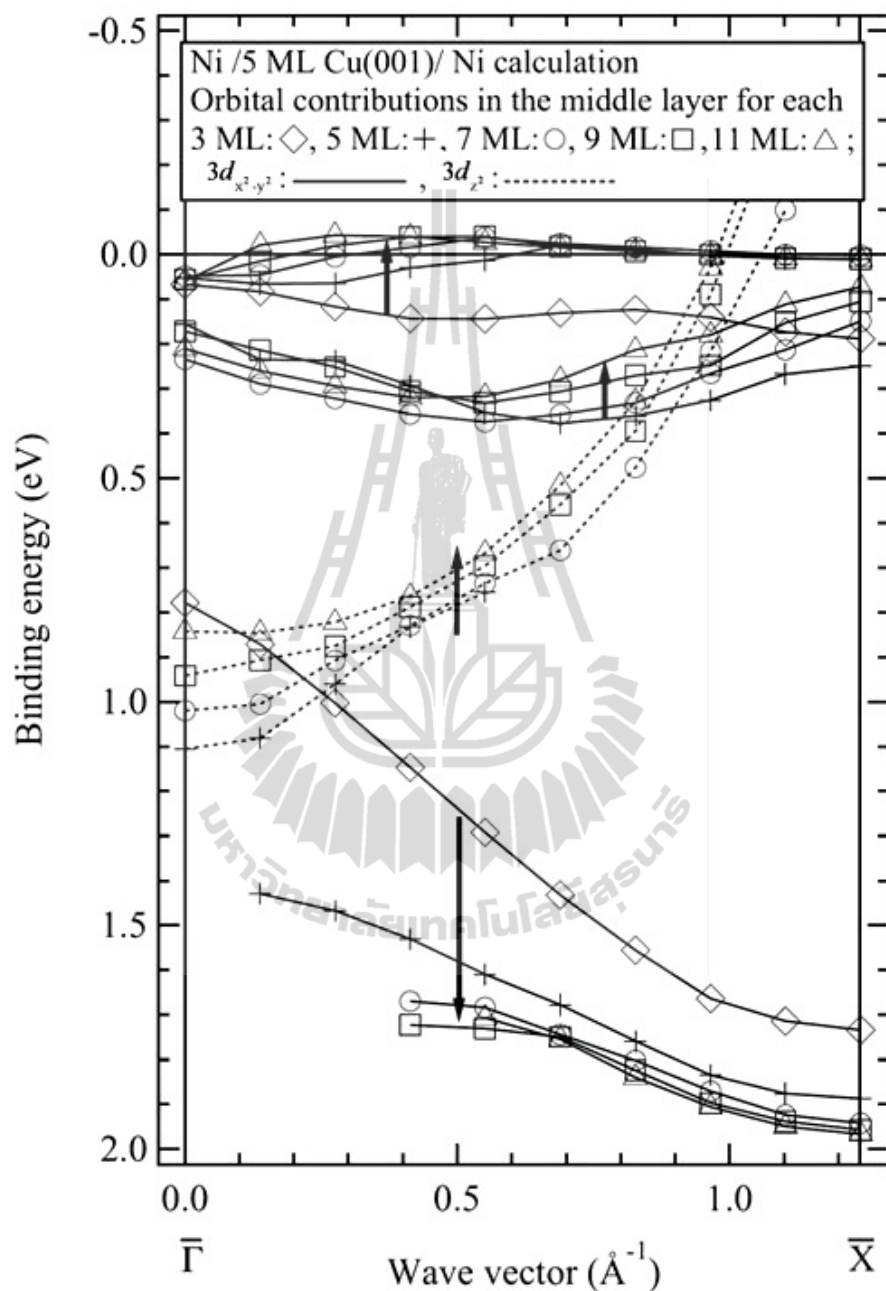


**Figure 5.13** First-principles energy band calculations in paramagnetic Ni films in the Ni/5 ML-Cu(001)/Ni structure. The markers indicate only a contribution from  $d_{x^2-y^2}$  and  $d_{z^2}$  orbitals to the bands in the middle layer of each Ni film, and arrows represent shifts for each  $d$  orbital.

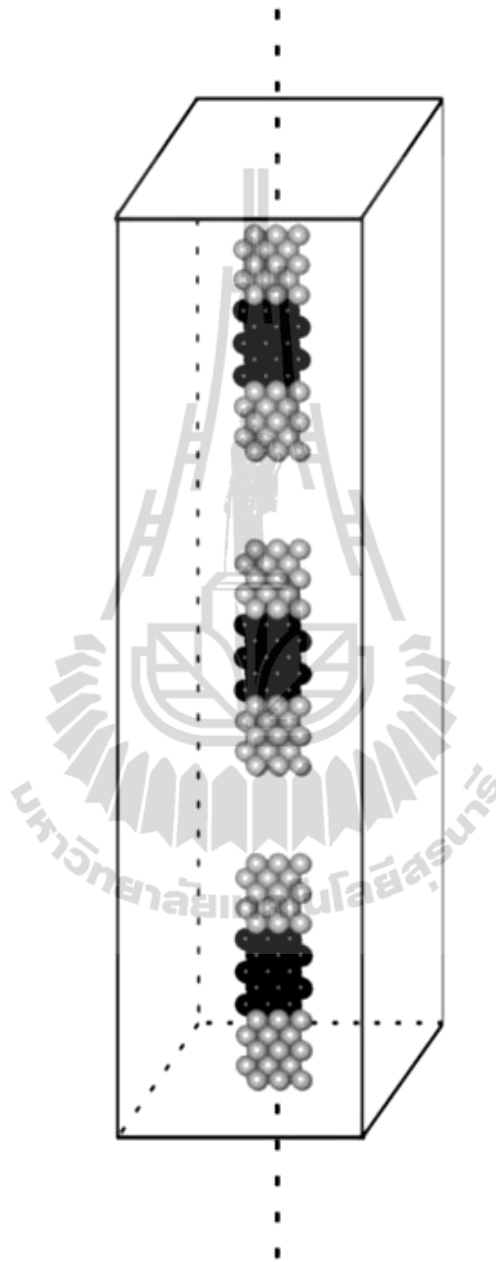


**Figure 5.14** A schematic model of a repetition supercell for 5-ML Ni/5 ML-Cu(001)/5-MLNi structure.

These discrepancies might be due to the limitation in the energy band calculation at a fixed in-plane lattice constant, at which the lattice is only relaxed in the surface normal direction. Since the realistic growth mode may vary in a three-dimensional way as reported in the STM measurement (Figure 5.15) (Shen, Giergiel, and Kirschner, 1995). It was found that the onset of strain relaxation causes the formation of misfit dislocations occurred in thicknesses above 7 ML, but it does not take into consideration in our calculation.

The morphology at various thicknesses of Ni/Cu(100) are shown in Figure 5.15 (a)-(h) measure by Shen et al. (1995). Figure 5.15 (c) shows the STM image of a 3.4-ML Ni film with a very good layer-by-layer growth, although most of the islands are of random shape. Up to 4.5 ML (Figure 5.15 (d)), the islands shape shows nearly rectangular and the height of the islands are in almost the same positions as those of 3.4 ML, this indicates a transition of the growth mode from layer-by-layer to multilayer growth. At a higher thickness of 5.6 ML (Figure 5.15 (e)), the plotted of the cross section showing the coexistence of monolayer and bilayer islands. At 7.1 ML (Figure 5.15 (f)), the marked line profile of the image can be regarded as most of the islands on the surface are three-dimensional platelike islands of rectangular shape. This shape gradually grows in size and height with increasing film thickness (Figure 5.15 (g)-(h)), but the changes of the film morphology have not been detected between 7.1 and 23 ML. Moreover, the rectangular shape is also displayed in our LEED measurements (Figure 5.16). Figure 5.16 (a)-(e) show a LEED pattern of Ni films from 0.5 ML up to 5.2 ML taken at 130 eV, the first order diffraction spots have the circular shape. However, at a higher thickness between 6.7 and 20 ML, the rectangular shape has been detected from the first order diffraction spots, and the size

of this shape become larger in 17.5 and 20 ML. This indicates the three-dimensional growth on surface, corresponding to STM results.

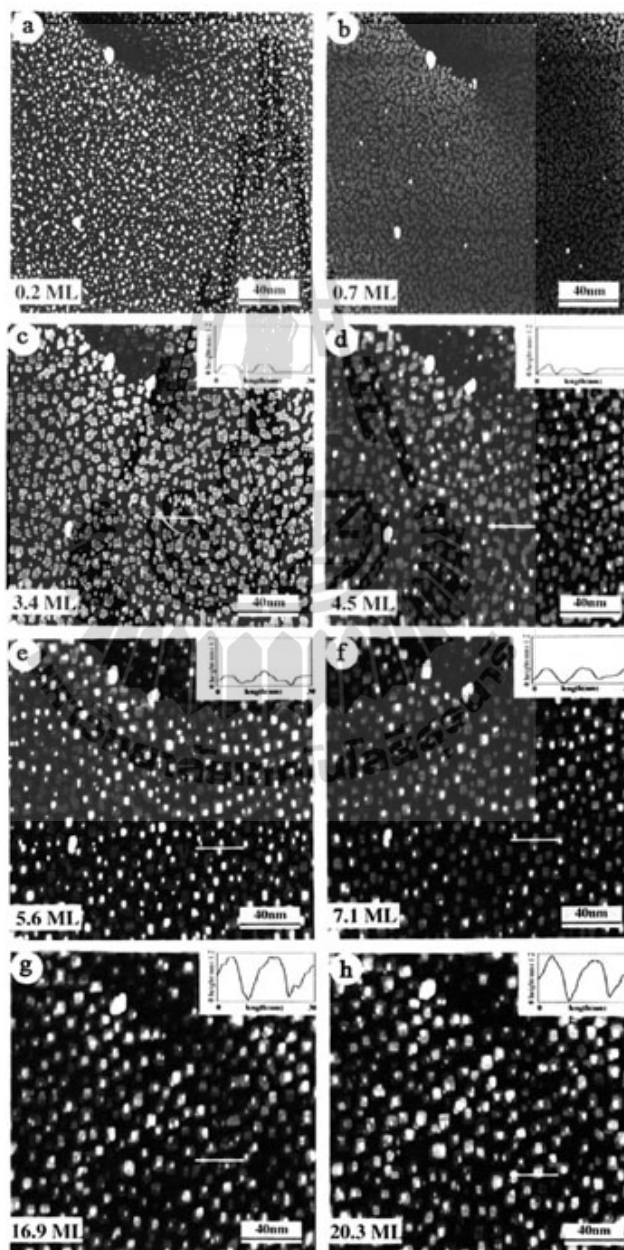


**Figure 5.15** STM images of (a) 0.2 ML, (b) 0.7 ML, (c) 3.4 ML, (d) 4.5 ML, (e) 5.6 ML, (f) 7.1 ML, (g) 16.9 ML, and (h) 20.3 ML Ni/Cu(100) films (Shen, Giergiel, and Kirschner, 1995).

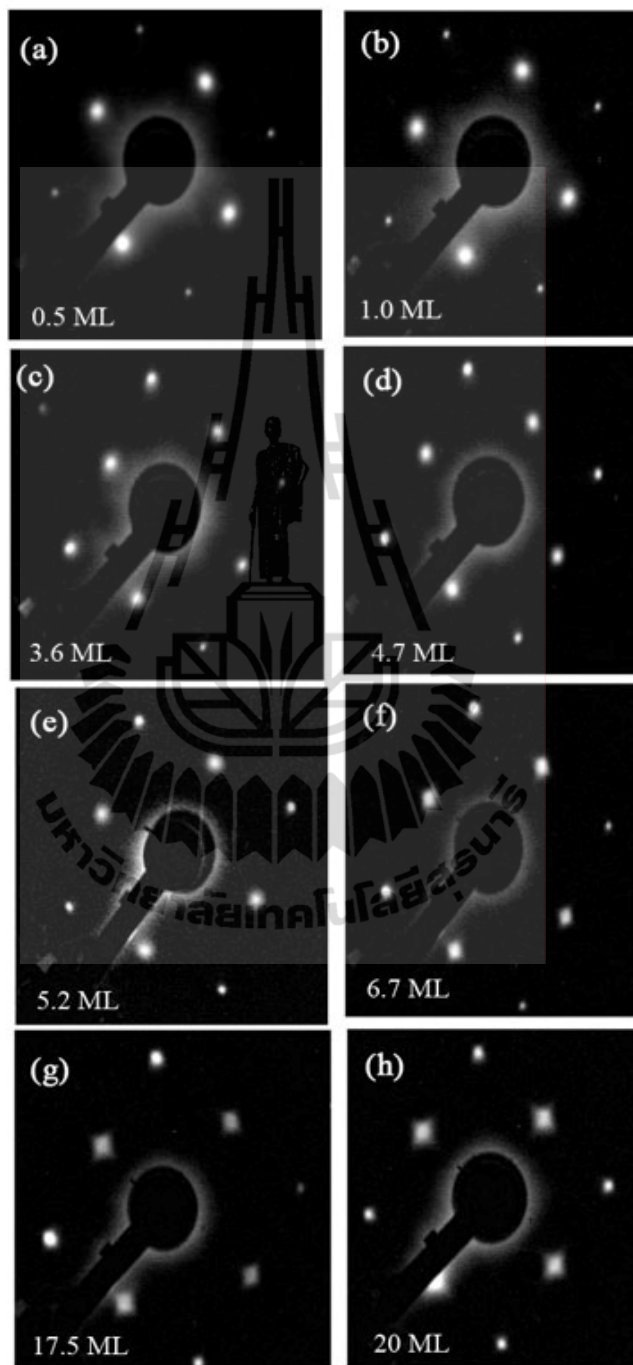


**Figure 5.16** LEED patterns of (a) 0.5 ML, (b) 1.0 ML, (c) 3.6 ML, (d) 4.7 ML, (e) 5.2 ML, (f) 6.7 ML, (g) 17.5 ML, and (h) 20 ML Ni/Cu(001) films taken at an electron energy of 130 eV.

In order to determine the influence of the growth mode during multilayer Ni thin film on the magnetic anisotropy of Ni/Cu(001) system. The calculated surface roughness for various thicknesses observed in RHEED intensity is taken into account. Figure 5.17 taken from simulations by Wu et al. (2008) shows the simulated surface roughness for Ni/Cu(100) system at room temperature with deposition flux of 0.8 ML/min, which is well consistent with the results from STM measurements (Shen, Giergiel, and Kirschner, 1995) as shown above. The surface roughness is generally defined as the average height and diameter of the islands. However, Elsholz and Schöll (2004) studied a surface morphology (roughness) due to the average height of the islands as a function of the total number of deposited. A larger value of roughness corresponds to a morphology that has more layers simultaneously exposed to the surface. The oscillation of roughness with increasing coverage with a periodicity of 1 ML means the layer-by-layer growth mode.

The effect of roughness on the magnetic anisotropy has been proved theoretically by Bruno (1988). The shape anisotropy is reduced as the in-plane demagnetizing fields at the edges of steps created by roughness. Therefore, the anisotropy contribution resulting from the roughness will always be positive, i.e. favoring PMA. Moreover, roughness also introduces step atoms at the interface. These step atoms should reduce the interface anisotropy contribution of magnetocrystalline origin as shown in the first calculations resulting from the presence of defects (MacLaren and Victora, 1994). This demonstrated the importance of the topology of the interface. It is difficult to evaluate the effect of roughness on the energy band because the lattice periodicity disappears on the surface. Molecular orbital calculation might help to simulate the effect of roughness localized in the observed islands in STM. Surfactant

of oxygen on Cu(001) surface was also found to form a flat layer-by-layer structure of Ni films (Hong et al., 2004). It is interesting how the energy band shifts as a function of thicknesses on Ni/O/Cu(001). However, this is out of scope in this thesis.

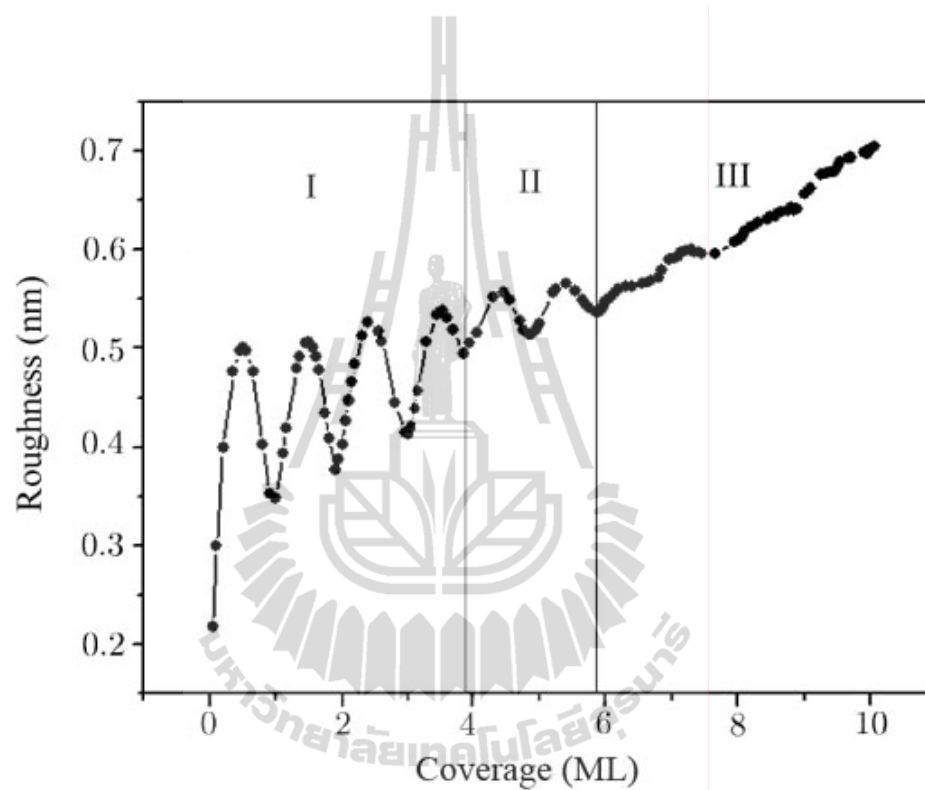


**Figure 5.17** Surface roughness (the average height of the islands) plotted versus total coverage for the Ni/Cu(100) system, which was simulated at room temperature with the deposition flux of 0.8 ML/min (Wu et al., 2008).

### 5.3 Magnetic properties of Ni on Cu(001)

To confirm the magnetic anisotropies in our Ni/Cu(001) films, the results of SMOKE measurements are also shown. Hysteresis curves obtained for both magnetization applied normal and in-plane to the films plane with different Ni thickness are shown in Figure 5.18. It was found that the magnetization was oriented perpendicular to the film plane at room temperature for Ni films thickness above 9 ML.  $T_C$  decreases when the thickness of a film decreases to atomic scale due to finite-size effects. Therefore, SMOKE measurements are also performed at low temperature shown in Figure 5.19. As the temperature decreases, the SRT begins at around 7 ML, and the coercive field also increases. However, the in-plane spin direction has a larger coercive field than the perpendicular magnetized state. The polar magnetization hysteresis curves are observed as square shape at around 17 ML. To determine the critical thickness ( $d_c$ ), in which the transition from perpendicular to in-plane magnetization occurred, the coercive field ( $H_c$ ) plots as a function of film thickness in Figure 5.20. The results in Figure 5.20 show a gradual increase in the coercive field from about 68 Oe to about 91.5 Oe occurred at about 12 ML. At the thickness near 17 ML there is a rapid rise in  $H_c$ , from 104 to 332 Oe. It is well known that the pseudomorphic growth of Ni films continues up to a critical thickness. This fact allows us to interpret that the onset of strain relaxation due to the formation of misfit dislocations begin as the rise of coercive field vs Ni film thickness.

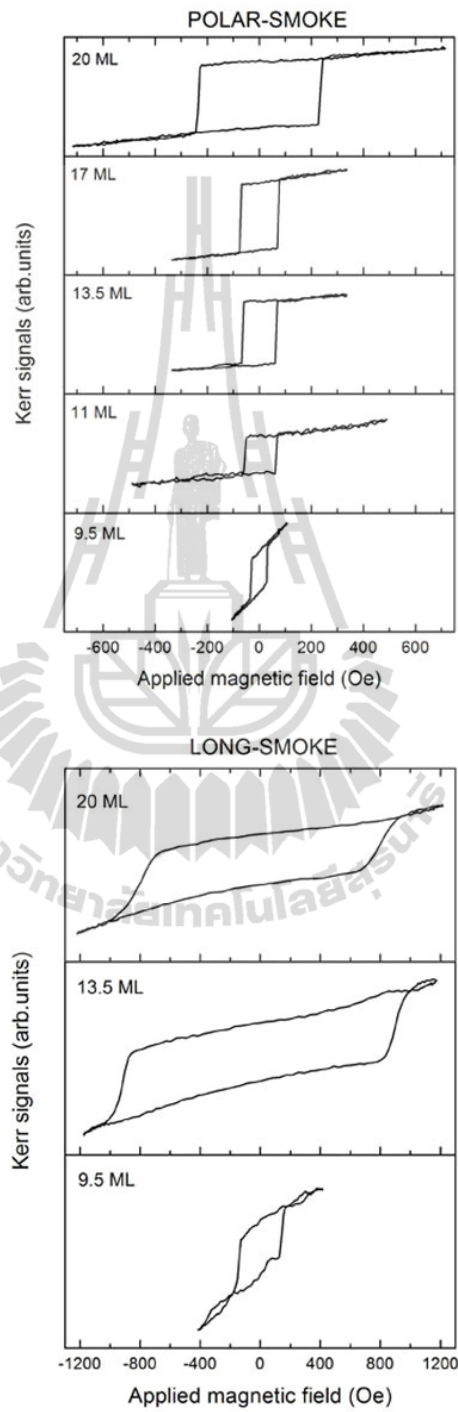


**Figure 5.18** Polar and longitudinal magnetization hysteresis loops for different Ni film thickness on Cu(001) measured at room temperature.

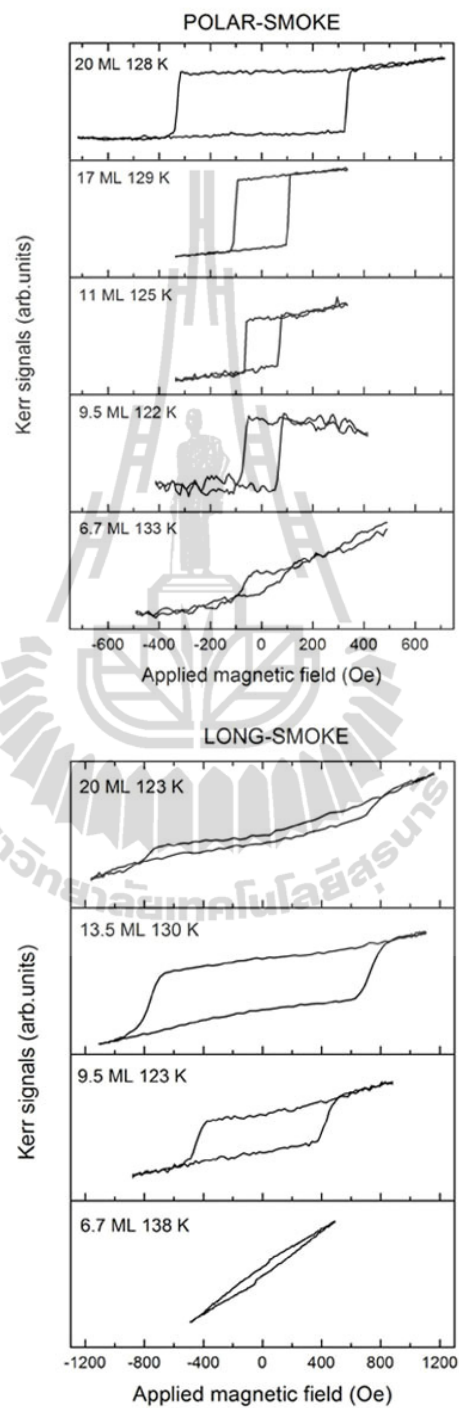


**Figure 5.19** Polar and longitudinal magnetization hysteresis loops of Ni films on Cu(001) measured at several typical temperatures.

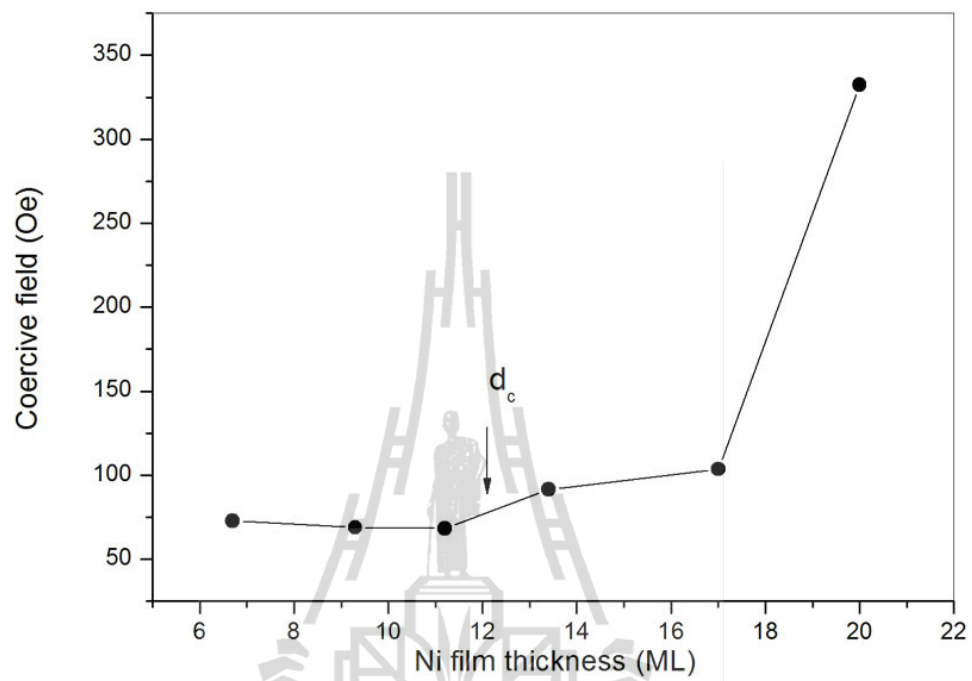


**Figure 5.20** Plot of coercive field as a function of Ni film thickness determined from the polar magnetization hysteresis loops.

# CHAPTER VI

## CONCLUSIONS

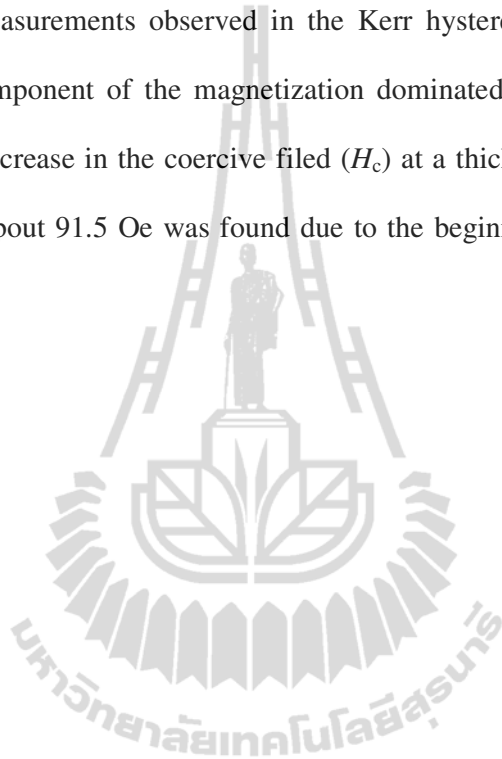
The thesis provides the fundamental understanding of the magnetic anisotropy in Ni films on Cu(001) substrate in terms of the electronic structure as a function of Ni films thickness. The energy band dispersions and MAEs of Ni/Cu(001) surfaces using ARPES combined with the first-principles energy-band calculation are summarized in this chapter.

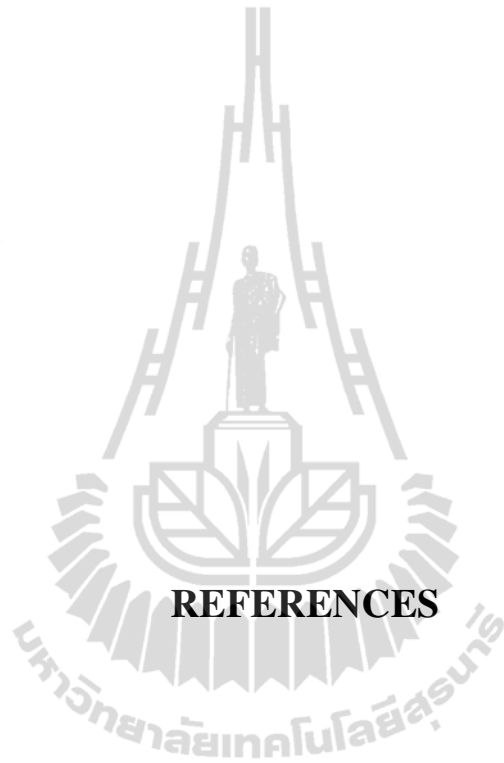
In the normal-emission ARPES spectra along the  $\Gamma$ - $\Delta$ -X line, it was shown that the electronic structure of Ni films on Cu(001) surface was close to that of bulk Ni at the film thickness around 3 ML. All Ni  $d$ -band features showed a gradual transition at a film thickness between 2.5 and 3.6 ML, leading to the change from the 2D into the 3D electronic structures.

In the surface band dispersions along  $\bar{\Gamma}$ - $\bar{\Delta}$ - $\bar{X}$  direction, it was found that the  $d$  electron spins stabilized to the surface perpendicular direction due to the increase of  $d_{x^2-y^2}$  and the decrease of  $d_{z^2}$  orbital occupancies corresponding to the band filling for  $\bar{\Delta}_2$  and  $\bar{\Delta}_1$ , respectively. The observed Ni film thickness dependence of the binding energy shift of Ni 3d states in ARPES spectra profile was found to be in good agreement with the first-principles energy-band calculation. According to the spin-orbit coupling model of PMA, the bands with energy position close to the  $E_F$  play a crucial role in the contribution to PMA.

The results observed in the binding energy shifts and energy band dispersions revealed that the orbital magnetic anisotropy is a key important in the formation of PMA on the Ni/Cu(001) system.

Magnetic measurements observed in the Kerr hysteresis loops revealed that a perpendicular component of the magnetization dominated at the thickness above 7 ML. A gradual increase in the coercive field ( $H_c$ ) at a thickness around 13 ML from about 68 Oe to about 91.5 Oe was found due to the beginning of misfit dislocations formation.





**REFERENCES**

## REFERENCES

- Amemiya, K., Sakai, E., Matsumura, D., Abe, H., and Ohta, T. (2005). Spin-reorientation transition of Ni/Cu(100) and CO/Ni/Cu(100): Separation of the surface and bulk components of the x-ray magnetic circular dichroism spectrum. **Phys. Rev. B** 71(21): 214420 1-7.
- Ashcroft, N. W., and Mermin, N. D. (1976). **Solid state physics**. United States of America: W. B. Saunders Company.
- Baberschke, K. (1996). The magnetism of nickel monolayers. **Appl. Phys. A** 62(5): 417-427.
- Baberschke, K. (1999). The correlation of local structure and magnetism in thin ferromagnetic films. **Surf. Rev. Lett.** 6(5): 735-739.
- Bachelet, G. B., Hamann, D. R., and Schlüter, M. (1982). Pseudopotentials that work: From H to Pu. **Phys. Rev. B** 26(8): 4199-4228.
- Berglund, C. N., and Spicer, W. E. (1964). Photoemission studies of copper and silver: Theory. **Phys. Rev.** 136(4A): A1030-A1044.
- Blöchl, P. E. (1994). Projector augmented-wave method. **Phys. Rev. B** 50(24): 17953-17979.
- Bouckaert, L. P., Smoluchowski, R., and Wigner, E. (1936). Theory of Brillouin zones and symmetry properties of wave functions in crystals. **Phys. Rev.** 50(1): 58-67.
- Bovensiepen, U., Pouloupoulos, P., Farle, M., and Baberschke, K. (1998). The Curie temperature in ultrathin Ni/Cu(001) films determined by ac susceptibility and MOKE. **Surf. Sci.** 402: 396-400.

- Briggs, D., and Seah, M. P. (1996). **Practical surface analysis by Auger and X-ray photoelectron spectroscopy** (2<sup>nd</sup> ed). England: John Wiley.
- Bruno, P. (1988). Dipolar magnetic surface anisotropy in ferromagnetic thin films with interfacial roughness. **J. Appl. Phys.** 64(6): 3153-3156.
- Bruno, P. (1989). Tight-binding approach to the orbital magnetic moment and magnetocrystalline anisotropy of transition-metal monolayers. **Phys. Rev. B** 39(1): 865-868.
- Burdick, G. A. (1963). Energy band structure of copper. **Phys. Rev.** 129(1): 138-150.
- Bylander, D. M., Kleinman, L., and Lee, S. (1990). Self-consistent calculations of the energy bands and bonding properties of B<sub>12</sub>C<sub>3</sub>. **Phys. Rev. B** 42(2): 1394-1403.
- Carcia, P. F. (1988). Perpendicular magnetic anisotropy in Pd/Co and Pt/Co thin-film layered structures. **J. Appl. Phys.** 63(10): 5066-5073.
- Carter, R. L. (1998). **Molecular symmetry and group theory**. New York: John Wiley & Sons.
- Ceperley, D. M., and Alder, B. J. (1980). Ground state of the electron gas by a stochastic method. **Phys. Rev. Lett.** 45(7): 566-569.
- Chai-ngam, R., Rattanasuporn, S., Supruangnet, R., Prawanta, S., Pruekthaisong, P., Nakajima, H., and Songsiriritthikul, P. (2010). Development of surface magneto-optic Kerr effect setup as a part of multi-UHV chamber at the Siam Photon Laboratory. **Thai Journal of Physics, Series 6** (in press).
- Cho, A. Y., and Arthur, J. R. (1975). Molecular beam epitaxy. **Progress in Solid State Chemistry** 10: 157-191.
- Cohen, M. L., and Chelikowsky, J. R. (1988). **Electronic structure and optical properties of semiconductors**. Berlin: Springer.

- Cumpson, P. J., and Seah, M. P. (1997). Elastic scattering corrections in AES and XPS. II. Estimating attenuation lengths and conditions required for their valid use in overlayer/substrate experiments. **Surf. Interface Anal.** 25: 430-446.
- Daalderop, G. H. O., Kelly, P. J., and Schuurmans, M. F. H. (1994). Magnetic anisotropy of a free-standing Co monolayer and of multilayers which contain Co monolayers. **Phys. Rev. B** 50(14): 9989-10003.
- Davidson, E. R. (1983). **Methods in computational molecular physics**. In G. H. F. Diercksen and S. Wilson (eds.). **NATO Advanced study institute, Series C: Mathematical and physics science** (Vol. 113, 95). New York: Plenum.
- Davis, L. E., MacDonald, N. C., Palmberg, P. W., Riach, G. E., and Weber, R. E. (1996). **Handbook of Auger Electron Spectroscopy**. Physical Electronics.
- Dempsey, D. G., and Kleinman, L. (1977). Surface properties and the photoelectron spin polarization of nickel. **Phys. Rev. Lett.** 39(20): 1297-1300.
- Dietz, E., Becker, H., and Gerhardt, U. (1975). Momentum distribution of photoelectrons emitted from Cu and Ag single crystals, and its polarization dependence. **Phys. Rev. B** 12(6): 2084-2096.
- Dietz, E., Gerhardt, U., and Maetz, C. J. (1978). Exchange splitting in nickel. **Phys. Rev. Lett.** 40(13): 892-896.
- Donath, M., Glöbl, M., Senftinger, B., and Dose, V. (1986). Photon polarization effects in inverse photoemission from Cu(001). **Solid State Commun.** 60(3): 237-240.
- Dose, V., Altmann, W., Goldmann, A., Kolac, U., and Rogozik, J. (1984). Image-potential states observed by inverse photoemission. **Phys. Rev. Lett.** 52(21): 1919-1921.

- Eastman, D. E., Himpsel, F. J., and Knapp, J. A. (1978). Experimental band structure and temperature-dependent magnetic exchange splitting of nickel using angle-resolved photoemission. **Phys. Rev. Lett.** 40(23): 1514-1517.
- Eberhardt, W., and Plummer, E. W. (1980). Angle-resolved photoemission determination of the band structure and multielectron excitations in Ni. **Phys. Rev. B** 21(8): 3245-3255.
- Elsholz, F., and Schöll, E. (2004). Control of surface roughness in amorphous thin-film growth. **Appl. Phys. Lett.** 84(21): 4167-4169.
- Engel, B. N., England, C. D., Van Leeuwen, R. A., Wiedmann, M. H., and Falco, C. M. (1991). Interface magnetic anisotropy in epitaxial superlattices. **Phys. Rev. Lett.** 67(14): 1910-1913.
- Erskine, J. L. (1980). Surface states and the photoelectron-spin polarization of Ni(100). **Phys. Rev. Lett.** 45(17): 1446-1449.
- Falicov, L. M., Victora, R. H., and Tersoff, J. (1985). **The structure of surfaces.** Berlin: Springer.
- Farle, M., Mirwald-Schulz, B., Anisimov, A. N., Platow, W., and Baberschke, K. (1997a). Higher-order magnetic anisotropies and the nature of the spin-reorientation transition in face-centered-tetragonal Ni(001)/Cu(001). **Phys. Rev. B** 55(6): 3708-3715.
- Farle, M., Platow, W., Anisimov, A. N., Pouloupoulos, P., and Baberschke, K. (1997b). Anomalous reorientation phase transition of the magnetization in fct Ni/Cu(001). **Phys. Rev. B** 56(9): 5100-5103.

- Feder, R., Alvarado, S. F., Tamura, E., and Kisker, E. (1983). Surface magnetic structure analysis of Ni(001) by polarized electron diffraction. **Surf. Sci.** 127(1): 83-107.
- Feibelman, P. J., and Eastman, D. E. (1974). Photoemission spectroscopy- Correspondence between quantum theory and experimental phenomenology. **Phys. Rev. B** 10(12): 4932-4947.
- Feynman, R. P. (1939). Forces in molecules. **Phys. Rev.** 56(4): 340-343.
- Freeman, A. J., and Wu, R. Q. (1991). Electronic structure theory of surface, interface and thin-film magnetism. **J. Magn. Magn. Mater.** 100(1-3): 497-514.
- Fu, C. L., Freeman, A. J., and Oguchi, T. (1985). Prediction of strongly enhanced two-dimensional ferromagnetic moments on metallic overlayers, interfaces, and superlattices. **Phys. Rev. Lett.** 54(25): 2700-2703.
- Fulghum, J. E., Stokell, R., McGuire, G., Patnaik, B., Yu, N., Zhao, Y. J., and Parikh, N. (1992). Determination of Si2p electron attenuation lengths in SiO<sub>2</sub>. **J. Electron Spectrosc. Relat. Phenom.** 60(2): 117-125.
- Gradmann, U., Korecki, J. and Waller, G. (1986). In-plane magnetic surface anisotropies in Fe(110). **Appl. Phys. A** 39(2): 101-108.
- Grass, M., Braun, J., Borstel, G., Schneider, R., Dürr, H., Fauster, Th., and Dose, V. (1993). Unoccupied electronic states and surface barriers at Cu surfaces. **J. Phys.: Condens. Matter** 5(5): 599-614.
- Hamann, D. R., Schlüter, M., and Chiang, C. (1979). Norm-conserving pseudopotentials. **Phys. Rev. Lett.** 43(20): 1494-1497.
- Heine, V. (1970). The concept of pseudopotentials. **Solid State Phys.** 24: 1-36.

- Henk, J., Niklasson, A. M. N., and Johansson, B. (1999). Magnetism and anisotropy of ultrathin Ni films on Cu(001). **Phys. Rev. B** 59(14): 9332-9341.
- Hermanson, J. (1977). Final-state symmetry and polarization effects in angle-resolved photoemission spectroscopy. **Solid State Commun.** 22: 9-11.
- Hertz, H. (1887). Photoelectric effect. **Ann. Physik** 31: 983-1000.
- Himpsel, F. J., Knapp, J. A., and Eastman, D. E. (1979). Experimental energy-band dispersions and exchange splitting for Ni. **Phys. Rev. B** 19(6): 2919-2927.
- Hjortstam, O., and Trygg, J. (1996). Calculated spin and orbital moments in the surfaces of the 3d metals Fe, Co, and Ni and their overlayers on Cu(001). **Phys. Rev. B** 53(14): 9204-9213.
- Hjortstam, O., Baberschke, K., Wills, J. M., Johansson, B., and Eriksson, O. (1997). Magnetic anisotropy and magnetostriction in tetragonal and cubic Ni. **Phys. Rev. B** 55(22): 15026-15032.
- Hohenberg, P., and Kohn, W. (1964). Inhomogeneous electron gas. **Phys. Rev.** 136(3B): 864-871.
- Holzwarth, N. A. W., Matthews, G. E., Tackett, A. R., and Dunning, R. B. (1997). Comparison of the projector augmented-wave, pseudopotential, and linearized augmented-plane-wave formalisms for density-functional calculations of solids. **Phys. Rev. B** 55(4): 2005-2017.
- Hong, J., Wu, R. Q., Lindner, J., Kosubek, E., and Baberschke, K. (2004). Manipulation of spin reorientation transition by oxygen surfactant growth: A combined theoretical and experimental approach. **Phys. Rev. Lett.** 92(14): 147202-147205.

- Huang, F., Kief, M. T., Mankey, G. J., and Willis, R. F. (1994). Magnetism in the few-monolayers limit: A surface magneto-optic Kerr-effect study of the magnetic behavior of ultrathin films of Co, Ni, and Co-Ni alloys on Cu(100) and Cu(111). **Phys. Rev. B** 49(6): 3962-3971.
- Hubbard, J. (1963). Electron correlations in narrow energy bands. **Proc. Roy. Soc. A** 276(26): 238-257.
- Hüfner, S. (1995). **Photoelectron spectroscopy** (2<sup>nd</sup> ed). Berlin : Springer-verlag.
- Ichimiya, A., and Cohen, P. (2004). **Reflection high energy electron diffraction**. Cambridge: Cambridge University Press.
- Johnson, D. D. (1988). Modified Broyden's method for accelerating convergence in self-consistent calculations. **Phys. Rev. B** 38(18): 12807-12813.
- Johnson, M. T., Bloemen, P. J. H., den Broeder F. J. A, and de Vries J. J. (1996). Magnetic anisotropy in metallic multilayers. **Rep. Prog. Phys.** 59(11): 1409-1458.
- Kevan, S. D. (1983). Observation of a new surface state on Cu(001). **Phys. Rev. B** 28(4): 2268-2270.
- Kittel, C. (1976). **Introduction to solid state physics**. New York: Wiley.
- Kohn, W., and Sham, L. J. (1965). Self-consistent equations including exchange and correlation effects. **Phys. Rev.** 140(4A): 1133-1138.
- Kohn, W., and Rostoker, N. (1954). Solution of the Schrödinger equation in periodic lattices with an application to metallic lithium. **Phys. Rev.** 94(5): 1111-1120.
- Kresse, G., and Furthmüller, J. (1996a). Efficiency of *ab-initio* total energy calculations for metals and semiconductors using a plane-wave basis set. **Comp. Mater. Sci.** 6: 15-50.

- Kresse, G., and Furthmüller, J. (1996b). Efficient iterative schemes for *ab initio* total-energy calculations using a plane-wave basis set. **Phys. Rev. B** 54(16): 11169-11186.
- Kresse, G., and Hafner, J. (1993). *Ab initio* molecular dynamics for open-shell transition metals. **Phys. Rev. B** 48(17): 13115-13118.
- Kresse, G., and Hafner, J. (1994). *Ab initio* molecular-dynamics simulation of the liquid-metal-amorphous-semiconductor transition in germanium. **Phys. Rev. B** 49(20): 14251-14269.
- Kresse, G., and Joubert, D. (1999). From ultrasoft pseudopotentials to the projector augmented-wave method. **Phys. Rev. B** 59(3): 1758-1775.
- Kübler, J., and Eyert, V. (1992). **Electronic and magnetic properties of metals and ceramics**. In K. H. J. Buschow (eds.). Weinheim: VCH-Verlag.
- Laasonen, K., Pasquarello, A., Car, R., Lee, C., and Vanderbilt, D. (1993). Car-Parrinello molecular dynamics with Vanderbilt ultrasoft pseudopotentials. **Phys. Rev. B** 47(16): 10142-10153.
- Lange, C., Mandel, T., Laubschacht, C., and Kaindl, G. (1990). Inverse photoemission study of copper at variable photon energy. **J. Electron Spectrosc. Relat. Phenom.** 52: 49-60.
- Liu, B. (1978). **Numerical algorithms in chemistry: Algebraic methods**. In C. Moler and I. Scavitt (eds.). In **Report on Workshop** (49). University of California: Berkley.
- MacLaren, J. M., and Victora, R. H. (1994). Theoretical predictions of interface anisotropy in the presence of interdiffusion. **J. Appl. Phys.** 76(10): 6069-6074.

- Mahan, G. D. (1970). Theory of photoemission in simple metals. **Phys. Rev. B** 2(11): 4334-4350.
- Mahan, G. D. (1981). **Many-particle Physics**. New York: Plenum.
- Manning, M. F., and Chodorow, M. I. (1939). Electronic energy bands in metallic tungsten. **Phys. Rev.** 56(8): 787-798.
- Martin, R. M. (2004). **Electronic structure: Basic theory and practical methods**. United Kingdom: Cambridge University Press.
- Monkhorst, H. J., and Pack, J. D. (1978). Comment on special points for Brillouin-zone integrations. **Phys. Rev. B** 18(10): 5897-5899.
- Mulhollan, G. A., et al. (1988). Spin-polarized LEED investigation of the magnetized Ni(111) surface. **Surf. Sci.** 204(3): 503-516.
- Müller, S., Schulz, B., Kostka, G., Farle, M., Heinz, K., and Baberschke, K. (1996). Pseudomorphic growth of Ni films on Cu(001): a quantitative LEED analysis. **Surf. Sci.** 364(3): 235-241.
- Nakajima, H., Buddhakala, M., Chumpolkulwong, S., Supruangnet, R., Kakizaki, A., and Songsiriritthigul, P. (2007). Performance of the BL4 beamline for surface and interface research at the Siam Photon Laboratory. In **Proceeding of the Ninth International Conference of Synchrotron Radiation Instrumentation** (Vol. 879, 543). New York: American Institute of Physics.
- Néel, L. (1954). Anisotropie magnétique superficielle et surstructures d'orientation. **J. Phys. Radium** 15(4): 225-239.
- Ney, A., Lenz, K., Pouloupoulos, P., and Baberschke, K. (2002). Absolute magnetometry on ultrathin 3d-metal films by UHV-SQUID. **J. Magn. Magn. Mater.** 240(1-3): 343-345.

- Noffke, J., Brunn, W., and Hermann, K. (1978). The extended rigorous cellular method: Theory and applications to thin films. **Z. Phys. B: Condens. Matter** 29(4): 353-360.
- O'Brien, W. L., Droubay, T., and Tonner, B. P. (1996). Transitions in the direction of magnetism in Ni/Cu(001) ultrathin films and the effects of capping layers. **Phys. Rev. B** 54(13): 9297-9303.
- Oura, K., Lifshits, V. G., Saranin, A. A., Zotov, A. V., and Katayama, M. (2003). **Surface science: An introduction** (1-45). Berlin Heidelberg: Springer-Verlag.
- Pampuch, C., Rader, O., Kläsger, R., and Carbone, C. (2001). Evolution of the electronic structure in epitaxial Co, Ni, and Cu films. **Phys. Rev. B** 63(15): 153409-153412.
- Parr, G. R., and Yang, W. (1989). **Density-functional theory of atoms and molecules**. The United States of America: Oxford University Press.
- Pendry, J. B. (1976). Theory of photoemission. **Surf. Sci.** 57(2): 679-705.
- Perdew, J. P., and Wang, Y. (1992). Accurate and simple analytic representation of the electron-gas correlation energy. **Phys. Rev. B** 45(23): 13244-13249.
- Perdew, J. P., Burke, K., and Ernzerhof, M. (1996). Generalized gradient approximation made simple. **Phys. Rev. Lett.** 77(18): 3865-3868.
- Phillips, J. C. (1958). Energy-band interpolation scheme based on a pseudopotential. **Phys. Rev.** 112(3): 685-695.
- Phillips, J. C., and Kleinman, L. (1959). New method for calculation wave functions in crystals and molecules. **Phys. Rev.** 116(2): 287-294.
- Pick, Š., and Dreysse, H. (1992). Monolayer magnetic anisotropy: A systematic tight-binding study. **Phys. Rev. B** 46(9): 5802-5805.

- Platow, W., Bovensiepen, U., Pouloupoulos, P., Farle, M., and Baberschke, K. (1999). Structure of ultrathin Ni/Cu(001) films as a function of film thickness, temperature, and magnetic order. **Phys. Rev. B** 59(19): 12641-12646.
- Ploog, K. (1988). Microscopical structuring of solids by molecular beam epitaxy. **Angewandte Chemie International Edition in English** 27(5): 593-621.
- Plummer, E. W., and Eberhardt, W. (1979). Magnetic surface states on Ni(100). **Phys. Rev. B** 20(4): 1444-1453.
- Powell, C. J. (1985). The energy dependence of electron attenuation lengths. **Surf. Interface Anal.** 7(6): 256-262.
- Pulay, P. (1980). Convergence acceleration of iterative sequences, the case of scf iteration. **Chem. Phys. Lett.** 73(2): 393-398.
- Qiu, Z. Q., and Bader, S. D. (1999). Symmetry breaking at magnetic surfaces and interfaces. **Surf. Sci.** 438(1-3): 319-328.
- Qiu, Z. Q., and Bader, S. D. (2000). Surface Magneto-Optic Kerr Effect. **Rev. Sci. Instrum.** 71(3): 1243-1255.
- Rader, O., Wolf, H., Gudat, W., Tadich, A., Broekman, L., Huwald, E., Leckey, R. C. G., Riley, J. D., Shikin, A. M., Matsui, F., Miyata, H., and Daimon, H. (2009). Apparent “three-dimensional” Fermi surface of transition-metal monolayers. **Phys. Rev. B** 79(24): 245104-1-6.
- Rado, G. T. (1982). Theory of ferromagnetic resonance and static magnetization in ultrathin crystals. **Phys. Rev. B** 26(1): 295-304.
- Saffren, M. M., and Slater, J. C. (1953). An augmented plane-wave method for the periodic potential problem. II. **Phys. Rev.** 92(5): 1126-1128.

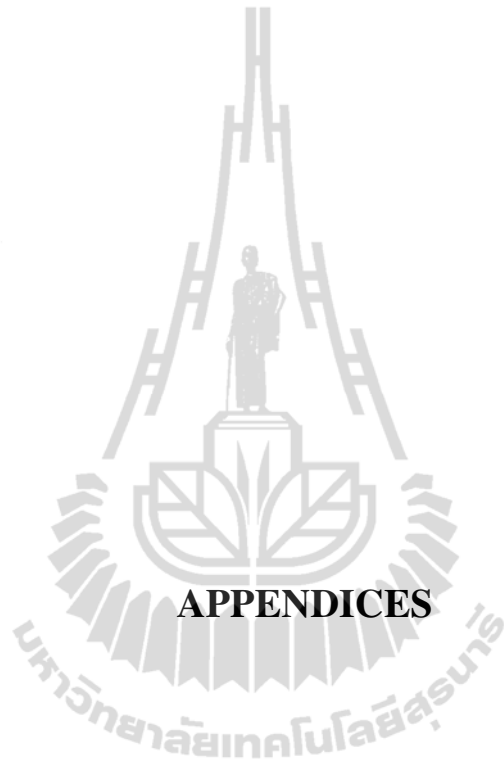
- Sander, D. (1999). The correlation between mechanical stress and magnetic anisotropy in ultrathin films. **Rep. Prog. Phys.** 62(5): 809.
- Schattke, W., and Van Hove, M. A. (2003). **Solid-state photoemission and related methods.** Germany: Wiley-Vch.
- Schneider, R., Dürr, H., Fauster, Th., and Dose, V. (1990). Temperature dependence of the inverse photoemission from copper surfaces. **Phys. Rev. B** 42(3): 1638-1651.
- Schulz, B., and Baberschke, K. (1994). Crossover from in-plane to perpendicular magnetization in ultrathin Ni/Cu(001) films. **Phys. Rev. B** 50(18): 13467-13471.
- Schulz, B., Schwarzwald, R., and Baberschke, K. (1994). Magnetic properties of ultrathin Ni/Cu(100) films determined by a UHV-FMR study. **Surf. Sci.** 307: 1102-1108.
- Segall, B. (1962). Fermi surface and energy bands of copper. **Phys. Rev.** 125(1): 109-122.
- Shen, J., Giergiel, J., and Kirschner, J. (1995). Growth and morphology of Ni/Cu(100) ultrathin films: An *in situ* study using scanning tunneling microscopy. **Phys. Rev. B** 52(11): 8454-8460.
- Singh, D. J., and Nordström L. (1994). **Planewaves, Pseudopotentials and the LAPW method** (2<sup>nd</sup> ed). United State of America: Spring Science+Business Media.
- Slater, J. C. (1937). Wave functions in a periodic potential. **Phys. Rev.** 51(10): 846-851.

- Slater, J. C. (1974). **The self-consistent field for molecules and solids** (Vol. 4). The United State of America: McGraw-Hill.
- Song, O., Ballentine, C. A., and O'Handley, R. C. (1994). Giant surface magnetostriction in polycrystalline Ni and NiFe films. **Appl. Phys. Lett.** 64(19): 2593-2595.
- Steinmann, W. (1989). Spectroscopy of image-potential states by two-photon photoemission. **Appl. Phys. A** 49(4): 365-377.
- Strocov, V. N., Claessen, R., Nicolay, G., Hüfner, S., Kimura, A., Harasawa, A., Shin, S., Kakizaki, A., Nilsson, P. O., Starnberg, H. I., and Blaha, P. (1998). Absolute band mapping by combined angle-dependent very-low-energy electron diffraction and photoemission: Application to Cu. **Phys. Rev. Lett.** 81(22): 4943-4946.
- Strocov, V. N., Starnberg, H., and Nilsson, P. O. (1997). Excited-state bands of Cu determined by VLEED band fitting and their implications for photoemission. **Phys. Rev. B** 56(4): 1717-1725.
- Tamura, E., Feder, R., Waller, G., and Gradmann, U. (1990). Determination of the surface magnetization of Fe(110) by spin-polarized low-energy electron diffraction. **Phys. Stat. Sol. (b)** 157(2): 627-633.
- Tanuma, S., Powell, C. J., and Penn, D. R. (1988). Calculation of electron inelastic mean free paths for 31 materials. **Surf. Interface Anal.** 11: 577-589.
- Tersoff, J., and Falicov, L. M. (1982). Magnetic and electronic properties of Ni films, surfaces, and interfaces. **Phys. Rev. B** 26(11): 6186-6200.
- Teter, M. P., Payne, M. C., and Allan, D. C. (1989). Solution of Schrödinger's equation for large systems. **Phys. Rev. B** 40(18): 12255-12263.

- Thermo Electron Corporation (2004). Alpha 110 Hemispherical electron energy analyzer. **AN30054\_E**.
- Thompson, M. A., and Erskine, J. L. (1985). Electronic properties of  $p(1 \times 1)$  Ni films on Cu(100). **Phys. Rev. B** 31(10): 6832-6835.
- Uiberacker, C., Zablouil, J., Weinberger, P., Szunyogh, L., and Sommers, C. (1999). Lattice relaxation driven reorientation transition in Ni/Cu(100). **Phys. Rev. Lett.** 82(6): 1289-1292.
- van Dijken, S., Vollmer, R., Poelsema, B., and Kirschner, J. (2000). The influence of CO and H<sub>2</sub> adsorption on the spin reorientation transition in Ni/Cu(001). **J. Magn. Magn. Mater.** 210(1-3): 316-328.
- Vanderbilt, D. (1990). Soft self-consistent pseudopotentials in a generalized eigenvalue formalism. **Phys. Rev. B** 41(11): 7892-7895.
- Vijayakumar, M., and Gopinathan, M. S. (1996). Spin-orbit coupling constants of transition metal atoms and ions in density functional theory. **J. Mol. Struct. (Theochem)** 361: 15-19.
- Voigt, W. (1915). **Handbook der Electricität und des Magnetismus**. Leipzig: Barth.
- Vollmer, R., Gutjahr-Löser, Th., Kirschner, J., van Dijken, S., and Poelsema, B. (1999). Spin-reorientation transition in Ni films on Cu(001): The influence of H<sub>2</sub> adsorption. **Phys. Rev. B** 60(9): 6277-6280.
- Vosko, S. H., Wilk, L., and Nusair, M. (1980). Accurate spin-dependent electron liquid correlation energies for local spin density calculations: a critical analysis. **Can. J. Phys.** 58(8): 1200-1211.

- Wagner, K., Weber, N., Elmers, H. J., and Gradmann, U. (1997). Magnetization of free Fe(110) surfaces from thin film magnetometry. **J. Magn. Magn. Mater.** 167(1-2): 21-26.
- Wang, C. S., and Callaway, J. (1974). Band structure of nickel: Spin-orbit coupling, the Fermi surface, and the optical conductivity. **Phys. Rev. B** 9(11): 4897-4907.
- Wegehaupt, T., Rieger, D., and Steinmann, W. (1988). Observation of empty bulk states on Cu(100) by two-photon photoemission. **Phys. Rev. B** 37(17): 10086-10089.
- Weinert, M., and Blügel, S. (1993). **Magnetic multilayers**. Singapore: World Scientific.
- Weling, F., and Callaway, J. (1982). Semiempirical description of energy bands in nickel. **Phys. Rev. B** 26(2): 710-719.
- Werner, W. S. M. (2004). Towards a universal curve for electron attenuation: Elastic scattering data for 45 elements. **Surf. Interface Anal.** 18(3): 217-228.
- Western Digital Technologies. (2006). **Perpendicular Magnetic Recording (PMR)** [On-line]. Available: <http://www.wdc.com/wdproducts/library/other/2579-701185.pdf>.
- Willhelm, F., Bovensiepen, U., Scherz, A., Pouloupoulos, P., Ney, A., Wende, H., Ceballos, G., and Baberschke, K. (2000). Manipulation of the Curie temperature and the magnetic moments of ultrathin Ni and Co films by Cu-capping. **J. Magn. Magn. Mater.** 222(1-2): 163-167.
- Wohlfarth, E. P. (1953). The theoretical and experimental status of the collective electron theory of ferromagnetism. **Rev. Mod. Phys.** 25(1): 211-219.

- Wood, D. M., and Zunger, A. (1985). A new method for diagonalising large matrices. **J. Phys. A** 18(9): 1343.
- Woodruff, D. P., Hulbert, S. L., and Johnson, P. D. (1985). Unoccupied surface resonance on Cu(100) and the effect of vacuum-level pinning. **Phys. Rev. B** 31(6): 4046-4048.
- Wu, F. M., Lu, H. J., Fang, Y. Z., and Huang, S. H. (2008). Coverage dependence of growth mode in heteroepitaxy of Ni on Cu(100) surface. **Common. Theor. Phys.** 50(1): 231-236.
- Wuttig, M., and Liu, X. (2004). **Ultrathin metal films: Magnetic and structural properties**. Germany: Springer.
- Zettili, N. **Quantum mechanics: Concepts and applications**. Chichester: John Wiley & Sons.
- Zhu, J. G., Zheng, Y., and Prinz, G. A. (2000). Ultrahigh density vertical magnetoresistive random access memory. **J. Appl. Phys.** 87(9): 6668-6673.
- Zhu, X.-Y., Hermanson, J., Arlinghaus, F. J., Gay, J. G., Richter, R., and Smith, J. R. (1984). Electronic structure and magnetism of Ni(100) films: Self-consistent local-orbital calculations. **Phys. Rev. B** 29(8): 4426-4438.



## APPENDIX A

### SPHERICAL HARMONICS FOR $s$ , $p$ , AND $d$ ORBITALS

Spherical harmonics  $Y_{l,m}(\theta, \varphi) = |l, m\rangle$  are eigenfunctions of the non-relativistic Hamiltonian describing an electron in a spherical symmetric potential, i.e. the hydrogen atom. The explicit representation of the spherical harmonics and their expressions in Cartesian coordinates is given in Table A.1 and the atomic orbitals with a basis set of the spherical harmonics in a cubic potential as shown in Table A.2.

**Table A.1** Spherical harmonics and their expressions in Cartesian coordinates (Zettili, 2001).

| $Y_{l,m}(\theta, \varphi)$   | $Y_{l,m}(x, y, z)$  |
|--|---|
| $Y_{0,0}(\theta, \varphi) = \frac{1}{\sqrt{4\pi}}$   | $Y_{0,0}(x, y, z) = \frac{1}{\sqrt{4\pi}}$                                    |
| $Y_{1,0}(\theta, \varphi) = \sqrt{\frac{3}{4\pi}} \cos \theta$                                       | $Y_{1,0}(x, y, z) = \sqrt{\frac{3}{4\pi}} \frac{z}{r}$                        |
| $Y_{1,\pm 1}(\theta, \varphi) = \mp \sqrt{\frac{3}{8\pi}} e^{\pm i\varphi} \sin \theta$              | $Y_{1,\pm 1}(x, y, z) = \mp \sqrt{\frac{3}{8\pi}} \frac{x \pm iy}{r}$         |
| $Y_{2,0}(\theta, \varphi) = \sqrt{\frac{5}{16\pi}} (3 \cos^2 \theta - 1)$                            | $Y_{2,0}(x, y, z) = \sqrt{\frac{5}{16\pi}} \frac{3z^2 - r^2}{r^2}$            |
| $Y_{2,\pm 1}(\theta, \varphi) = \mp \sqrt{\frac{15}{8\pi}} e^{\pm i\varphi} \sin \theta \cos \theta$ | $Y_{2,\pm 1}(x, y, z) = \mp \sqrt{\frac{15}{8\pi}} \frac{(x \pm iy)z}{r^2}$   |
| $Y_{2,\pm 2}(\theta, \varphi) = \sqrt{\frac{15}{32\pi}} e^{\pm 2i\varphi} \sin^2 \theta$             | $Y_{2,\pm 2}(x, y, z) = \mp \sqrt{\frac{15}{32\pi}} \frac{(x \pm iy)^2}{r^2}$ |

**Table A.2** Linear combinations of the spherical harmonics for  $s$ ,  $p$ , and  $d$  orbitals in cubic potential. The charge density in the angular wave functions form is plotted in the last column. The positive (negative) sign of the wave function is represented by the black (white) color (Zettili, 2001).

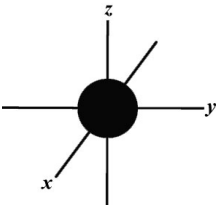
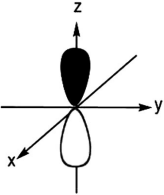
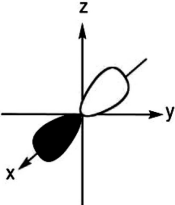
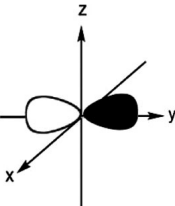
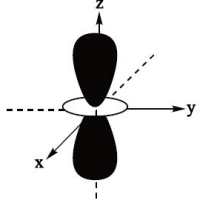
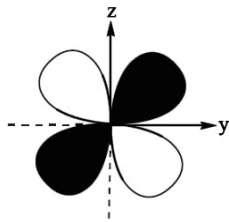
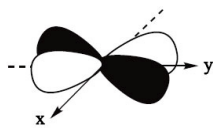
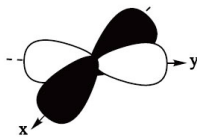
|           |  |   |
|-----------|--|---|
| $s$       | $\frac{1}{\sqrt{4\pi}} = Y_{0,0}$  |    |
| $p_z$     | $\sqrt{\frac{3}{4\pi}} \frac{z}{r} = Y_{1,0}$                                |   |
| $p_x$     | $\sqrt{\frac{3}{4\pi}} \frac{x}{r} = \frac{1}{\sqrt{2}}(Y_{1,-1} - Y_{1,1})$ |  |
| $p_y$     | $\sqrt{\frac{3}{4\pi}} \frac{y}{r} = \frac{i}{\sqrt{2}}(Y_{1,-1} + Y_{1,1})$ |  |
| $d_{z^2}$ | $\sqrt{\frac{5}{16\pi}} \frac{3z^2 - r^2}{r^2} = Y_{2,0}$                    |  |

Table A.2 (Continued).

|               |   |   |
|---------------|---|---|
| $d_{xz}$      | $\sqrt{\frac{15}{4\pi}} \frac{xz}{r^2} = \frac{1}{\sqrt{2}} (Y_{2,-1} - Y_{2,1})$         |    |
| $d_{yz}$      | $\sqrt{\frac{15}{4\pi}} \frac{yz}{r^2} = \frac{i}{\sqrt{2}} (Y_{2,-1} + Y_{2,1})$         |    |
| $d_{xy}$      | $\sqrt{\frac{15}{4\pi}} \frac{xy}{r^2} = \frac{i}{\sqrt{2}} (Y_{2,-2} - Y_{2,2})$         |   |
| $d_{x^2-y^2}$ | $\sqrt{\frac{15}{16\pi}} \frac{x^2 - y^2}{r^2} = \frac{1}{\sqrt{2}} (Y_{2,-2} + Y_{2,2})$ |  |

## APPENDIX B

### SPIN-ORBIT INTERACTION

Dirac theory provided a quantum mechanical description of electrons in an electromagnetic field with invariance under a Lorentz transformation, consistent with the theory of special relativity. As a consequence of the relativistic requirement, a practical form of Dirac's equation for a negative electron charge is written in the following form

$$\left\{ \begin{array}{l} \frac{(-i\hbar\nabla + eA)^2}{2m_e} - e\phi - \frac{(-i\hbar\nabla)^4}{8m_e^3c^2} + \frac{e\hbar}{2m_e}(\vec{B} \cdot \vec{\sigma}) \\ + \frac{e\hbar}{4m_e^2c^2}\vec{\sigma} \cdot [\vec{E} \times (-i\hbar\nabla)] - \frac{e\hbar^2}{4m_e^2c^2}\vec{E} \cdot \nabla \end{array} \right\} \psi = E'\psi. \quad (\text{B.1})$$

The following equation leads to the spin-orbit interaction based on the Thomas correction factor with  $(e\hbar/4m_e^2c^2)\vec{\sigma} \cdot [\vec{E} \times (-i\hbar\nabla)]$  term. According to the application of relativistic transformation to Maxwell's equation, the second term arises from electron motion in the presence of an electric field. The interaction of the electron's magnetic moment  $\vec{\mu}_s$  with the orbital magnetic field  $\vec{B}$  of the nucleus gives rise to the following interaction energy

$$H_{so} = \frac{e}{m_e c} \vec{S} \cdot \vec{B} \quad (\text{B.2})$$

Since, the magnetic field originated by the electron moving at  $\vec{v}$  in a circular orbit around the proton is

$$\vec{B} = \frac{1}{m_e c} \vec{E} \times \vec{p} \quad (\text{B.3})$$

However, the electric field of and electron moves in the Coulomb potential of a nucleus  $V(r) = -e\phi(r)$ , is obtained by

$$\vec{E}(r) = -\vec{\nabla}\phi(r) = \frac{1}{e} \vec{\nabla}V(r) = \frac{1}{e} \frac{\vec{r}}{r} \frac{dV}{dr}. \quad (\text{B.4})$$

So, the magnetic field of the nucleus is obtained by inserting Eq. (B.4) into Eq. (B.3)

$$\vec{B} = \frac{1}{m_e c} \vec{p} \times \frac{1}{e} \frac{\vec{r}}{r} \frac{dV}{dr} = \frac{1}{em_e c r} \frac{dV}{dr} (\vec{p} \times \vec{r}) = \frac{1}{em_e c r} \frac{dV}{dr} \vec{L} \quad (\text{B.5})$$

Therefore, the spin-orbit interaction term in hydrogen's electron;  $V(r) = -e^2 / r$  can be written in the form

$$H_{so} = \frac{e}{m_e c} \vec{S} \cdot \frac{1}{em_e c r} \frac{dV}{dr} \vec{L} = \frac{e^2}{m_e^2 c^2 r^3} \vec{L} \cdot \vec{S} \quad (\text{B.6})$$

The relativistic effect in hydrogen leads to a reduction of the interaction energy in Eq. (B.6) by a factor of 2:

$$H_{so} = \frac{e^2}{2m_e^2 c^2 r^3} \vec{L} \cdot \vec{S} = \xi \vec{L} \cdot \vec{S}, \quad (\text{B.7})$$

where  $\xi$  is the spin-orbit coupling constant. Now, for hydrogen atom the Hamiltonian can be written as

$$H = \frac{\vec{p}^2}{2m_e} - \frac{e^2}{r} + \frac{e^2}{2m_e^2 c^2 r^3} \vec{L} \cdot \vec{S} = H_0 + H_{so}, \quad (\text{B.8})$$

where  $H_0$  is the unperturbed Hamiltonian. As the effects of spin-orbit coupling are to be small, one can use the perturbation theory to find the corrections to the energy

eigenvalues due to  $H_{so}$ . It is require the degenerate eigenstates of  $H_0$  as some linear combinations such that they are also eigenstates of  $H_{so}$  as

$$\vec{L} \cdot \vec{S} = (J^2 - L^2 - S^2) / 2. \quad (\text{B.9})$$

So we write the angular part of the eigenstates of  $H_0$  as the eigenstates  $|n, l, j, m\rangle$  of the operators  $\{L^2, S^2, J^2, J_z\}$ .

Then, the eigenvalues of  $H_{so}$  are given by

$$\Delta E_{nlj} = \frac{e^2 \hbar^2}{4m_e^2 c^2} \left( \int_0^\infty |R_{nl}(r)|^2 \frac{1}{r} dr \right) \left[ j(j+1) - l(l+1) - \frac{3}{4} \right], \quad (\text{B.10})$$

where  $R_{nl}$  are the radial parts of the corresponding energy eigenfunctions of  $H_0$ . The calculated values of spin-orbit coupling constants and radial moments,  $\langle r^n \rangle$ , can be used to compute spin-orbit splitting in molecules.

The spin-orbit coupling constants calculated by an orbital-based DFT method with exchange and correlation functionals derived from *ab-initio* for various orbitals of Ni and Cu atoms is shown in Table B.1. Here, the  $\xi_{nl}$  values are calculated by using the expression

$$\xi_{nl} = \frac{2}{2l+1} (e_{nlj_+} - e_{nlj_-}), \quad (\text{B.11})$$

where  $\xi_{nlj_+}$  and  $\xi_{nlj_-}$  are the eigenvalues expressed in Eq. (B.10) with  $j_+ = l + 1/2$  and  $j_- = l - 1/2$ , respectively.

**Table B.1** Spin-orbit coupling constants for various orbitals of Ni and Cu atoms (in Ry) (Vijayakumar and Gopinathan, 1996).

| Atom | Orbital | DFT    |
|------|---------|--------|
| Ni   | 2p      | 0.8787 |
|      | 3p      | 0.1079 |
|      | 3d      | 0.0092 |
| Cu   | 2p      | 1.0410 |
|      | 3p      | 0.1350 |
|      | 3d      | 0.0109 |



## APPENDIX C

### IRREDUCIBLE REPRESENTATIONS AND CHARACTER

#### TABLES FOR $C_{4v}$

Each point group has a complete set of possible symmetry operations that are conveniently listed as a matrix known as a *Character* table. Those involve the decomposition of reducible representations into their irreducible components. Group theory is an essential tool in the analysis of the symmetry of a molecule, which provides us insight into the orbitals used in bonding. By convention, character tables are displayed with the columns labeled by the classes and the rows by the irreducible representations. In Table C.1 the character tables for  $C_{4v}$  point group is given. Notes about symmetry labels and characters;  $A$  ( $B$ ) means symmetric (anti-symmetric) with regard to rotation about the principal axis for one-dimensional representations.  $E$  for two-dimensional representations, with subscript numbers is used to differentiate symmetry labels. An individual point group is represented by a set of symmetry operations as follows;  $E$  means the identity operation,  $C_n$  represents rotation by  $2\pi/n$  angle,  $\sigma_v$  and  $\sigma_d$  denote vertical and diagonal reflection plane with respect to the principal axis, respectively.

**Table C.1** Character table for  $C_{4v}$  point group (Carter, 1998). A basis function and small representation in BSW and Schoenflies notation in fcc (001) bulk and surfaces in Cartesian coordinate are also shown.

| $C_{4v}$ | E | $2C_4$ | $C_2$ | $2\sigma_v$ | $2\sigma_d$ | Bulk BZ          | $\Delta$    | Surface BZ       | $\bar{\Delta}$    | Compatible<br>to $\Gamma$                                   |
|----------|---|--------|-------|-------------|-------------|------------------|-------------|------------------|-------------------|---|
| $A_1$    | 1 | 1      | 1     | 1           | 1           | $x^2 + y^2, z^2$ | $\Delta_1$  | $x^2 + y^2, z^2$ | $\bar{\Delta}_1$  | $\Gamma_{15}, \Gamma_{12}$                                  |
| $A_2$    | 1 | 1      | 1     | -1          | -1          | $xy(x^2 - y^2)$  | $\Delta'_1$ | $xy(x^2 - y^2)$  | $\bar{\Delta}'_1$ | $\Gamma'_{15}, \Gamma'_{12}$                                |
| $B_1$    | 1 | -1     | 1     | 1           | -1          | $x^2 - y^2$      | $\Delta_2$  | $xy$             | $\bar{\Delta}'_2$ | $\Gamma_{25}, \Gamma_{12}$                                  |
| $B_2$    | 1 | -1     | 1     | -1          | 1           | $xy$             | $\Delta'_2$ | $x^2 - y^2$      | $\bar{\Delta}_2$  | $\Gamma'_{25}, \Gamma'_{12}$                                |
| $E$      | 2 | 0      | -2    | 0           | 0           | $(xz, yz)$       | $\Delta_5$  | $(xz, yz)$       | $\bar{\Delta}_5$  | $\Gamma_{15}, \Gamma'_{15},$<br>$\Gamma_{25}, \Gamma'_{25}$ |

## APPENDIX D

### PUBLICATIONS AND PRESENTATIONS

#### D.1 List of Publications

Meevasana, W., Supruangnet, R., Nakajima, H., Topon, O., Amornkitbamrung, V., and Songsiriritthigul, P. (2009). Electron affinity study of admantane on Si(111). **Appl. Surf. Sci.** 256: 934-936.

Supruangnet, R., Nakajima, H., Chai-Ngam, R., Songsiriritthigul, P., and Kakizaki, A. (2011). Electronic structure and magnetic anisotropy in Ni/Cu(001) from angle-resolved photoemission spectroscopy. **J. Phys. Soc. Jpn.** 80: 064706-064710.

#### D.2 List of Presentations (poster)

Meevasana, W., Supruangnet, R., Nakajima, H., and Songsiriritthigul, P. (2008). Study of admantane on Si(111) as a potential electron emitter. In **Siam Physics Congress 2008**. Nakorn Ratchasima: Thai Physics Society.

Supruangnet, R., Nakajima, H., Chai-ngam, R., and Songsiriritthigul, P. (2009). Angle-resolved photoemission spectroscopy in ultra-thin Ni film on Cu(001). In **Siam Physics Congress 2009**. Phetchburi: Thai Physics Society.

Supruangnet, R., Nakajima, H., and Songsiriritthigul, P. (2011). First-principles calculation of magnetic anisotropy on Ni films. In **Siam Physics Congress 2011**. Chonburi: Thai Physics Society.



## Electron affinity study of adamantane on Si(1 1 1)

W. Meevasana<sup>a,b,\*</sup>, R. Supruangnet<sup>c</sup>, H. Nakajima<sup>a,d</sup>, O. Topon<sup>e</sup>, V. Amornkitbamrung<sup>e</sup>, P. Songsiririthigul<sup>a,c,d</sup>

<sup>a</sup>Synchrotron Light Research Institute, Nakhon Ratchasima 30000, Thailand

<sup>b</sup>Department of Physics, Stanford University, Stanford, CA 94305, USA

<sup>c</sup>School of Physics, Suranaree University of Technology, Nakhon Ratchasima 30000, Thailand

<sup>d</sup>TheP Center, CHE, 328 Si Ayutthaya Rd., Bangkok 10400, Thailand

<sup>e</sup>Department of Physics, Khon Kaen University, Khon Kaen 40002, Thailand

### ARTICLE INFO

Article history:  
Available online 6 June 2009

PACS:  
73.22.-f, 79.60.-i

Keywords:  
Diamondoid  
Adamantane  
Electron affinity  
Photoemission spectroscopy

### ABSTRACT

Recently, tetramantane, a member of diamondoid series ( $C_{4n+6}H_{4n+12}$ ), has shown to exhibit negative-electron-affinity effect which has a potential use for efficient electron emitting devices. Here, we explore the electronic property of adamantane ( $C_{10}H_{16}$ ), the smallest member of the series. We prepare adamantane films on Si(1 1 1) substrates and then study their electronic structure with photoemission spectroscopy. Photoelectron spectra of adamantane on Si(1 1 1) have shown a peak at low-kinetic energy which could be a generic property of diamondoids. The possibility of the negative-electron-affinity effect in adamantane is further discussed.

© 2009 Elsevier B.V. All rights reserved.

### 1. Introduction

Diamondoids, a series of hydrocarbon compounds whose carbon atoms form a diamond-like nanostructure and hydrogen atoms terminate the surface, have attracted attention as recently they can be extracted in a large quantity from petroleum waste [1]. These materials have potential to combine the properties of diamond and nanomaterials. One interesting property is that hydrogen-terminated diamond surfaces have negative electron affinity (NEA), which has the conduction-band minimum higher than the vacuum level [2–4]. NEA materials could find many applications in photodetectors and cold electron emitters. Because diamondoids are essentially fully hydrogen-terminated diamond clusters, they could be good candidates for NEA electron emission material.

From the series of diamondoids, as shown in Fig. 1, adamantane ( $C_{10}H_{16}$ ) is the smallest member consisting of one diamond-structure-like subunit. Larger diamondoids are diamantane ( $C_{14}H_{20}$ ), triamantane ( $C_{18}H_{24}$ ), and poly-mantanes which have the chemical formulae ( $C_{4n+6}H_{4n+12}$ ).

Up to date, only the self-assembled monolayers of tetramantane-6-thiol ( $C_{22}H_{27}-S-H$ ) on gold have been reported to exhibit the NEA effect in the diamondoid series [5]. Here, to search for a

signature of negative-electron-affinity effect in another diamondoid member, we study adamantane on Si(1 1 1) surface with photoemission spectroscopy and find that NEA effect may be generic in diamondoids.

### 2. Experiment

We measured photoelectron spectra of adamantane on Si(1 1 1) substrate; the Si(1 1 1) substrate (Nilaco Corp., Japan) was n-type with low resistivity ( $\leq 0.02 \Omega \text{ cm}$ ). The substrate preparation in UHV started by heating the substrate up to 1123 K for 15 min and flashed to 1273 K to remove contamination on the surface. The surface quality of the substrate was then checked by low-electron-energy diffraction (LEED) and photoemission spectroscopy. After the Si(1 1 1) surface was cleaned and later cooled down to temperature  $T = 195 \text{ K}$ , adamantane was evaporated onto the surface at pressure  $= 3 \times 10^{-7} \text{ mbar}$  for 2 min; this evaporation was through a leak valve connecting to the sample cell whose temperature was set to 343 K. Note that before evaporating, the sample cell was warmed up to 323 K and continuously pumped for 1 h to assure the purity of evaporating adamantane.

All angle-integrated photoelectron data of adamantane on Si(1 1 1) were collected on a VG electron energy analyzer (CLAM2) at Beamline 4 of the Siam Photon Laboratory at the Synchrotron Light Research Institute, Thailand. The photon energies were between 55 and 130 eV and the base pressure was  $< 3 \times 10^{-10} \text{ mbar}$ .

\* Corresponding author at: Synchrotron Light Research Institute, Nakhon Ratchasima 30000, Thailand. Tel.: +66 44 217 040.  
E-mail address: worawat@gmail.com (W. Meevasana).

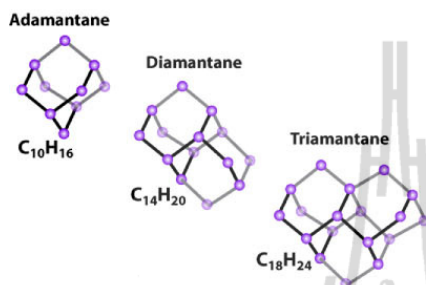


Fig. 1. Atomic structures of the first three members of diamondoids where spheres represent carbon atoms.

### 3. Results and discussion

After cleaning the Si(111) surface by the heating process, we measure low-energy-electron-diffraction pattern and photoelectron spectroscopy to check the surface quality. The low-energy-electron-diffraction pattern shows the  $c(7 \times 7)$  pattern as shown in Fig. 2 and the photoelectron spectrum shows valance band in the binding energy range between 0 and 5 eV as shown in Fig. 3 (top graph). These indicate that the prepared Si(111) surface is reasonably clean.

We then prepare the adamantane films by evaporating adamantane onto the clean Si(111) surface. Photoelectron spectra of valance bands are measured before and after the evaporation, as shown in Fig. 3 (top two graphs). The clear change in the spectral line shape shows that adamantane covers Si(111) surface reasonably well after the evaporation. To have a rough estimate of film thickness, the spectra of adamantane on Si(111) from our measurements are compared with the previous studies [6,7] as shown in Fig. 3; the top two spectra are from our measurements and the two bottom spectra of adamantane films with thickness = 0.3 and 2 monolayers (ML) are from Ref. [6]. When the film is in sub-monolayer in thickness (e.g. 0.3 ML spectrum), the

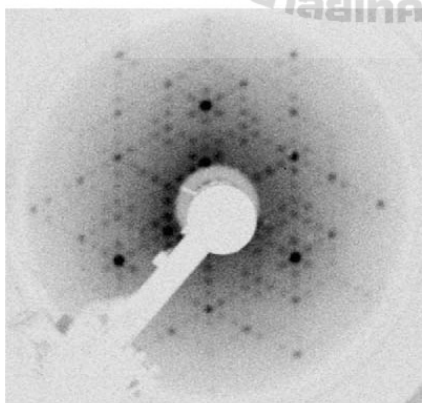


Fig. 2. Low-energy-electron-diffraction pattern showing  $c(7 \times 7)$  surface structure of Si(111).

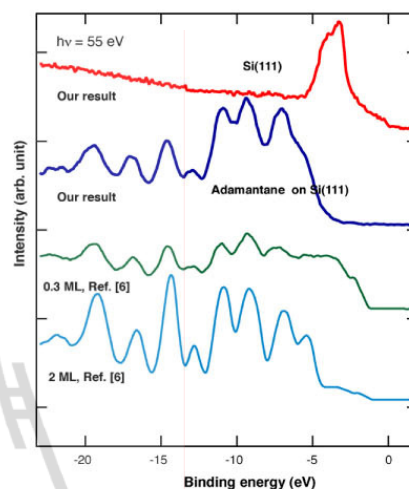


Fig. 3. Photoemission spectra of adamantane on Si(111). The top two spectra are from our measurements of Si(111) alone and adamantane on Si(111) as indicated. The measurements were performed at  $T = 200$  K with photon energy = 55 eV. For a rough comparison, the bottom two spectra of adamantane films with thickness = 0.3 and 2 monolayers (ML) are from Ref. [6].

spectrum will show the intensity distributed from both Si substrate and adamantane. Since the 2 ML spectrum from Ref. [6] and our spectrum show a closer appearance at energy range near Fermi level, where contribution of Si spectral weight would show up otherwise if the Si surface presents, this implies that approximately 2 monolayers of adamantane or in the same order are deposited onto our Si(111) substrate.

To explore the NEA property, we focus on the photoelectron spectra at low-kinetic energy. We note that 9 V bias on the sample is applied to avoid the problem of low-energy cut-off of electron analyzer. We find that there is a low-kinetic-energy-electron peak (shaded area, in Fig. 4(a) and (b)), showing up in the spectrum of adamantane on Si(111) while this peak is not observed with the spectrum of Si(111) alone.

This peak also persists with various photon energies; the spectra of 55 and 130 eV photon energies are shown in Fig. 4(a) and (b) respectively. We note that the strong narrow peak in Si(111) spectrum with 130 eV photon energy is Si 2p energy level. This Si 2p peak is different from the low-kinetic-energy-electron peak since the energy position of Si 2p will change with respect to energy of incident photon.

One possible interpretation of this low-energy peak is a result of negative-electron-affinity effect where the conduction-band minimum is above the vacuum level. This can be illustrated by the schematic photoelectron spectra in Fig. 4(c) in the case that electron affinity (EA) is positive or negative; in the figure,  $E_c$  is the conduction-band minimum,  $E_v$  is the valance-band maximum,  $E_g$  is the band gap ( $E_g = E_c - E_v$ ),  $h\nu$  is the photon energy and  $E_{vac}$  is the vacuum level, indicated for the case of either positive or negative EA. In the case of negative EA, once the photon excites electrons from valance band to conduction band, these excited electrons have a high probability to go from the conduction-band minimum to the vacuum level. This results in a narrow low-energy-electron peak of secondary electrons with spectral weight starting at the energy of

936

W. Meevasana et al. / Applied Surface Science 256 (2009) 934–936

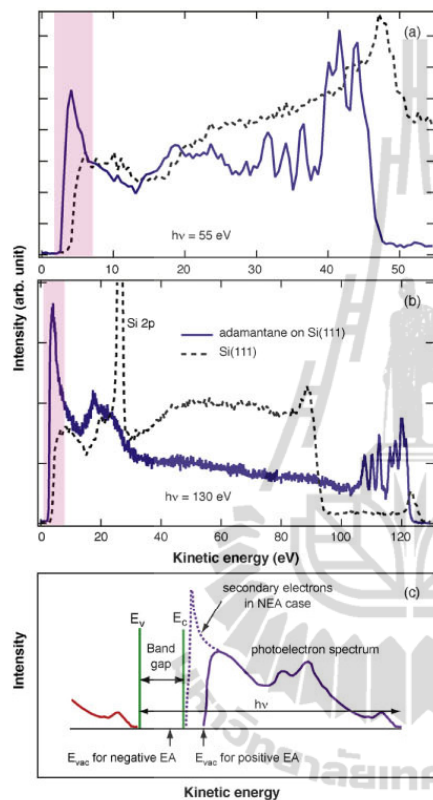


Fig. 4. Photoemission spectra of adamantane on Si(1 1 1) measured with photon energies of (a) 55 eV and (b) 130 eV. (c) A schematic photoelectron spectra in the case of either positive or negative electron affinity (EA); the description is in the text.

conduction-band minimum, as shown in the dashed line in Fig. 4(c), while this narrow peak (dashed line) will be absent in the case of positive EA. Note that in the case of positive EA, secondary electrons still occur but the spectrum would be rather broad with spectral weight starting at the energy of the vacuum level instead. From Ref. [4], this can be written in the following equations:

$$\chi + E_g = h\nu - W \quad (\text{in the case of positive EA})$$

$$E_g = h\nu - W \quad (\text{in the case of negative EA})$$

where  $\chi$  is the electron affinity for positive EA case, and  $W$  is the width of photoelectron spectrum.

From our spectra in Fig. 4(a) and (b),  $h\nu - W = 8.3 \pm 0.2$  eV; according to the equations above, this value should be equal to the band gap in the case of NEA. While the calculated DMC gap reported by Drummond et al. [8] is 7.61 eV, the uncertainty of this calculated value is still possible. Unfortunately, we are not aware of an experimentally-reported band gap of adamantane to confirm the gap value. Although the low-kinetic-energy-electron peak of adamantane implies the NEA effect, at this point, we still leave a possibility that the electron affinity might not be negative but could be a small positive value; the uncertainty will be resolved once the experimental value of band gap is available.

#### 4. Conclusions

From photoelectron study of adamantane on Si(1 1 1), we have found that the photoelectron spectra of adamantane on Si(1 1 1) also exhibit a peak at low-kinetic energy. This low-energy peak could be a generic phenomenon in diamondoid series. We interpret that the origin of this peak could be that the electron affinity of adamantane is either negative or small positive.

#### Acknowledgements

We would like to thank W.L. Yang for valued discussion and providing the samples. W.M. acknowledges DPST and R.S. acknowledges SLRI for the financial support.

#### References

- [1] J.E. Dahl, et al. Science 299 (2003) 96.
- [2] E.J. Himpfel, et al. Phys. Rev. B 20 (1979) 624.
- [3] J. van der Weide, R.J. Nemanich, Appl. Phys. Lett. 62 (1993) 1878.
- [4] R.J. Nemanich, et al. Diamond Relat. Mater. 5 (1996) 790.
- [5] W.L. Yang, et al. Science 316 (2007) 1460.
- [6] J.K. Simons, et al. Surf. Sci. 346 (1996) 21.
- [7] J.K. Simons, et al. J. Vac. Sci. Technol. A 11 (1993) 2244.
- [8] N.D. Drummond, et al. Phys. Rev. Lett. 95 (2005) 096801.

**Electronic Structure and Magnetic Anisotropy in Ni/Cu(001)  
from Angle-Resolved Photoemission Spectroscopy**Rachadaporn SUPRUANGNET<sup>1</sup>, Hideki NAKAJIMA<sup>2,3\*</sup>, Ritthikrai CHAI-NGAM<sup>2</sup>,  
Prayoon SONGSIRITTHIGUL<sup>1,2,3</sup>, and Akito KAKIZAKI<sup>4</sup><sup>1</sup>School of Physics, Suranaree University of Technology,

111 University Avenue, Muang District, Nakhon Ratchasima 30000, Thailand

<sup>2</sup>Synchrotron Light Research Institute (Public Organization),

111 University Avenue, Muang District, Nakhon Ratchasima 30000, Thailand

<sup>3</sup>Thailand Center of Excellence in Physics, CHE, Bangkok 10400, Thailand<sup>4</sup>Institute for Solid State Physics, The University of Tokyo, Kashiwa, Chiba 277-8581, Japan

(Received March 13, 2011; accepted March 31, 2011; published online May 25, 2011)

We investigated the thickness-dependent surface energy band structures of Ni films on a Cu(001) surface by angle-resolved photoemission spectroscopy. As the Ni film grows, Ni 3*d* bands are formed near the Fermi level in the range of the Cu 4*s* bands. In the surface band dispersions measured along the  $\bar{\Gamma}$ - $\bar{\Delta}$ - $\bar{X}$  plane, one band with  $d_{z^2}$  orbital character evolves with a small shift to low binding energy up to 20 ML, while the other band with  $d_{x^2-y^2}$  orbital character gradually forms with a shift to high binding energy above 6.6 ML. Both an increase of the  $d_{x^2-y^2}$  and a decrease of the  $d_{z^2}$  band fillings in the Ni thickness range between 6.6 and 20 ML contribute to reinforce the perpendicular magnetic anisotropy, which are partly backed up by a first-principles energy band calculation.

**KEYWORDS:** angle-resolved photoemission spectroscopy, surface energy band dispersion, perpendicular magnetic anisotropy

**1. Introduction**

Recently, the perpendicular magnetic anisotropy (PMA) of low-dimensional magnetic materials has attracted the attention of industrial engineers and basic researchers to develop high density magnetic recording and spin-electronic devices<sup>1,2)</sup> because they break through the limit of the size and capacity of conventional devices, which are based on the in-plane magnetic anisotropy due to the demagnetized-field effect. In general, the magnetic anisotropy in films is different than that in bulk because various lattice and electronic structures develop in the films on heterogeneous substrates.<sup>3,4)</sup> Thus far, it has been shown that particular film thicknesses of Ni/Cu, Co/Pt, and Co/Pd,<sup>5,6)</sup> systems show PMA leading to a high saturation magnetization as well as a high coercive force.<sup>7)</sup>

Among magnetic thin films for PMA, the Ni/Cu(001) system shows a stable PMA in a wide thickness range of Ni films at room temperature.<sup>8,9)</sup> The magnetization direction of Ni films was found to be parallel to the film surface below 7 monolayers (ML), varied from in-plane to out-of-plane at thicknesses of 7–10 ML and then switched from out-of-plane to in-plane with increasing film thickness up to 35–70 ML. These critical thicknesses responsible for the PMA of Ni films are understood as a result of the distortion of the atomic structures in films in such a way that the strain at the interface between Ni and Cu is gradually released with increasing film thicknesses.<sup>10)</sup>

According to the previously reported experiments,<sup>11–14)</sup> the ultra-thin Ni films are pseudomorphically formed, and the strains for the parallel and perpendicular directions of the surface result in a tetragonally distorted structure (fct) of the Ni films. The relativistic calculations of the electronic structure of fct Ni film show that the first PMA transition,

which occurs at thin Ni films, is due to a large quench of the in-plane magnetic anisotropies of the surface and interface.<sup>15–17)</sup> The second transition from PMA to the in-plane magnetic anisotropy is understood being due to the relaxation of the strains in sufficiently thick Ni films so that the surface in-plane anisotropy dominates.<sup>10)</sup> Recent photoemission studies reported the development of electronic structures in Ni films in the thickness range from the monolayer limit to bulk.<sup>18–21)</sup> It was found that the electronic structure of Ni films shows a bulk-like electronic structure above 3 ML. Though the magnetization and its direction are strongly dependent on the spin and orbital magnetic moments of the electrons, there is no critical change.<sup>22–24)</sup> It was revealed by photoemission spectroscopy that in Co/Pd(111), the re-orientation of the magnetization direction from perpendicular to in-plane magnetic anisotropies is due to the increase of Co 3*d* states responsible for in-plane orbital magnetic moments.<sup>25)</sup> So far, there has been no experimental evidence that explains the contribution of the electronic structures to PMA around the critical thickness in Ni/Cu(001), even though Hoesch *et al.* found that the binding energy shifts were due to the reduced number of *d* holes in the thin Ni films.<sup>20,26)</sup>

In this report, we discuss the origin of PMA based on the spin-orbit coupling where  $d_{x^2-y^2}$  and  $d_{z^2}$  orbitals contribute to the perpendicular and in-plane magnetic anisotropies. It was found that in Ni films on Cu(001) substrates, the *d* electron spins stabilize to the surface perpendicular direction due to the increase of  $d_{x^2-y^2}$  and the decrease of  $d_{z^2}$  orbital occupancy. The electronic structures were studied by both angle-resolved photoemission spectroscopy (ARPES) and a first-principles energy-band calculation.

**2. Experimental**

Photoemission experiments were carried out at beamline 4 of the Siam Photon Laboratory of the Synchrotron Light

\*E-mail: hideki@sri.or.th

Research Institute (SLRI).<sup>27)</sup> The ARPES apparatus consists of an ion gun, an electron gun for Auger electron spectroscopy (AES), a temperature-controlled sample holder, and an electron-energy analyzer (Thermo VG Scientific; ARUPS10). Pressure in the analysis chamber was below  $2 \times 10^{-10}$  mbar during the ARPES measurements. The overall energy resolution of the measured spectra was 170 meV at a photon energy of 45 eV, which was confirmed on the Fermi edge ( $E_F$ ) of a gold sample at room temperature. The acceptance angle of ARUPS10 was set to  $\pm 1^\circ$ .

A sample treatment was carried out under the following conditions. The Cu(001) surface was first bombarded using argon ions with a kinetic energy of 1.0 keV at a pressure of  $2.0 \times 10^{-6}$  mbar to remove impurities adsorbed in the atmospheric environment, which was monitored by AES. Repeated cycles of argon-ion bombardment and subsequent annealing at 753 K were adopted to reduce carbon, oxygen and sulfur impurities inside the sample to a negligible level. Finally, the long-range order of periodic surface structures was determined by low-energy electron diffraction (LEED) analysis. The sample surface was identified as a well-defined Cu(001) surface with a very sharp and low-background  $p(1 \times 1)$  LEED pattern.

Ni was deposited on the clean Cu(001) surface by either an e-beam evaporator or an effusion cell in the thickness range from 0.5 to 40 ML with a deposition rate of 40–90 s/ML at a pressure in between  $3.0 \times 10^{-9}$  and  $1.0 \times 10^{-8}$  mbar. Ni lumps (99.99%) for the evaporant were loaded into a BeO crucible in the effusion cell, and the rod was mounted as an e-beam target. During the deposition, we kept the flux constant and observed the reflection high-energy electron diffraction (RHEED) oscillation at an electron energy of 15 keV to evaluate the film thickness and quality. After the deposition, the Ni film was analyzed on the basis of the LEED pattern and AES measurement prior to photoemission measurements. Every LEED patterns showed the same  $p(1 \times 1)$  structure as observed in the clean Cu(001) surface.

In Fig. 1, the specular RHEED beam intensity is plotted as a function of deposition time. A single oscillation corresponds to a monolayer of epitaxial film growth so that the film thicknesses are easily identified. However, as reported previously,<sup>13)</sup> it was difficult to observe the RHEED oscillation above 7 ML, so we evaluated the film thickness from a deposition rate calculated from an early stage of the deposition. Above 7 ML, the evaluation of the film thickness using the AES measurement was also used because it was consistent with the film thickness resulting from the RHEED oscillation number below 7 ML. Insets of Fig. 1 show the LEED and RHEED patterns after a deposition of Ni 6.6 ML on Cu(001).

### 3. Results and Discussion

To clarify the thickness dependence of surface electronic structures, we measured the ARPES spectra for various Ni thicknesses on Cu(001) along the  $\Delta$  direction. Figures 2 and 3 show the ARPES spectra at an emission angle of 0 and  $10^\circ$ , respectively. The incident angle was set in either  $20^\circ$  or  $45^\circ$  specified in the figures, and the vector potential ( $A$ ) parallel to the plane of incidence ( $p$  polarization) was

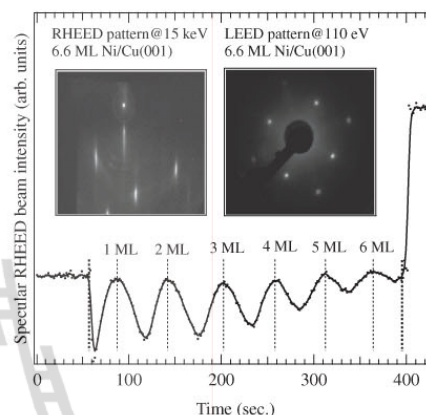


Fig. 1. The specular RHEED beam intensity in the deposition process. The beam intensity is normalized by the background. The solid line results from the smoothed beam intensity. The inset shows RHEED and LEED patterns after a deposition of Ni 6.6 ML on the Cu(001).

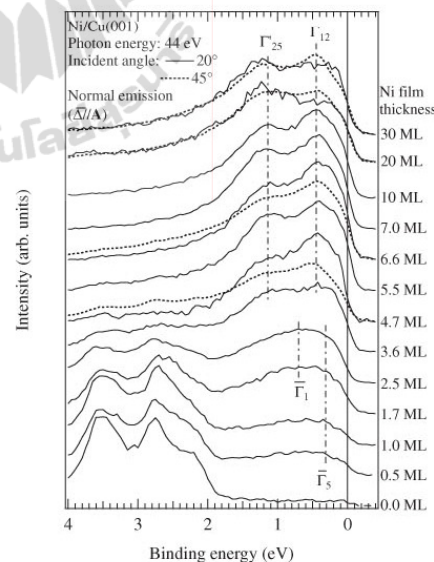
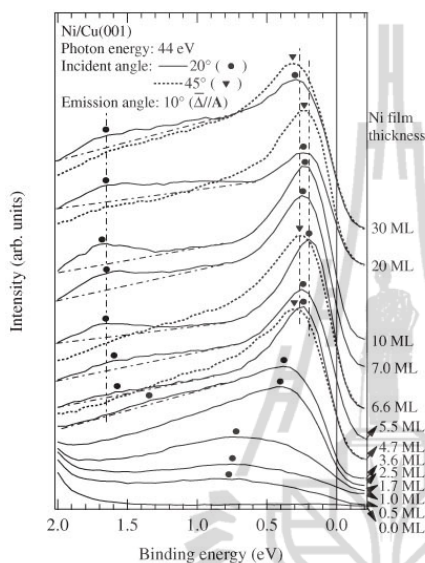


Fig. 2. Thickness dependence of ARPES spectra on the Ni/Cu(001). Spectra measured at normal emission are shown in the order of Ni film thickness from bottom to top as labeled on the right hand side of each spectrum. The photon energy and incident angle are 44 eV and  $20^\circ$ . Some spectra at an incident angle of  $45^\circ$  are also shown.



**Fig. 3.** Thickness dependence of ARPES spectra on the Ni/Cu(001). Spectra measured at an emission angle of  $10^\circ$  are shown in the order of Ni film thickness from bottom to top as labeled on the right hand side of each spectrum. The photon energy and incident angle are 44 eV and  $20^\circ$ . Some spectra at an incident angle of  $45^\circ$  are also shown.

aligned in a mirror plane of  $\bar{\Delta}$ . The ARPES analyzer was also deployed in the same mirror plane identifying the only even initial state symmetry discussed later. A photon energy of 44 eV was fixed corresponding to the  $\Gamma$  point of the bulk Brillouin zone (BZ). Each spectrum was normalized to the integrated intensity because the photoionization cross section is almost equivalent for the Ni and Cu  $3d$  electrons in the soft x-ray energy range. In Figs. 2 and 3, the Ni and Cu  $3d$  bands are clearly distinguished below and above 2 eV of binding energy. Although the Cu  $4sp$  bands are overlapped with the Ni and Cu  $3d$  bands, the contribution of  $sp$  bands is negligible near  $\bar{\Gamma}$ . The increasing thickness of the Ni film leads to the decreasing intensity of Cu  $3d$  bands and the increasing intensity of Ni  $3d$  bands up to 7 ML. Above 7 ML, the Cu band does not appear in the spectra being due to the short mean free path of photoelectrons.

In Fig. 2, the normal-emission spectra of the Ni  $3d$  bands are dominated by two-peak structure. A difference between the spectra with film thicknesses below and above 3 ML was observed with the help of previously reported data.<sup>19)</sup> broad features discernible around 0.32 and 0.66 eV below 3 ML film, shaped as peaks at 0.45 and 1.15 eV above 3 ML. It is reasonable to say that each peak component in the broad feature varied its intensity with increasing film thicknesses, which are indicated by the lines with dots in Fig. 2. These states are due to a formation of two-dimensional band

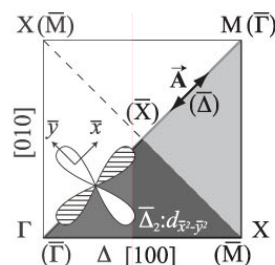


**Fig. 4.** A simple drawing of the  $d_{x^2-y^2}$  orbital along the  $\bar{\Delta}$  mirror plane in the surface BZ coordinate. The bulk BZ (light gray) is also shown including the surface BZ (dark gray). In this figure, irreducible representations and coordinates in the surface BZ are described with a overline and parentheses.

structures including surface, interface, and film depending on the Ni film thickness. The small differences of spectra measured in two incident angles might be due to the overlapping between surface and bulk electronic structures. However, the intensity at 0.45 eV of a  $45^\circ$  incidence in 4.7 ML, becomes small in 6.6 ML being due to the developing bulk electronic structure of  $\Gamma_{12}$  clearly observed above 20 ML. An important point to be mentioned here is that the normal-emission spectra do not show any significant thickness and polarization dependences in terms of the energy position. In contrast, when the emission angle increases, the corresponding spectra show clear differences upon the thickness and polarization, as shown in Fig. 3 at an emission angle of  $10^\circ$ . Figure 3 shows that two thickness dependences are observed above 3 ML in the spectra at a  $20^\circ$ : one peak at 1.35 eV in 3.6 ML shifts to a high binding energy of 1.65 eV above 6.6 ML. The other peak at 0.4 eV in 2.5 ML shifts to a low binding energy of 0.2 eV at 6.6 ML and shifts to high binding energy above 6.6 ML. At an incident angle of  $45^\circ$ , the former peak does not appear, while the latter peak shows a slight shift to low binding energy of 0.23 eV up to 20 ML. The lines with dots represent the guides for eyes to clarify the peak positions relative to 6.6 ML and backgrounds around 1.65 eV on the spectra at an incident angle of  $20^\circ$  in Fig. 3. It should be noted that initial states of all both symmetries are observed for the both incident angles of 20 and  $45^\circ$  because the vector potential and ARPES analyzer cannot be definitely aligned in the normal or parallel to the sample surface in the experimental condition. However, we discuss two symmetries on each peak near  $E_F$ , because the difference in the peak positions is not negligible.

Our ARPES geometry with  $p$ -polarized light along the  $\bar{\Delta}$  mirror plane constrains to excite the even initial states with respect to the  $\bar{\Delta}$  mirror plane so that the bands with  $d_{z^2}$  and  $d_{x^2-y^2}$  orbital characters are possibly excited corresponding to  $\Delta_1$  and  $\Delta_2$ , respectively.<sup>28)</sup> As shown in Fig. 4, because the surface BZ coordinate ( $x$ -axis) described in our  $d$  orbital representations is different by  $45^\circ$  from the bulk BZ coordinate,  $\Delta_2$  corresponds to  $\bar{\Delta}_2$ , and  $\Delta_1$  to  $\bar{\Delta}_1$ . In connection with the bulk state, the  $\Delta_2$  state from  $\Delta_2$  is possibly converged into the  $\Gamma'_{25}$  state decomposing into  $\Delta'_2$

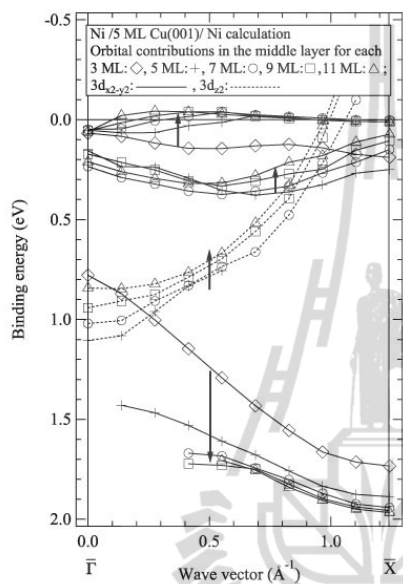


**Fig. 5.** First-principles energy band calculations in paramagnetic Ni films in the Ni/5 ML-Cu(001)/Ni structure. The Ni and Cu atomic structures with a fixed in-plane lattice constant of 3.58 Å are optimized in the total energy calculation. The markers indicate only a strong contribution from each  $d$  orbital to the bands in the middle layer of each Ni film, and arrows represent shifts for each  $d$  orbital.

and  $\Delta_5$  as reported previously.<sup>19,21</sup> Note that the  $d$  orbitals assigned here are one of the basis sets to describe the orbital contribution to the magnetic anisotropy. A disagreement from the bulk symmetry might be due to the surface origin identified in the result of calculation.

The selection of the initial state symmetries depends on the direction of the vector potential in such a way that the perpendicular and parallel vector potentials to the surface preferably excite the  $\Delta_1$  and  $\Delta_2$  bands. In 6.6 ML, the peak at 1.65 eV observed in the spectra at a 20° incident was not found in the spectra at a 45° incident angle, so the band originates from  $d_{x^2-y^2}$ . The peak intensities from 0.2 to 0.3 eV observed in incident angles of 20 and 45° show almost equivalent each other, while their energy position and shift upon the polarization are slightly different. These results suggest that two peaks are overlapped; one observed in an incident angle of 20° originates from the band with  $d_{x^2-y^2}$ , the other in an incident angle of 45° with  $d_{z^2}$ . These assignments were found to be in fair agreement with the first-principles energy-band calculation using the Vienna *ab-initio* simulation package<sup>29</sup> based on the projector-augmented-wave formalism<sup>30</sup> with a spin-polarized generalized-gradient approximation.<sup>31</sup> Figure 5 shows the  $d$ -orbital dependent energy-band structure for Ni film thicknesses between 3 and 11 ML in the Ni/5 ML-

Cu(001)/Ni structure. The calculation was performed for paramagnetic Ni because the Curie temperature in thin Ni films is lower than room temperature. A fixed in-plane lattice constant of 3.58 Å obtained from previously reported experiment<sup>11</sup> was employed to optimize the Ni and Cu atomic structures in the total energy calculation. The markers indicate only a thickness-dependent contribution from each  $d$  orbital to the bands in the middle layer of each Ni film depending on the Ni film thickness. The band at 1.1 eV in 7 ML at the  $\Gamma$  point originates from  $d_{z^2}$ , showing a large dispersive  $sp-d$  hybridized band across  $E_F$ , which shifts slightly to low binding energy as the Ni film thickness increases. The band at 0.8 eV in 3 ML originates from  $d_{x^2-y^2}$ , showing a dispersion to high binding energy along the  $\Gamma$ - $\bar{X}$  direction, and shifts to low binding energy as the Ni film thickness increases. These energy band symmetries, dispersions, and binding energy shifts upon the film thickness for each band were found to be in good agreement with our ARPES spectral profile, despite slightly different binding energies. The two-band sets from -0.1 to 0.4 eV originating from  $d_{x^2-y^2}$  and partly shifting to low binding energy might correspond to the peak at 0.2 eV in 6.6 ML film observed in the spectra measured at an incident angle of 20°. The calculated shift to low binding energy is in agreement with that up to 6.6 ML, while does not agree with the shift to high binding energy above 6.6 ML. The discrepancy might be due to the limitation in the energy band calculation at a fixed in-plane lattice constant, resulting in the lattice relaxation only in the surface normal direction. Even though the multilayer growth mode was found above 7 ML in the scanning tunneling microscopy,<sup>13</sup> it does not take into consideration in our calculation.

According to the spin-orbit coupling model of PMA,<sup>22</sup> the observed Ni film thickness dependence of the binding energy shift of Ni 3d states is reasonably explained as follows. When a binding energy of the out-of-plane distributed electronic structure ( $d_{z^2}$ ) decreases as the thickness increases, PMA is stabilized by decreasing band filling responsible for the in-plane magnetic anisotropy up to 20 ML. The binding energy shifts of the in-plane distributed electronic structure ( $d_{x^2-y^2}$ ) favor PMA to increase the band filling responsible for PMA above 6.6 ML. However, the band from 0.8 to 2 eV away from  $E_F$  might not effect to PMA because the shift does not contribute to the occupancy. These results are consistent with those obtained in the recent works showing the Fermi surface in hybridization with  $sp$ - and  $d$ -like bands in 2–6 ML.<sup>20,21</sup>

In summary, we identified the energy band shifts to stabilize the PMA around the critical thickness in the Ni/Cu(001). The observed binding energy shifts and energy band dispersions revealed that the orbital magnetic anisotropy plays a key role in the formation of PMA on the Ni/Cu(001).

#### Acknowledgment

Authors thank all of the technical staff members of SLRI for their support. One of the authors (R.S.) would like to thank SLRI for the scholarship (Contract No.: GS-50-D05). The authors acknowledge the group of S. Limpijumong for their help with some of the calculations.

## Manuscript published in Journal of the Physical Society of Japan

Person-to-person distribution by the author only. Not permitted for publication for institutional repositories or on personal Web sites.

J. Phys. Soc. Jpn. **80** (2011) 064706

FULL PAPERS

R. SUPRIANGNET *et al.*

- 1) J. Hong, R. Q. Wu, J. Lindner, E. Kosubek, and K. Baberschke: *Phys. Rev. Lett.* **92** (2004) 147202.
- 2) S. Hope, E. Gu, B. Choi, and J. A. C. Bland: *Phys. Rev. Lett.* **80** (1998) 1750.
- 3) U. Gradmann: *J. Magn. Magn. Mater.* **54-57** (1986) 733.
- 4) J. G. Gay and R. Richter: *Phys. Rev. Lett.* **56** (1986) 2728.
- 5) F. J. A. den Broeder, W. Hoving, and P. J. H. Bloemen: *J. Magn. Magn. Mater.* **93** (1991) 562; F. J. A. den Broeder, E. Janssen, W. Hoving, and W. B. Zeper: *IEEE Trans. Magn.* **28** (1992) 2760; F. J. A. den Broeder, H. W. van Kesteren, W. Hoving, and W. B. Zeper: *Appl. Phys. Lett.* **61** (1992) 1468.
- 6) P. F. García, A. D. Meinhardt, and A. Suna: *Appl. Phys. Lett.* **47** (1985) 178.
- 7) S. Iwasaki and Y. Nakamura: *IEEE Trans. Magn.* **13** (1977) 1272.
- 8) B. Schulz and K. Baberschke: *Phys. Rev. B* **50** (1994) 13467.
- 9) R. Jungblut, M. T. Johnson, J. aan de Stegge, A. Reinders, and F. J. A. den Broeder: *J. Appl. Phys.* **75** (1994) 6424.
- 10) W. L. O'Brien and B. P. Tonner: *J. Appl. Phys.* **79** (1996) 5623; W. L. O'Brien, T. Droubay, and B. P. Tonner: *Phys. Rev. B* **54** (1996) 9297.
- 11) W. Platow, U. Bovensiepen, P. Pouloupoulos, M. Farle, K. Baberschke, L. Hammer, S. Walter, S. Müller, and K. Heinz: *Phys. Rev. B* **59** (1999) 12641.
- 12) S. Müller, B. Schulz, G. Kostka, M. Farle, K. Heinz, and K. Baberschke: *Surf. Sci.* **364** (1996) 235.
- 13) J. Shen, J. Giergiel, and J. Kirschner: *Phys. Rev. B* **52** (1995) 8354.
- 14) M. Farle, B. Mirwald-Schulz, A. N. Anisimov, W. Platow, and K. Baberschke: *Phys. Rev. B* **55** (1997) 3708; M. Farle, W. Platow, A. N. Anisimov, P. Pouloupoulos, and K. Baberschke: *Phys. Rev. B* **56** (1997) 5100.
- 15) J. Henk, A. M. N. Niklasson, and B. Johansson: *Phys. Rev. B* **59** (1999) 9332.
- 16) O. Hjortstam, K. Baberschke, J. M. Wills, B. Johansson, and O. Eriksson: *Phys. Rev. B* **55** (1997) 15026.
- 17) C. Uiberacker, J. Zabloudil, P. Weinberger, L. Szunyogh, and C. Sommers: *Phys. Rev. Lett.* **82** (1999) 1289.
- 18) G. J. Mankey, K. Subramanian, R. L. Stockbauer, and R. L. Kurtz: *Phys. Rev. Lett.* **78** (1997) 1146.
- 19) C. Pampuch, O. Rader, R. Kläsges, and C. Carbone: *Phys. Rev. B* **63** (2001) 153409.
- 20) M. Hoesch, V. N. Petrov, M. Muntwiler, M. Hengsberger, J. L. Checa, T. Greber, and J. Osterwalder: *Phys. Rev. B* **79** (2009) 155404.
- 21) O. Rader, H. Wolf, W. Gudat, A. Tadic, L. Broekman, E. Huwald, R. C. G. Leckey, J. D. Riley, A. M. Shikin, F. Matsui, H. Miyata, and H. Daimon: *Phys. Rev. B* **79** (2009) 245104.
- 22) H. Takayama, K. P. Bohnen, and P. Fulde: *Phys. Rev. B* **14** (1976) 2287.
- 23) G. H. O. Daalderop, P. J. Kelly, and M. F. H. Schuurmans: *Phys. Rev. B* **50** (1994) 9989.
- 24) M. T. Johnson, R. Jungblut, P. J. Kelly, and F. J. A. den Broeder: *J. Magn. Magn. Mater.* **148** (1995) 118.
- 25) M. Sawada, K. Hayashi, and A. Kakizaki: *J. Phys. Soc. Jpn.* **72** (2003) 1161.
- 26) P. Srivastava, N. Haack, H. Wende, R. Chauvistré, and K. Baberschke: *Phys. Rev. B* **56** (1997) R4398.
- 27) H. Nakajima, M. Buddhakala, S. Chumpolkulwong, R. Supriangnet, A. Kakizaki, and P. Songsiririthigul: *AIP Conf. Proc.* **879** (2007) 543.
- 28) J. Hermanson: *Solid State Commun.* **22** (1977) 9.
- 29) G. Kresse and J. Hafner: *Phys. Rev. B* **47** (1993) R558.
- 30) G. Kresse and J. Joubert: *Phys. Rev. B* **59** (1999) 1758.
- 31) J. P. Perdew, J. A. Chevary, S. H. Vosko, K. A. Jackson, M. R. Pederson, D. J. Singh, and C. Fiolhais: *Phys. Rev. B* **46** (1992) 6671.

Abstract submitted for the Siam Physics Congress 2008, Nakorn Ratchasima (2008)

SPC2008  
NAKORN RATCHASIMA, THAILAND

### **Study of Adamantane on Si(111) as a Potential Electron Emitter**

*W. Meevasana<sup>1,2</sup>, R. Supruangnet<sup>3\*</sup>, H. Nakajima<sup>1</sup>, and P. Songsiririthigul<sup>1,3</sup>*

<sup>1</sup>National Synchrotron Research Center, Nakhon Ratchasima, Thailand

<sup>2</sup>Department of Physics, Stanford University, Stanford, California, USA

<sup>3</sup>School of Physics, Suranaree University of Technology, Nakhon Ratchasima, Thailand

#### **Abstract**

Diamondoids, a series of hydrocarbon compounds whose carbon atoms form diamond-like nanostructures, have attracted attention as recently they can be extracted from petroleum waste. Moreover, tetramantane (four-unit diamondoid) is found to show the property of negative electron-affinity materials, which have potential use as efficient monochromatic electron emitters. Here, we study the electronic property of adamantane, the smallest-size diamondoid. Adamantane is evaporated on Si(111) and the photoelectron from the sample is further measured with photoemission spectroscopy. We has found that the photoelectron spectra of adamantane on Si(111) also exhibits a peak at low-kinetic energy which is an indication of negative-electron-affinity effect and makes this effect more general in diamondoids.

**Keyword:** photoemission, adamantane, diamondoid, negative electron affinity

---

\* Corresponding author. Email: aufee@hotmail.com

Abstract submitted for the Siam Physics Congress 2009, Phetchburi (2009)

SPC2009  
CHA-AM, PHETCHBURI, THAILAND

Poster Presentation

### **Angle-resolved photoemission spectroscopy in ultra-thin Ni film on Cu(001)**

*R. Supruangnet<sup>1</sup>, H. Nakajima<sup>2,3</sup>, R. Chai-ngam<sup>2,4</sup> and P. Songsirithigul<sup>1,2,3\*</sup>*

<sup>1</sup>School of Physics, Suranaree University of Technology, Nakhon Ratchasima, Thailand

<sup>2</sup>Synchrotron Light Research Institute, Nakhon Ratchasima, Thailand

<sup>3</sup>Nanospectroscopy Laboratory - ThEP Center, Nakhon Ratchasima, Thailand

<sup>4</sup>Department of Physics, Mahasarakham University, Mahasarakham, Thailand

#### **Abstract**

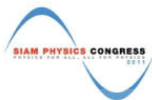
This report presents the results from the investigations of Ni ultra-thin film on Cu(001) studied by angle-resolved photoemission spectroscopy (ARPES), Auger electron spectroscopy, low-energy electron diffraction and reflection high-energy electron diffraction (RHEED). The MBE growth of Ni film was monitored by RHEED and its intensity showed a layer-dependent oscillation which is characteristic of layer-by-layer growth. The ARPES spectra revealed the energy band dispersions depending on Ni film thickness in the range of several monolayers close to a critical thickness (7ML) of both spin reorientation transition and magnetic phase transition.

**Keyword:** Angle-resolved photoemission spectroscopy, ultra thin film, nickel, spin-reorientation

---

\* Corresponding author. Email: [prayoon@sri.or.th](mailto:prayoon@sri.or.th)

Abstract submitted for the Siam Physics Congress 2011, Chonburi (2011)



Siam Physics Congress SPC2011  
*Physics for all, all for physics* 23-26 March 2011

## First-principles calculation of magnetic anisotropy on Ni films

Ratchadaporn Supruangnet<sup>1</sup>, Hideki Nakajima<sup>2,3\*</sup> and Prayoon  
Songsiriritthigul<sup>1,2,3</sup>

<sup>1</sup>*School of Physics, Suranaree University of Technology, 111 University Avenue,  
Muang District, Nakhon Ratchasima 30000, Thailand*

<sup>2</sup>*Synchrotron Light Research Institute (Public Organization), 111 University Avenue,  
Muang District, Nakhon Ratchasima 30000, Thailand*

<sup>3</sup>*ThEP Center, Commission on Higher Education, Bangkok 10400, Thailand*

*\*Corresponding author. E-mail: hideki@slri.or.th*

### Abstract

For Ni films on Cu(001), it is known that the spin-reorientation transition (SRT) from an in-plane to out-of-plane magnetization directions appears when the Ni thickness is increased above 7 ML. However, the origin of SRT has not been studied from the electronic structure viewpoint, so far. To identify the contribution of the density-of-states (DOS) to SRT, we calculated the thickness dependence of the magnetic anisotropy energy (MAE) in paramagnetic Ni/Cu superlattices using the Vienna *ab-initio* simulation package. Six vacuum layers separate the  $m$  ML Ni/5 ML Cu/ $m$  ML Ni supercells ( $m$ : Ni film thickness up to 11 ML). In all calculations, the in-plane lattice was fixed, while the interlayer distance was relaxed. It was found that the calculated MAE becomes positive above 6 ML. The shifts of d-orbital dependent DOS will be discussed around the SRT.

**Keywords:** Ni Film, Spin-Reorientation Transition, Magnetic Anisotropy

# CURRICULUM VITAE

Miss. Ratchadaporn Supruangnet

Date of birth: 20 August 1981

Place of birth: Bangkok, Thailand

Nationality: Thai

## Education

Academic year

1999-2002 Khon Kaen University, Khon Kaen, Thailand.

Bachelor of Science (Physics)

2004-2006 Suranaree University of Technology, Nakhon Ratchasima,  
Thailand.

Master of Science (Physics)

2007-2010 Suranaree University of Technology, Nakhon Ratchasima,  
Thailand.

Ph.D. candidate in Physics

## Academic experience

2003 Research Assistant, National Metal and Materials Technology  
Center, Thailand Science Park, Pathumthani, Thailand.